

PASSIVELY MODELOCKED ELECTRICALLY PUMPED VECSELS

A dissertation submitted to

ETH ZÜRICH

for the degree of

DOCTOR OF SCIENCES

presented by

WOLFGANG PETER PALLMANN

Dipl.-Ing. Univ.
Friedrich-Alexander-Universität Erlangen, Germany

born on June 9, 1983

citizen of Germany

accepted on the recommendation of

Prof. Dr. U. Keller, Supervisor
Prof. Dr. B. Witzigmann, Co-Examiner

September 2013

Table of Contents

<i>Symbols and Abbreviations</i>	VII
<i>List of Figures</i>	XIII
<i>List of Tables</i>	XV
<i>Publications</i>	XVII
<i>Abstract</i>	XXII
<i>Kurzfassung</i>	XXIV
Chapter 1 Introduction	1
Chapter 2 Electrically pumped VECSELs	7
2.1 General design considerations	7
2.1.1 Current confinement	8
2.1.2 Field enhancement and gain	9
2.1.3 Optimization for modelocked operation.....	11
2.2 Design details and wafer growth.....	13
2.3 Simulation of EP-VECSELs	15
2.3.1 Multilayer structure simulation.....	15
2.3.2 EP-VECSEL numerical simulations.....	15
Chapter 3 Passively Modelocked VECSELs	17
3.1 Active and passive modelocking	18
3.2 Mechanisms of passive modelocking.....	19
3.2.1 Fast saturable absorber.....	20
3.2.2 Slow saturable absorber with constant gain	20
3.2.3 Slow saturable absorber with strong gain saturation.....	21
3.3 Pulse formation in passively modelocked VECSELs	22
3.3.1 Gain and absorber saturation.....	22
3.3.2 Quasi-soliton modelocking.....	22
3.4 Semiconductor saturable absorber mirrors	24

3.4.1	Carrier dynamics in semiconductor absorbers.....	24
3.4.2	SESAM design and parameters	25
3.4.3	Important SESAM parameters	26
3.4.4	Measurement of the non-linear SESAM reflectivity	27
Chapter 4	Semiconductor fabrication techniques	31
4.1	Semiconductor materials and growth	31
4.1.1	Choice of the material system	31
4.1.2	Semiconductor growth and calibration	33
4.2	Processing	36
4.2.1	Fabrication methods	36
4.2.2	EP-VECSEL process flow	42
4.2.3	Challenges in the realization of EP-VECSELs	44
Chapter 5	First experimental results	47
5.1	Test setup.....	48
5.2	Electrical characterization	48
5.2.1	Threshold behavior and resistance.....	48
5.2.2	Current confinement	49
5.3	Continuous-wave characterization.....	50
5.3.1	Output power and powerscaling.....	50
5.3.2	Spectral properties of the EP-VECSELs.....	52
5.3.3	Beam quality of the EP-VECSELs.....	54
Chapter 6	Beam quality and gain characterization of EP-VECSELs	55
6.1	Design of the characterized devices	56
6.2	Electrical and cw multi-mode characterization	57
6.3	Beam quality characterization	58
6.4	Spectral gain characterization.....	59
6.4.1	Measurement setup	59
6.4.2	Spectral gain measurements.....	60
6.5	Gain saturation measurements.....	63
6.5.1	Measurement method and setup.....	63
6.5.2	Gain saturation measurements	66
6.6	Passive modelocking experiments.....	68

6.6.1	Cavity setup	68
6.6.2	Passive modelocking results	69
Chapter 7	EP-VECSEL design improvements	71
7.1	Electrical optimization of the p-DBR.....	71
7.1.1	p-DBR design for low electrical losses.....	72
7.1.2	Realized designs of the improved p-DBR	76
7.1.3	Improvement of the measurement technique.....	77
7.1.4	Electrical measurements of the improved p-DBRs	78
7.1.5	Further possible improvements.....	80
7.2	Improvement of the thermal management.....	81
7.3	Beam quality optimization.....	83
7.4	Improved design	84
Chapter 8	Experimental results of the improved design	87
8.1	Electrical characterization	88
8.2	Continuous wave characterization	89
8.2.1	Multi-mode performance and powerscaling	89
8.2.2	Beam quality and single-mode performance.....	93
8.3	Passive modelocking experiments.....	94
8.3.1	Experimental setup	94
8.3.2	Experimental results.....	95
8.4	Limitations and outlook	96
8.4.1	Performance limitations of the modelocked EP-VECSELs.....	96
8.4.2	Possible improvements for higher average output power	96
Chapter 9	Conclusion and outlook	99
	<i>References</i>	103
	<i>Curriculum Vitæ</i>	109
	<i>Acknowledgements</i>	111

Symbols and Abbreviations

Symbols

A	beam area (m^2)
c_0	speed of light in vacuum ($\text{m}\cdot\text{s}^{-1}$)
D	group delay dispersion (GDD) coefficient (s^2)
d	thickness (m)
dR_{th}	differential resistance at lasing threshold ($\text{V}\cdot\text{A}^{-1}$)
e	elementary charge (C)
E	normalized electric field amplitude or energy (J)
E_{sat}	saturation energy (J)
E_{v}	valence band energy (eV)
F	fluence ($\text{J}\cdot\text{m}^{-2}$)
f	focal length (m) or frequency (Hz)
F_2	induced absorbtion coefficient ($\text{J}\cdot\text{m}^{-2}$)
f_{rep}	repetition frequency (Hz)
F_{sat}	saturation fluence ($\text{J}\cdot\text{m}^{-2}$)
G	power gain coefficient
g_{ss}	small-signal gain
$g_{\text{ss,eff}}$	effective small-signal gain
I	electric current (A)
I_{th}	lasing threshold current (A)
J_{th}	lasing threshold current density ($\text{A}\cdot\text{m}^{-2}$)
l	loss
L	optical length (m)
M^2	beam quality factor
N	carrier density (m^{-3})
n	refractive index or electron density (m^{-3})
N_{A}	acceptor doping concentration (m^{-3})
N_{D}	donator doping concentration (m^{-3})

VIII SYMBOLS AND ABBREVIATIONS

N_{QW}	number of quantum wells
P	power (W)
p	hole density (m^{-3})
R	reflectivity
R_{lin}	linear reflectivity
R_{ns}	non-saturable reflectivity
R_{ss}	reflectivity of the small-signal gain
S	signal
T	temperature (K)
T_{R}	cavity round-trip time (s)
V	voltage (V)
x	molefraction
z	position (m)
α_{FCA}	free carrier absorption coefficient (m^{-1})
\mathcal{E}	normalized electric field amplitude
Γ	field enhancement of the gain
Γ_{abs}	field enhancement in the absorber
κ	coefficient of thermal conductivity ($\text{W}\cdot\text{m}^{-1}\cdot\text{K}^{-1}$)
λ	wavelength (m)
ΔR	modulation depth
ΔR_{ns}	non-saturable losses
ΔT	temperature increase (K)
τ_{pulse}	pulse duration (s)
ν	optical frequency (Hz)

Abbreviations

ADC	analog-to-digital converter
Al	aluminum
AlAs	aluminum arsenide
AlGaAs	aluminum gallium arsenide
AR	anti-reflection
Ar	argon
As	arsenic
Au	gold
BCD	bottom contact diameter
BS	beam splitter
C	carbon
CB	conduction band
CBr ₄	carbon tetra-bromide
Cl	chlorine
Cr	chromium
CSL	current spreading layer
CTE	coefficient of thermal expansion
Cu	copper
cw	continuous-wave
DBR	distributed Bragg reflector
DI	de-ionized
DPSSL	diode-pumped solid-state laser
EL	electroluminescence
EP	electrical pumping
F	fluorine
FCA	free carrier absorption
FS	fused silica
FWHM	full-width half-maximum
Ga	gallium
GaAs	gallium arsenide
GDD	group delay dispersion

Ge	germanium
H	hydrogen
HCl	hydrochloric acid
HF	hydrofluoric acid
HMDS	hexamethyldisilazane
HR	high reflector
IA	induced absorption
ICP	inductively-coupled plasma
In	indium
InAs	indium arsenide
InGaAs	indium gallium arsenide
IPA	isopropanol
KLM	Kerr lens mode-locking
LIV	light-current-voltage
MBE	molecular beam epitaxy
MIXSEL	mode-locked integrated external-cavity surface-emitting laser
MOVPE	metal-organic vapor-phase epitaxy
N	nitrogen
Ni	nickel
O	oxygen
OC	output coupler
OP	optical pumping
PBS	polarizing beam splitter
PD	photodiode
PECVD	plasma-enhanced chemical vapor deposition
PL	photoluminescence
Pt	platinum
QD	quantum dot
QML	Q-switched modelocking
QW	quantum well
RBW	resolution bandwidth
RF	radio frequency

RIE	reactive ion etching
ROC	radius of curvature
RTA	rapid thermal annealing
SEM	scanning electron microscope
SESAM	semiconductor saturable absorber mirror
SHG	second-harmonic generation
Si	silicon
SI	semi-insulating
SiN _x	silicon nitride
Sn	tin
SPM	self-phase modulation
TBP	time-bandwidth product
TCE	trichloroethylene
TEC	thermo-electric cooler
TEM	transverse electromagnetic mode or transmission electron microscope
Ti	titanium
TPA	two-photon absorption
UV	ultra-violet
VB	valence band
VCSEL	vertical cavity surface-emitting laser
VECSEL	vertical external-cavity surface-emitting laser
W	tungsten
Zn	zinc

List of Figures

Figure 1.1:	Schematic of a passively modelocked OP- and EP-VECSEL.	4
Figure 2.1:	Schematic of the EP-VECSEL gain chip.	8
Figure 2.2:	Field enhancement and reflectivity as function of the number of n-DBR pairs.	10
Figure 2.3:	Influence of the AR-coating on the field enhancement and the GDD.	11
Figure 2.4:	Estimation for obtainable pulse duration from a passively modelocked EP-VECSEL.	12
Figure 2.5:	Initial design of the electrically pumped VECSEL.	13
Figure 3.1:	Active and passive modelocking.	19
Figure 3.2:	Mechanisms of passive modelocking.	20
Figure 3.3:	Soliton-like pulse shaping mechanism in modelocked VECSELs.	23
Figure 3.4:	Carrier dynamics in a SESAM.	24
Figure 3.5:	Antiresonant and resonant SESAM design.	25
Figure 3.6:	Non-linear reflectivity curve and fit of a resonant SESAM.	26
Figure 3.7:	Measurement setup for the non-linear reflectivity of SESAMs.	28
Figure 3.8:	Signal analysis for a typical non-linear reflectivity measurement.	29
Figure 4.1:	Bandgap energy as function of the lattice constant of III/V-semiconductors.	32
Figure 4.2:	Growth error analysis.	34
Figure 4.3:	SEM and TEM images of an EP-VECSEL.	35
Figure 4.4:	Effect of annealing on the IV-curve of an EP-VECSEL.	41
Figure 4.5:	SEM image of a processed device.	44
Figure 4.6:	Influence of the AR-definition and the diffusion barrier on the IV-curve.	45
Figure 5.1:	Images of the fabricated EP-VECSEL gain chip.	47
Figure 5.2:	Straight cavity for the cw characterization.	48
Figure 5.3:	I_{th} and dR_{th} as a function of the BCD.	49
Figure 5.4:	EL profiles of EP-VECSELs with different BCD.	49
Figure 5.5:	LIV-curve of a 180- μ m BCD EP-VECSEL.	50
Figure 5.6:	Effect of the OC transmission on the output power.	51
Figure 5.7:	P_{out} and J_{th} as a function of the BCD.	51
Figure 5.8:	Optical spectrum and wavelength shift of a 100- μ m-BCD EP-VECSEL.	52
Figure 5.9:	Estimated temperature shift as function of the current density.	53
Figure 6.1:	Image of the <i>Philips U-L-M Photonics</i> EP-VECSELs on a TO-can mount.	56
Figure 6.2:	Electrical and cw multi-mode characterization.	57
Figure 6.3:	Schematic of the spectral gain measurement setup.	59
Figure 6.4:	Gain spectra for EP-VECSEL with 9 n-DBR pairs.	61
Figure 6.5:	Gain spectra for EP-VECSEL with 13 n-DBR pairs.	62
Figure 6.6:	Measurement method for the gain saturation of EP-VECSELs.	64
Figure 6.7:	Schematic of the gain saturation measurement setup.	65
Figure 6.8:	Gain saturation measurements of the two EP-VECSEL gain chips.	67
Figure 6.9:	Schematic of the cavity setup for the modelocking experiments.	68
Figure 6.10:	Modelocking results of the <i>Philips U-L-M Photonics</i> EP-VECSELs.	70

XIV LIST OF FIGURES

Figure 7.1:	Valence band at AlAs/GaAs heterointerface.	72
Figure 7.2:	Simulated valence band and TEM-images for different interfaces.	73
Figure 7.3:	AlAs/GaAs p-DBR with a stepped molefraction grading.	74
Figure 7.4:	Simulation of an optimized p-DBR with stepped molefraction grading.	75
Figure 7.5:	$\text{Al}_{0.9}\text{Ga}_{0.1}\text{As}$ /GaAs p-DBR with a bi-parabolic digital alloy molefraction grading.	76
Figure 7.6:	p-DBR electrical measurement techniques.	78
Figure 7.7:	IV-curves of the improved p-DBRs.	79
Figure 7.8:	Temperature increase and output power as function of the device size.	81
Figure 7.9:	New maskset for improved thermal management.	82
Figure 7.10:	Improved design of the EP-VECSEL.	84
Figure 8.1:	Images of the improved EP-VECSEL gain chip.	88
Figure 8.2:	I_{th} and dR_{th} as a function of the BCD.	88
Figure 8.3:	LIV-curve of a 200- μm BCD EP-VECSEL.	89
Figure 8.4:	Influence of the temperature on the LIV-curve of a 100- μm BCD EP-VECSEL.	90
Figure 8.5:	Influence of the OC transmission on the LI-curve of a 100- μm BCD EP-VECSEL.	90
Figure 8.6:	Optical spectra as a function of wavelength and injected current.	91
Figure 8.7:	Output power and threshold current density as a function of the BCD.	92
Figure 8.8:	Experimental setup for the modelocking experiments.	94
Figure 8.9:	Passive modelocking results.	95
Figure 8.10:	Simulated influence of the heatsink material on the LI-curve.	98

List of Tables

Table 4.1:	Important properties of III/V-compounds.	32
Table 4.2:	Growth error analysis of a QW-SESAM.	34
Table 4.3:	Thermal conductivity of different relevant materials.	40
Table 5.1:	Beam quality measurements of our EP-VECSELs.	54
Table 6.1:	Device parameters <i>Philips U-L-M Photonics</i> EP-VECSELs.	57
Table 6.2:	Beam quality measurements <i>Philips U-L-M Photonics</i> EP-VECSELs.	58
Table 6.3	Summary of the extracted spectral gain parameters.	63
Table 6.4	Summary of the extracted gain saturation parameters.	67
Table 7.1	Overview of the realized p-DBR designs.	77
Table 7.2	Resistance and differential resistance of the improved p-DBRs.	80
Table 7.3	Comparison of the n-DBR reflectivity and the resulting field enhancement.	83
Table 8.1:	Comparison of the cw multi-mode performance of the initial and improved design.	92
Table 8.2:	Beam quality measurements as a function of the BCD.	93

Publications

Parts of this thesis are published in the following journal papers and conference proceedings.

Journal papers

1. Y. Barbarin, M. Hoffmann, W. P. Pallmann, I. Dahhan, P. Kreuter, M. Miller, J. Baier, H. Moench, M. Golling, T. Südmeyer, B. Witzigmann and U. Keller, "Electrically pumped vertical external cavity surface emitting lasers suitable for passive modelocking", *IEEE Journal of Selected Topics in Quantum Electronics* **17**(6), 1779-1786 (2011).
2. V. J. Wittwer, C. A. Zaugg, W. P. Pallmann, A. E. H. Oehler, B. Rudin, M. Hoffmann, M. Golling, Y. Barbarin, T. Südmeyer, and U. Keller, "Timing Jitter Characterization of a Free-Running SESAM Mode-locked VECSEL", *IEEE Photonics Journal* **3**(4), 658-664 (2011).
3. W. P. Pallmann, C. A. Zaugg, M. Mangold, V. J. Wittwer, H. Moench, S. Gronenborn, M. Miller, B. W. Tilma, T. Südmeyer and U. Keller, "Gain characterization and passive modelocking of electrically pumped VECSELs", *Optics Express* **20**(22), 24791-24802 (2012).
4. C. A. Zaugg, M. Hoffmann, W. P. Pallmann, V. J. Wittwer, O. D. Sieber, M. Mangold, M. Golling, K. J. Weingarten, B. W. Tilma, T. Südmeyer and U. Keller, "Low repetition rate SESAM modelocked VECSEL using an extendable active multipass-cavity approach", *Optics Express* **20**(25), 27915-27921 (2012).
5. W. P. Pallmann, C. A. Zaugg, M. Mangold, I. Dahhan, M. Golling, B. W. Tilma, B. Witzigmann and U. Keller, "Ultrafast Electrically Pumped VECSELs", *IEEE Photonics Journal* **5**(4), 1501207 (2013).

Conference papers

1. M. Hoffmann, Y. Barbarin, W. P. Pallmann, D. J. H. C. Maas, P. Kreuter, B. Witzigmann, M. Golling, T. Südmeyer and U. Keller, "Simulation, design, and characterization of electrically pumped VECSELs for future passive modelocking", *Conference on Lasers and Electro-Optics*, San Jose, USA, 2010
2. W.P. Pallmann, Y. Barbarin, M. Hoffmann, P. Kreuter, B. Witzigmann, M. Golling, T. Südmeyer and U. Keller, "Design and Continuous-Wave Characterization of Electrically Pumped VECSELs Suitable for Passive Modelocking", *European Conference on Integrated Optics*, Cambridge, United Kingdom, 2010
3. W. P. Pallmann, M. Hoffmann, P. Kreuter, I. Dahhan, B. Witzigmann, M. Golling, Y. Barbarin, T. Südmeyer and U. Keller, "Ultrafast Electrically Pumped Vertically Emitting Semiconductor Lasers", *Materials Research Center Graduate Symposium*, Zurich, Switzerland, 2010

4. W.P. Pallmann, M. Hoffmann, V. J. Wittwer, B. Rudin, P. Kreuter, B. Witzigmann, M. Golling, Y. Barbarin, T. Südmeyer and U. Keller, "Novel Ultrafast Vertically Emitting Semiconductor Lasers", *European Conference on Optical Communication*, Torino, Italy, 2010
5. Y. Barbarin, W. P. Pallmann, M. Hoffmann, I. Dahhan, P. Kreuter, M. Golling, T. Südmeyer, B. Witzigmann and U. Keller, "Electrically-Pumped VECSELs Suitable for Passive Modelocking: Design, Simulation and Characterization in Continuous Wave", *International Semiconductor Laser Conference*, Kyoto, Japan, 2010
6. M. Hoffmann, W. P. Pallmann, O. D. Sieber, V. J. Wittwer, Y. Barbarin, I. L. Krestnikov, S. S. Mikhlin, D. A. Livshits, G. Malcolm, C. Craig, T. Südmeyer and U. Keller, "All Quantum-Dot Based SESAM modelocked VECSEL with sub-picosecond Pulses", *Europhoton*, Hamburg, Germany, 2010
7. M. Hoffmann, W. P. Pallmann, I. Dahhan, B. Witzigmann, M. Golling, Y. Barbarin, T. Südmeyer and U. Keller, "Ultra-compact electrically pumped vertically emitting ultrafast semiconductor lasers", *MIT Student Exchange*, Boston, USA, 2010
8. M. Hoffmann, O. D. Sieber, W. P. Pallmann, V. J. Wittwer, Y. Barbarin, I. L. Krestnikov, S. S. Mikhlin, D. A. Livshits, G. Malcolm, C. Hamilton, T. Südmeyer and U. Keller, "All quantum-dot based femtosecond VECSEL", *Europhoton*, Hamburg, Germany, 2010 - **Post-deadline talk**
9. Y. Barbarin, M. Hoffmann, W. P. Pallmann, I. Dahhan, P. Kreuter, M. Golling, T. Südmeyer, B. Witzigmann and U. Keller, "Simulation, design and characterization of electrically-pumped VECSELs for future passive modelocking", *VCSEL day*, Torino, Italy, 2010
10. W. P. Pallmann, M. Hoffmann, J. Baier, H. Moench, I. Dahhan, B. Witzigmann, M. Golling, Y. Barbarin, T. Südmeyer and U. Keller, "Beam-quality optimization of electrically pumped VECSELs for passive modelocking" *Photonics West, LASE, Vertical External Cavity Surface Emitting Lasers*, San Francisco, USA, 2011
11. M. Hoffmann, O. D. Sieber, W. P. Pallmann, V. J. Wittwer, Y. Barbarin, I. L. Krestnikov, S. S. Mikhlin, D. A. Livshits, G. Malcolm, C. Hamilton, T. Südmeyer and U. Keller, "All quantum-dot based femtosecond VECSEL", *Photonics West, LASE, Vertical External Cavity Surface Emitting Lasers*, San Francisco, USA, 2011
12. O. D. Sieber, M. H. Hoffmann, V. J. Wittwer, W. P. Pallmann, Y. Barbarin, M. Golling, T. Südmeyer and U. Keller, "Scaling high-power ultrafast VECSELs into the femtosecond regime", *Photonics West, LASE, Vertical External Cavity Surface Emitting Lasers*, San Francisco, USA, 2011
13. V. J. Wittwer, W. P. Pallmann, A. E. H. Oehler, B. Rudin, M. Golling, Y. Barbarin, T. Südmeyer and U. Keller, "Timing jitter characterization of a quantum dot SESAM modelocked VECSEL", *Photonics West, LASE, Vertical External Surface Emitting Lasers*, San Francisco, USA, 2011
14. B. Witzigmann, I. Dahhan, P. Kreuter, Y. Barbarin, M. Hoffmann, W. P. Pallmann, M. Golling, T. Südmeyer and U. Keller, "Design and simulation of electrically pumped mode-locked VECSELs", *Photonics West, LASE, Vertical External Cavity Surface Emitting Lasers*, San Francisco, USA, 2011 - **Invited talk**
15. B. Rudin, M. Hoffmann, V. J. Wittwer, W. P. Pallmann, M. Golling, Y. Barbarin, T. Südmeyer and U. Keller, "Ultrafast semiconductor lasers in the thin disk geometry", *Latin America Optics and Photonics Conference*, Recife, Brazil, 2010 - **Invited talk**

16. O. D. Sieber, M. Hoffmann, V. J. Wittwer, W. P. Pallmann, I. L. Krestnikov, S. S. Mikhlin, D. A. Livshits, M. Golling, Y. Barbarin, T. Südmeyer and U. Keller, "Femtosecond VECSELs with up to 1 W Average Output Power", *Conference on Lasers and Electro-Optics*, Baltimore, USA, 2011
17. M. Hoffmann, O. D. Sieber, V. J. Wittwer, W. P. Pallmann, I. L. Krestnikov, S. S. Mikhlin, D. A. Livshits, M. Golling, Y. Barbarin, T. Südmeyer and U. Keller, "Femtosecond VECSELs with up to 1 W Average Output Power", *Conference on Lasers and Electro-Optics*, Munich, Germany, 2011
18. V. J. Wittwer, C. A. Zaugg, W. P. Pallmann, A. E. H. Oehler, B. Rudin, M. Hoffmann, M. Golling, Y. Barbarin, T. Südmeyer and U. Keller, "Free-Running Quantum Dot SESAM Modelocked VECSEL with Record-Low Timing Jitter", *Conference on Lasers and Electro-Optics*, Munich, Germany, 2011
19. O. D. Sieber, M. Hoffmann, V. J. Wittwer, W. P. Pallmann, I. L. Krestnikov, S. S. Mikhlin, D. A. Livshits, M. Golling, Y. Barbarin, T. Südmeyer and U. Keller, "Novel femtosecond semiconductor lasers with more than 1 W average power", *Laser Physics Workshop*, Sarajevo, Bosnia and Herzegovina, 2011 - **Invited talk**
20. C. A. Zaugg, W. P. Pallmann, M. Hoffmann, Y. Barbarin, M. Golling, I. Dahhan, T. Südmeyer, B. Witzigmann and U. Keller, "Recent advances in electrically pumped VECSELs for modelocking", *European Semiconductor Laser Workshop*, Lausanne, Switzerland, 2011
21. C. A. Zaugg, W. P. Pallmann, M. Hoffmann, I. Dahhan, B. Witzigmann, M. Golling, Y. Barbarin, T. Südmeyer and U. Keller, "Electrically pumped vertical external cavity surface emitting laser", *Materials Research Center Graduate Symposium*, Zurich, Switzerland, 2011
22. M. Golling, W. P. Pallmann, C. A. Zaugg, T. Südmeyer and U. Keller, "MBE growth of electrically pumped VECSELs", *Photonics West, LASE, Vertical External Cavity Surface Emitting Lasers*, San Francisco, USA, 2012
23. J. R. Orchard, D. T. D. Childs, L. C. Lin, B. J. Stevens, D. M. Williams, R. A. Hogg, M. Butkus, E. U. Rafailov, S. Gronenborn, J. Kolb, H. Moench, M. Miller, M. Hoffmann, Y. Barbarin, W. P. Pallmann, M. Golling, T. Südmeyer and U. Keller, "Development of EP-VECSEL for Mode Locking Applications", *Photonics West, LASE, Vertical External Cavity Surface Emitting Lasers*, San Francisco, USA, 2012
24. I. Dahhan, Y. Barbarin, M. Hoffmann, W. P. Pallmann, C. A. Zaugg, M. Golling, T. Südmeyer, U. Keller and B. Witzigmann, "Current confinement in EP-VECSELs for high power single-mode operation suitable for passive mode-locking", *Photonics Europe*, Brussels, Belgium, 2012 - **Invited talk**
25. C. A. Zaugg, M. Hoffmann, W. P. Pallmann, O. D. Sieber, V. J. Wittwer, M. Mangold, M. Golling, K. J. Weingarten, B. W. Tilma, T. Südmeyer and U. Keller, "257 MHz pulse repetition rate from a modelocked VECSEL", *Conference on Lasers and Electro-Optics*, San Jose, USA, 2012
26. C. A. Zaugg, M. Hoffmann, W. P. Pallmann, V. J. Wittwer, M. Golling, K. J. Weingarten, T. Südmeyer and U. Keller, "250 MHz modelocked VECSEL: towards low repetition rates using an extendable multi-pass approach", *Europhoton*, Stockholm, Sweden, 2012
27. W. P. Pallmann, M. Mangold, V. J. Wittwer, B. W. Tilma, H. Moench, S. Gronenborn, M. Miller, T. Südmeyer and U. Keller, "Gain characterization of electrically-pumped VECSELs", *International Semiconductor Laser Conference*, San Diego, USA, 2012
28. C. A. Zaugg, W. P. Pallmann, M. Mangold, V. J. Wittwer, H. Moench, S. Gronenborn, M. Miller, B. W. Tilma, T. Südmeyer and U. Keller, "Passively modelocked electrically pumped

XX PUBLICATIONS

- VECSELs", *Photonics West, LASE, Vertical External Cavity Surface Emitting Lasers, San Francisco, USA, 2013*
29. B. W. Tilma, W. P. Pallmann, C. A. Zaugg, M. Golling and U. Keller, "Sub-10-Picosecond Pulses from a Passively Modelocked Electrically Pumped VECSEL", *Advanced Solid-State Lasers, Paris, France, 2013*.
 30. C. A. Zaugg, W. P. Pallmann, M. Mangold, I. Dahhan, M. Golling, B. W. Tilma, B. Witzigmann and U. Keller, „SESAM-modelocked electrically pumped VECSELs emitting 6.3-ps pulses“, *Photonics West, LASE, Vertical External Cavity Surface Emitting Lasers, San Francisco, USA, 2014*

Abstract

Optically pumped vertical external-cavity surface-emitting lasers (OP-VECSELs) have shown impressive performance with high average output power in both continuous-wave (cw) and passively modelocked operation using semiconductor saturable absorber mirrors (SESAMs). Electrical pumping (EP) is a key factor for more compact and cost efficient modelocked VECSELs suitable for low-cost mass applications such as optical clock-rate distribution in microprocessors, chip-to-chip interconnects or optical telecommunication systems.

The design of an EP-VECSEL differs significantly from that of an OP-VECSEL. The EP-VECSEL gain chip must be conductive for electrical current while maintaining the excellent optical properties of OP-VECSELs. This requires a well-balanced optical-electrical tradeoff. Some of the major challenges the design of a modelocked EP-VECSEL needs to face are non-uniform current injection for large devices, localized Joule-heating due to resistive losses or free carrier absorption (FCA) due to doping necessary for electrical conductivity.

In this thesis, the design, fabrication and performance improvement of an EP-VECSEL optimized for passive modelocking are presented. In our first successful realization of an EP-VECSEL, confined Gaussian-like current injection profiles for devices up to a bottom contact diameter (BCD) of $100\text{ }\mu\text{m}$ and up to 120 mW of output power in cw multi-mode operation were demonstrated. We identified two major performance-limiting factors, namely thermal issues and insufficient beam quality for stable passively modelocked operation.

A detailed investigation of the beam quality of EP-VECSELs with different intermediate distributed Bragg reflector (DBR) reflectivity is presented and reveals important guidelines for achieving excellent beam quality with reasonable output power levels. Furthermore, an in-depth characterization of important gain properties as function of the intermediate DBR reflectivity was performed and broadens the physical understanding of these devices. Typical values for the small-signal gain, spectral bandwidth and gain saturation behavior for different values of the field

enhancement are given. Based on the results of this characterization, a passively modelocked EP-VECSEL emitting 9.5-ps pulses was demonstrated. This was an important step, showing that an EP-VECSEL with an optimized intermediate DBR reflectivity is suitable for ultrafast pulse generation.

Using an optimized EP-VECSEL gain chip, we then generated up to 170 mW of output power in cw multi-mode operation and 26 mW in fundamental transversal mode operation. This required an improvement of various design aspects of the devices. The intermediate DBR reflectivity was reduced to achieve fundamental transversal mode operation. The resulting gain-penalty was compensated by an enhanced thermal management of the EP-VECSEL gain chip. An electrical optimization of the p-doped DBR aimed for a reduction of Joule-heating in the devices due to ohmic losses. For this purpose, a p-DBR with a digital-alloy bi-parabolic grading was developed, delivering state-of-the-art electrical performance. Additionally, an optimized device geometry was derived from numerical simulations to increase the heat transfer area of the individual devices.

Passively modelocking the optimized EP-VECSELs with a low saturation fluence SESAM led to a record-low pulse duration of 6.3 ps with 6.2 mW of average output power and 7.3-ps pulses with 13.1 mW (1.1 W) of average (peak) output power, both at 1.46 GHz repetition rate. These are to the best of our knowledge the shortest pulses with the highest peak power from an EP-VECSEL to date.

Trade-offs for further output power scaling and reduced pulse durations are finally discussed. Advanced heat management will result in significantly higher average output power and will lead to compact, cost-efficient ultrafast laser sources with high power levels and GHz repetition rates.

Kurzfassung

Optisch gepumpte, oberflächenemittierende Halbleiterlaser mit einem externen Resonator (optically pumped vertical external-cavity surface-emitting lasers, OP-VECSELs) haben bereits beeindruckende Ergebnisse erzielt. Dabei sind hohe Durchschnittsleistungen im Dauerstrichbetrieb und im passiv modengekoppelten Betrieb mit Hilfe eines sättigbaren Halbleiter-Spiegels (semiconductor saturable absorber mirror, SESAM) hervorzuheben. Elektrisches Pumpen (EP) ist ein Schlüsselfaktor für kompaktere, kosteneffizientere modengekoppelte VECSEL, die für kostengünstige Massenanwendungen wie optische Taktratenverteilung in Mikroprozessoren, Chip-zu-Chip Verbindungen oder optische Telekommunikationssysteme geeignet sind.

Das Design eines EP-VECSELs unterscheidet sich signifikant von dem eines OP-VECSELs. Der EP-VECSEL Verstärkungschip muss für elektrischen Strom leitend sein, während die exzellenten optischen Eigenschaften des OP-VECSELs so gut wie möglich erhalten bleiben sollen. Dies erfordert ein ausgewogenes Verhältnis zwischen optischen und elektrischen Eigenschaften. Einige der größten Herausforderungen für das Design eines modengekoppelten EP-VECSELs sind ungleichförmige Strominjektion für große Bauelemente, lokale ohmsche Erwärmung verursacht durch resistive Verluste oder Absorption freier Träger aufgrund der eingebrachten Dotieratome, die für die elektrische Leitfähigkeit nötig sind.

Die vorliegende Doktorarbeit behandelt das Design, die Herstellung und die Leistungsverbesserung eines für passive Modenkopplung optimierten EP-VECSELs. Mit unserer ersten erfolgreichen Umsetzung eines EP-VECSELs konnten wir zeigen, dass Bauelemente bis zu einem Durchmesser des unteren Kontaktes von 100 μm räumlich begrenzte, einer Gauß'schen Verteilung ähnliche Strominjektionsprofile aufweisen. Außerdem konnte eine Ausgangsleistung von bis zu 120 mW im Dauerstrichbetrieb mit höheren transversalen Moden erzielt werden. Zwei wichtige leistungslimitierende Faktoren konnten ermittelt werden, und zwar zum einen

thermische Probleme, zum anderen unzureichende Strahlqualität, um stabilen passiv-modengekoppelten Betrieb zu erzielen.

Des Weiteren stellt diese Arbeit eine ausführliche Untersuchung der Strahlqualität von EP-VECSELn in Abhängigkeit der internen DBR-Reflektivität (DBR: distributed Bragg reflector) vor und zeigt wichtige Richtlinien auf, um hervorragende Strahlqualität mit annehmbarer Ausgangsleistung zu erzielen. Darüberhinaus wurde eine detaillierte Charakterisierung wichtiger Verstärkungseigenschaften in Abhängigkeit der internen DBR-Reflektivität durchgeführt um das physikalische Verständnis für diese Bauelemente zu erweitern. Typische Werte für die Kleinsignalverstärkung, die spektrale Bandbreite und das Sättigungsverhalten der Verstärkung für verschiedene Werte der Feldüberhöhung werden dargelegt. Diese Charakterisierung der Verstärkungsparameter führte zu einem passiv modengekoppelten EP-VECSEL mit einer Pulsdauer von 9.5 ps. Dies war ein entscheidender Zwischenschritt um zu zeigen, dass ein EP-VECSEL mit optimierter interner DBR-Reflektivität geeignet ist um ultrakurze Pulse zu erzeugen.

Mit einem optimierten EP-VECSEL Verstärkungschip erzielten wir dann bis zu 170 mW Ausgangsleistung im Dauerstrichbetrieb mit höheren transversalen Moden und 26 mW in fundamentaler transversaler Mode. Dies setzte eine Verbesserung diverser Designmerkmale der Bauelemente voraus. Die Reflektivität des internen DBRs wurde verringert um den Dauerstrichbetrieb in fundamentaler transversaler Mode zu ermöglichen. Die daraus entstehende Einbuße bezüglich der Verstärkung wurde durch verbesserte thermische Eigenschaften des EP-VECSEL Verstärkungschips kompensiert. Eine elektrische Optimierung des p-dotierten DBRs strebte eine Senkung der ohmschen Verluste in den Bauelementen an. Aus diesem Grund wurde ein p-DBR mit bi-parabolischem Materialübergang basierend auf einer digitalen Materialmischung entwickelt. Die Charakterisierung des elektrischen Widerstandes des p-DBRs lieferte Ergebnisse auf dem Stand aktueller Technik. Darüberhinaus wurde eine optimierte Geometrie der Bauelemente anhand numerischer Simulationen bestimmt um die Wärmeübertragungsfläche der einzelnen Laser zu vergrößern.

Mittels passiver Modenkopplung wurden mit den optimierten EP-VECSELn unter Verwendung eines SESAMs mit niedriger Sättigungsfluenz kürzeste Pulse mit einer Pulsdauer von 6.3 ps und einer Durchschnittsausgangsleistung von 6.2 mW

erzeugt. Des Weiteren wurden Pulse mit einer Pulsdauer von 7.3 ps und 13.1 mW (1.1 W) Durchschnittsleistung (Spitzenleistung) erzielt, beides jeweils bei einer Repetitionsrate von 1.46 GHz. Unserem aktuellen Wissensstand zufolge sind das die kürzesten Pulse mit der höchsten Spitzenleistung, die bisher mit einem EP-VECSEL erzeugt wurden.

Abschließend wird der Kompromiss zwischen einer weiteren Erhöhung der Ausgangsleistung und kürzeren Pulsen diskutiert. Eine weitere Verbesserung der thermischen Eigenschaften wird eine signifikante Erhöhung der Durchschnittsleistung ermöglichen. Dies wird zu kompakten, kosteneffizienten ultraschnellen Laserquellen mit hoher Ausgangsleistung und Repetitionsraten im GHz-Bereich führen.

Chapter 1

Introduction

Semiconductor lasers have become an important and omnipresent part of our daily life and can be found in nearly every household. They are used in CD/DVD and Bluray players, computer mice and printers. They can be found in nearly every supermarket in barcode scanners and are the key to today's long distance communication networks. Since the first demonstration of an edge-emitting laser diode in 1962 by Hall and coworkers [1], the design and performance of semiconductor lasers has improved significantly. Furthermore, the wafer-scale technology on which they are based enables a cost-efficient mass production necessary for high volume products. Aside from the edge-emitting geometry of the first diode lasers, vertically emitting diode lasers were also developed and first demonstrated in 1979 by Iga and coworkers [2]. Major advantage of the vertical emitters is the better beam quality compared to the edge-emitters.

Exploring the concept of optically pumped vertically emitting semiconductor lasers has led to a new type of laser, the optically pumped vertical external cavity surface emitting laser (OP-VECSEL). Already in 1997, the great potential of this technology was demonstrated, when more than 0.5 W of continuous wave (cw) output power in a TEM_{00} transverse-mode where obtained by Kuznetsov et al [3]. Since then, output power levels have been scaled up to 20 W in fundamental transversal-mode operation [4] or even up to 106 W in transversal multi-mode operation [5]. The reason for the excellent performance of OP-VECSELs lies in a wide range of distinct advantages [6] compared to other laser technologies:

- A high degree of design freedom can be achieved through bandgap engineering of the multi-quantum well (QW) semiconductor structure allowing the tailoring of properties like threshold behavior, output power, efficiency or emission wavelength.
- Technically mature semiconductor material systems like GaAs/AlGaAs/InGaAs or GaAs/InGaAsP/InGaAs are available for the realization of these lasers and additionally allow for a great wavelength variety of these devices.
- The disk geometry of OP-VECSELs features a nearly one-dimensional heat flow. This allows for power-scaling of the device, meaning the output power can be scaled with the pumped area [7]. Large pump-spots also reduce potential damage at high-power operation.
- Barrier-pumping of the QWs strongly relaxes constraints for the pump diodes, since a large bandwidth can be efficiently absorbed and consequently does not require narrow linewidth, temperature-stabilized pump diodes like many diode-pumped solid-state lasers (DPSSLs).
- They exhibit excellent beam quality with near-diffraction-limited output beams, since the external cavity geometry allows for precise mode-control using a curved output coupler (OC) mirror.

Additionally, the external cavity is suitable for wavelength tuning with intra-cavity filters, intra-cavity frequency doubling or modelocking. Passively modelocking VECSELs with a semiconductor saturable absorber mirror (SESAM [8]) enables the generation of pico- to femtosecond pulses [9] and has gained great interest in recent years. The first passively modelocked OP-VECSEL was demonstrated by Hoogland et al. in 2000 [10], where they obtained 22-ps pulses with an average output power of 21.6 mW at a repetition rate of 4 GHz. In the meantime, the performance has been improved significantly. Up to 5.1 W of average output power in 682-fs pulses [11] have been demonstrated in fundamental modelocking, where only a single pulse circulates in the laser cavity, and even pulses as short as 60 fs in bursts of pulses.

Modelocked operation of VECSELs has allowed these semiconductor lasers to access a whole new field of applications in science and technology. Frequency metrology, super-continuum generation or biomedical imaging are just a few examples that could greatly profit from modelocked VECSELs. Many of these applications currently rely on large and complex ultrafast solid-state lasers like titanium-sapphire systems. Modelocked VECSELs represent a cost-efficient and compact alternative.

In order to additionally allow access to low-cost applications such as optical clock-rate distribution in microprocessors, chip-to-chip interconnects or optical telecommunication systems, it is vital to reduce the complexity and size of modelocked VECSELs even further. One approach is the integration of the absorber directly into the VECSEL gain chip. This has led to the so-called MIXSEL (modelocked integrated external-cavity surface emitting laser) [12]. Using a MIXSEL gain chip, up to 6.4 W of average output power in 28-ps pulses [13] have been obtained, the highest average output power of any modelocked semiconductor laser.

A second important approach is the electrical pumping of modelocked VECSELs. Electrical pumping significantly reduces packaging requirements and the complexity of the optical setup, since there is no need for the pump diode and pump optics. However, the design of an EP-VECSEL is more complex and requires a carefully balanced trade-off between optical and electrical properties. Figure 1.1 illustrates the major differences between a passively modelocked OP-VECSEL and a passively modelocked electrically pumped VECSEL (EP-VECSEL). Since the EP-VECSEL gain chip must be conductive for electrical current, doping of the semiconductor material is essential. Low doping levels lead to high electrical losses, whereas high doping levels lead to high optical losses and heating from FCA. Furthermore, the current injection profile needs to remain homogenous and confined even for large devices to reach high output power levels.

Despite these challenges, Hadley and coworkers first demonstrated a working EP-VECSEL in 1993, obtaining 2.4 mW of cw output power in a transversal fundamental mode at a wavelength of 985 nm [14]. Ten years later in 2003, 500 mW of cw output power in transversal TEM₀₀-mode operation at 980 nm were demonstrated by the *Novalux Corporation* from their EP-VECSEL, the so-called *NECSEL* [15]. Even up to 900 mW in cw multi-mode operation were obtained.

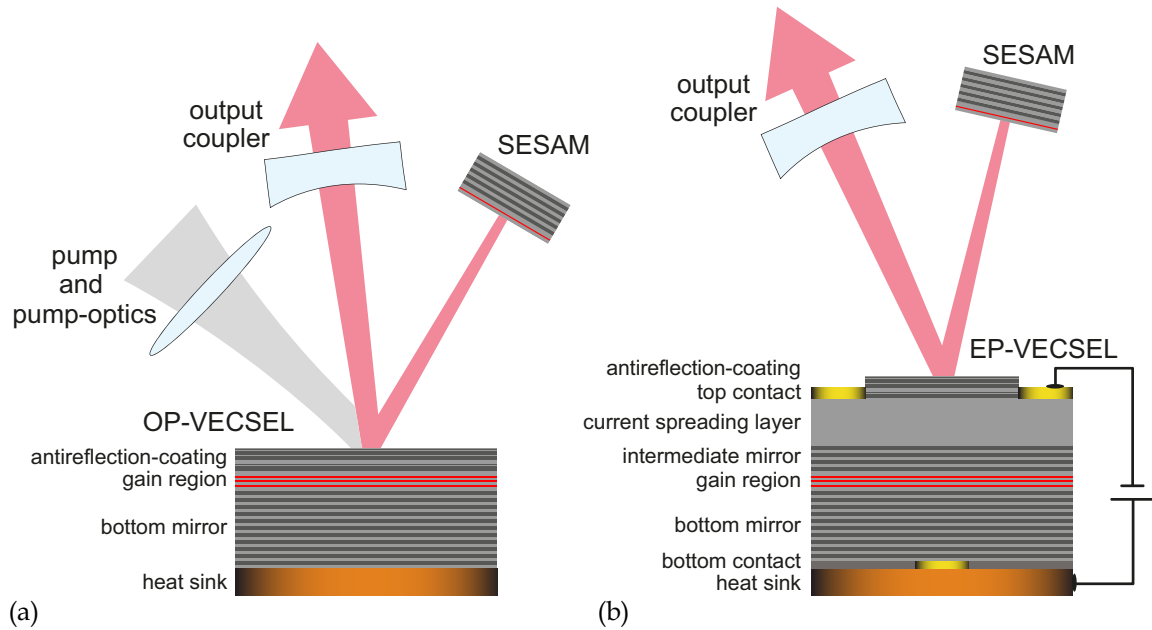


Figure 1.1 Schematic of a passively modelocked (a) OP-VECSEL and (b) EP-VECSEL (not to scale). The gain chips are in the order of a few μm , the external cavity in the range of a few cm. Electrical pumping reduces the complexity of the optical setup since pump and pump optics are not needed. On the other hand, the design and fabrication of the EP-VECSEL gain chip is more complex.

The devices were also frequency-doubled to 490 nm with 40 mW of output power [16]. Despite the impressive cw performance of the *NECSEL*, passive modelocking experiments using *NECSEL* gain chips were limited to 40 mW of average output power in 57-ps pulses [17] and tens of milliwatts with 15-ps pulses [18]. To the best of our knowledge these are the only reported passive modelocking results based on EP-VECSELs.

In the same wavelength region, 133 mW of output power in multi-mode operation [19] and 50 mW of output power frequency doubled to 1.5 mW at 485 nm [20] have been obtained. At 850 nm, 30 mW of output power in multi-mode operation were also shown from a micro-mirror EP-VECSEL [21]. In the 1.5 μm region, 2.7 mW in pulsed and 0.3 mW in cw operation were presented, limited by thermal problems, especially the high thermal resistance of the Bragg mirrors in the InP/InGaAsP-material system [22]. Also limited by thermal effects, 1.5 mW in pulsed operation was demonstrated at a wavelength of 2.34 μm using the AlAsSb/GaSb/GaInAsSb-material system [23].

It becomes evident that the realization of a passively modelocked EP-VECSEL not only requires an optimized design of the gain chip, but additionally good knowledge of device and cavity parameters to optimize the modelocking performance.

The main objective of this thesis was to realize and improve an EP-VECSEL optimized for passive modelocking. The thesis is organized as follows: First, the design of the EP-VECSELs is described in detail (Chapter 2). One of the major design differences of an EP-VECSEL gain structure compared to an OP-VECSEL is the resonant subcavity between the bottom distributed Bragg reflector (DBR) and an intermediate DBR. The subcavity increases the field enhancement and thus the gain in the active region. This is necessary to compensate losses from free carrier absorption (FCA) due to doping of the structure. The effect of the resonance on important device properties is discussed. In the following chapter, a short introduction to passive modelocking and the pulse formation mechanism in SESAM-modelocked VECSELs is given. Later, the design and the non-linear reflectivity measurement of SESAMs are introduced. In Chapter 4, the growth and the processing scheme of the EP-VECSELs are described. The cw lasing performance and the limitations of our first realization of EP-VECSELs are presented in Chapter 5.

Chapter 6 of this thesis focuses on the beam quality and gain characterization of EP-VECSELs. To gain deeper insight into how the resonance of the structure affects the device characteristics, EP-VECSELs with different reflectivity of the intermediate DBR and thus field enhancement were characterized. First, the influence of the intermediate DBR reflectivity on the beam quality is investigated. This study allowed us to determine design guidelines for our own future designs to achieve good beam quality with reasonable output power. In the following section, the gain as function of the field enhancement is characterized. Good knowledge of the gain properties is important for designing modelocking experiments and numerical modeling of the devices. From spectral gain measurements, gain bandwidth and small-signal gain are extracted. Subsequently, gain saturation measurements are described. From these measurements, the saturation fluence, small-signal gain, non-saturable losses and induced absorption effects can be determined. Passive modelocking experiments using the most suitable characterized EP-VECSEL are then described.

In Chapter 7 of this thesis, an improved design for an EP-VECSEL optimized for passive modelocking is presented. First, all improvements are discussed and then an overview is given over the optimized design. In the first section of Chapter 8, the new EP-VECSEL gain chip is characterized in cw operation. In the following section, passive modelocking experiments with the improved EP-VECSELs are described. At the end of this chapter, limitations for the output power and pulse duration are discussed and approaches for improved performance are presented.

Finally, this thesis concludes with a summary of all presented results that have led to the demonstration of a passively modelocked EP-VECSEL emitting ultrashort pulses. Furthermore, an outlook for this technology is given.

Chapter 2

Electrically pumped VECSELs

EP-VECSELs belong to the class of surface emitting lasers. In comparison to VCSELs (vertical cavity surface emitting lasers), the laser cavity is completed only with an additional cavity element, for instance an OC mirror. Like for VCSELs, their pump profile is given purely by the geometry, material and doping scheme. For OP-VECSELs, the pump profile can be independently designed of the gain structure by adapting the pump and the pump optics. Consequently, the design of an EP-VECSEL differs significantly from that of an OP-VECSEL. Furthermore, the EP-VECSEL gain chip must be conductive for electrical current while trying to maintain the excellent optical properties of an OP-VECSEL as good as possible. Some of the challenges that arise from electrical pumping are non-uniform current injection for large devices, current crowding, localized Joule-heating due to resistive losses or FCA resulting in optical losses and excess heat, only to mention a few. Some general design guidelines and a detailed description of our initial design will be given in this chapter and the optical-electrical tradeoff will be discussed. The simulation tools for the design and improvement of EP-VECSELs will be briefly described at the end of the chapter.

2.1 General design considerations

The design of an EP-VECSEL is crucial for achieving good beam quality at high output powers. Additional factors like moderate group delay dispersion (GDD) and gain bandwidth also need to be considered at the same time to optimize the design for passively modelocked operation.

2.1.1 Current confinement

For fundamental transversal-mode operation, a confined, Gaussian-like current injection profile is essential. To achieve this, there are several design parameters that can be adapted. The geometry of the devices, the doping scheme, the use of a current spreading layer (CSL), an oxide aperture or a tunnel junction are just some of the choices to be made. To have a good starting point, we developed design guidelines based on numerical simulations [24]. Figure 2.1 shows a schematic of our resulting EP-VECSEL design.

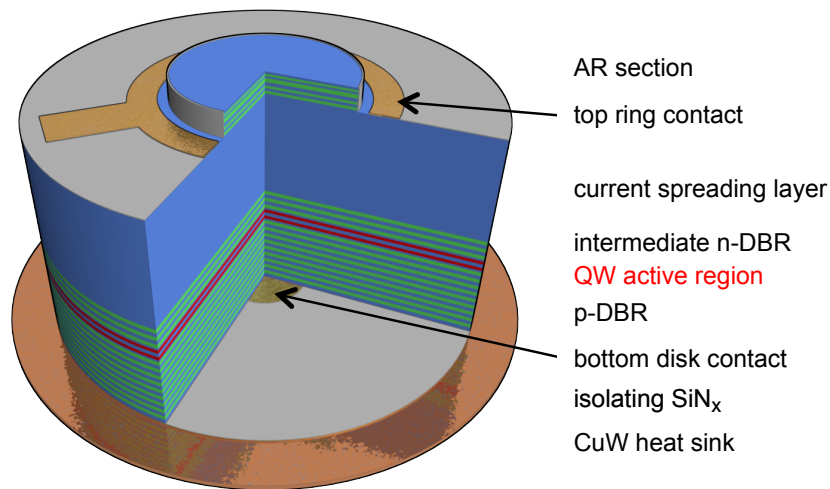


Figure 2.1 Schematic of the EP-VECSEL gain chip on a copper-tungsten (CuW) heat sink (not to scale): Bottom disc contact and top ring electrode inject current into the structure. The p-DBR acts as end mirror for the laser wavelength. The gain section consists of several QWs, the partial-reflective intermediate n-DBR increases the field enhancement. The current spreading layer (CSL) supports a homogeneous current injection to the center of the device. The anti-reflection (AR) section reduces unwanted sub-cavity effects from the CSL. For lasing operation, a second mirror like a curved OC is necessary (not shown). SiN_x: silicon nitride.

Current is injected into the device through a disk-shaped bottom contact underneath the p-doped, highly reflecting DBR (p-DBR) and through a top ring electrode. The holes in the p-doped region have a lower mobility compared to the electrons in the n-doped region. Consequently, they remain in the center of the device in the volume above the bottom contact, whereas the highly mobile electrons move through the current spreading layer (CSL) to the center of the structure with the QW gain layers. There, they recombine with the holes [24]. Thus, the CSL

together with the bottom disk contact below the p-doped region create a confined inversion profile to support a fundamental transversal lasing mode.

2.1.2 Field enhancement and gain

As mentioned earlier, doping of the EP-VECSEL gain structure is a necessity to reduce electrical losses. Still, already moderate doping levels lead to increased optical losses from FCA. The FCA coefficient α_{FCA} of doped GaAs is given as

$$\alpha_{\text{FCA}} = 5 \cdot 10^{-18} \text{ cm}^2 \cdot n + 1.1 \cdot 10^{-17} \text{ cm}^2 \cdot p , \quad (2.1)$$

where n and p are the electron and hole densities in cm^{-3} , respectively [24]. The electron and hole densities can be approximated by the doping concentrations N_{D} and N_{A} . Considering a plane wave approach and neglecting standing wave effects, the optical round-trip losses l_{r} can be estimated using the *Lambert-Beer* law:

$$l_{\text{r}} \approx 1 - e^{-\alpha_{\text{FCA}} \cdot 2d} , \quad (2.2)$$

where d is the thickness of the layer. For a CSL thickness of $d = 6 \mu\text{m}$ with a moderate doping level of $N_{\text{D}} = 2 \cdot 10^{18} \text{ cm}^{-3}$ this already corresponds to losses in the range of $l_{\text{r}} \approx 1.2\%$. To compensate these additional losses, the modal gain of the device needs to be increased. This can be achieved by using an intermediate n-doped DBR (n-DBR), as shown in Figure 2.1. This partly reflective mirror creates a resonant subcavity with the p-DBR and increases the field enhancement Γ in the active region at the position of the QWs. Γ is wavelength-dependent and can be defined as:

$$\Gamma = \frac{1}{N_{\text{QW}}} \sum_{\text{QWs}} |\mathcal{E}(z)|^2 , \quad (2.3)$$

where N_{QW} is the number of quantum wells and $\mathcal{E}(z)$ the electric field at the position of the QWs z . The overall gain is then given by the power reflectivity coefficient

$$G(\lambda) = \frac{P_{\text{out}}}{P_{\text{in}}} = 1 + N_{\text{QW}} \Gamma(\lambda) g(\lambda, N) n_{\text{r}} d_{\text{QW}} , \quad (2.4)$$

where $g(\lambda, N)$ is the intrinsic QW gain, given as a function of the wavelength and the carrier density, n_{r} is the real part of the refractive index and d_{QW} corresponds to the QW thickness.

Considering Equation (2.4), increasing the number of QWs is one possibility to increase the gain of the device. However, this would also lead to an increased thickness of the active region. Since the active region is located in the undoped region between the p-doped and n-doped part of the device, increasing the thickness leads to a strong increase in electrical resistance and is therefore not desirable.

The other more favorable possibility is to increase the field enhancement. This can be achieved by increasing the number of quarter-wave layer pairs in the n-DBR. Figure 2.2(a) shows the wavelength-dependence of the field enhancement in the QW active region for 7, 9, and 11 n-DBR pairs each consisting both of a quarter-wave layer of AlAs and GaAs.

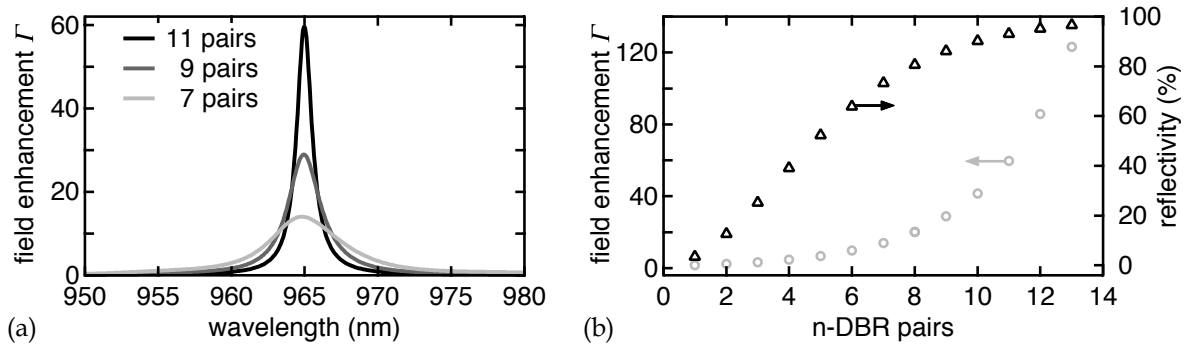


Figure 2.2 Field enhancement in the active region of the EP-VECSEL as function of the number of n-DBR pairs. (a) Wavelength-dependence of the field enhancement for 7, 9 and 11 n-DBR pairs and (b) maximum field enhancement and resulting reflectivity of the n-DBR for a different number of n-DBR pairs.

For 11 n-DBR pairs, the field enhancement shows a very strong dependence on the wavelength, a bandwidth of around 1.25 nm full width at half maximum (FWHM) is obtainable. At the same time, values of nearly 60 for the field enhancement are reached. Reducing the number of pairs to 9 or even 7 decreases the spectral filtering effect, but also reduces the achievable field enhancement. Values of 29 and 14 for the field enhancement and 2.45 nm and 5.7 nm for the bandwidth (FWHM) are obtainable, respectively. Figure 2.2(b) shows the field enhancement and the resulting reflectivity of the n-DBR as a function of the number of n-DBR pairs. For 11 pairs, a reflectivity of nearly 93% is already reached.

2.1.3 Optimization for modelocked operation

To obtain short pulses with high average output power, it is important to optimize the structure not only for highest possible cw single-mode power, but also for modelocked operation. The two most important parameters for short pulses are a large gain bandwidth and moderate values for the GDD [25]. From Figure 2.2(a), we have already learned that reducing the number of n-DBR pairs leads to a higher bandwidth of the gain and is therefore beneficial for obtaining short pulses. Figure 2.3(a) shows the influence of the AR-coating on the wavelength-dependent field enhancement. Without the AR-coating, the CSL acts like a Fabry-Perot etalon. This leads to additional modulations on the wavelength-dependent field enhancement and reduces the bandwidth of the gain.

The second important parameter for short pulses is the GDD. The GDD coefficient $D(\omega)$ is given by

$$D(\omega) = \frac{d^2\phi(\omega)}{d\omega^2}, \quad (2.5)$$

with the phase $\phi(\omega)$. D is usually expressed in fs² or ps² for very high values. Figure 2.3(b) shows the wavelength-dependent GDD as function of the number of n-DBR pairs.

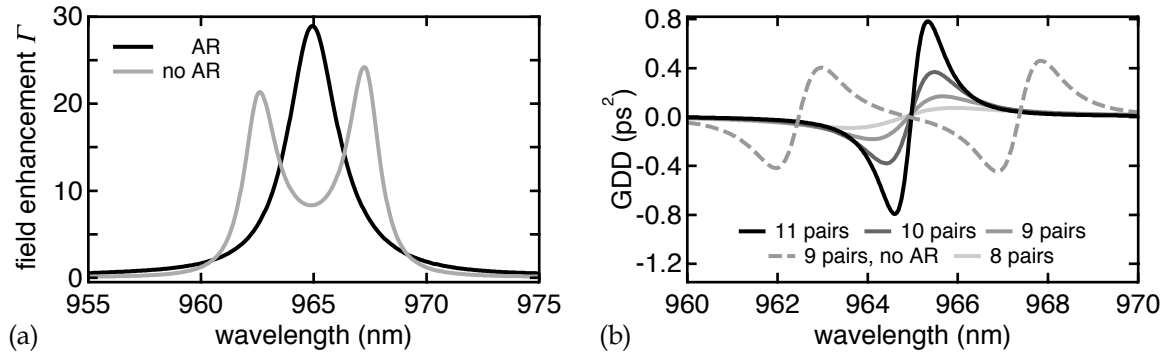


Figure 2.3 (a) Wavelength-dependent field enhancement in the QWs with (black) and without (gray) an AR coating on the device. The AR-coating reduces sub-cavity effects resulting from the CSL, which acts as a Fabry-Perot-etalon. (b) GDD as a function of the wavelength and the number of n-DBR pairs, with an AR-coating. Due to the resonance, the GDD values are very high and strongly wavelength-dependent around the resonance. Without an AR-coating, the maximum values of the GDD are even higher (dashed gray).

For an EP-VECSEL with 11 n-DBR pairs, the reached values around the resonance are in the order of nearly 0.8 ps^2 . Reducing the number of pairs leads to a less wavelength-dependent distribution of the GDD with much lower absolute values. For 9 n-DBR pairs, the GDD distribution without an AR-coating on the device is plotted additionally. In this case, the maximum values of the GDD are much higher.

Both for the gain bandwidth and the GDD distribution, a reduced n-DBR reflectivity in combination with an AR-coating is beneficial. However, a trade-off in regards to output power due to the reduced gain needs to be accepted for a lower number of n-DBR pairs.

Figure 2.4 shows an estimation for the obtainable pulse duration from a passively modelocked EP-VECSEL as function of the GDD and the gain bandwidth. The estimation is based on a numerical model of the pulse formation process in passively modelocked VECSELs [26].

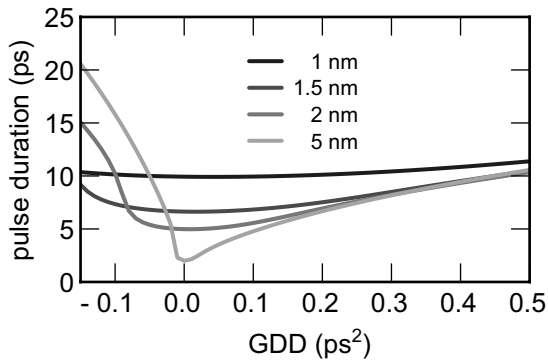


Figure 2.4 Estimation for the obtainable pulse duration of a passively modelocked EP-VECSEL as function of the GDD and the gain bandwidth. The estimation is based on numerical pulse shaping simulations [26].

If we consider an EP-VECSEL with 9 n-DBR pairs, a gain bandwidth of more than 2 nm should be available (Figure 2.2(a)). The maximum GDD value for this number of n-DBR pairs is below 0.2 ps^2 (Figure 2.3(b)). This results in an obtainable pulse duration of around 6 ps.

2.2 Design details and wafer growth

Figure 2.5 shows the initial design of the EP-VECSEL gain chip. The refractive index profile is represented in black, the squared electric field in green. The field enhancement in the active region is increased due to the resonant subcavity between p- and n-DBR (see Section 2.1.2). The bulk doping levels are given on top of the schematic.

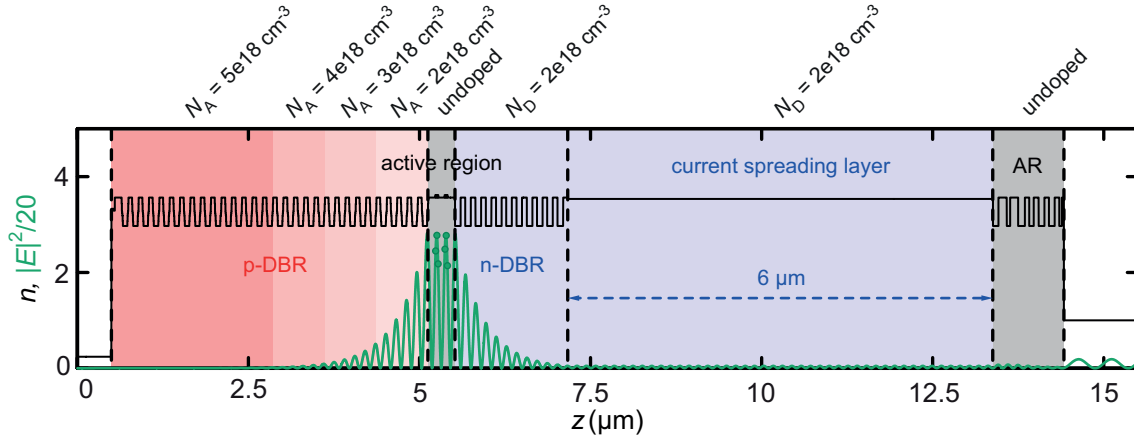


Figure 2.5 Initial design of the electrically pumped VECSEL gain chip. The black lines represent the refractive index profile, the green lines the squared electric field. The QWs are placed in the antinode of the standing wave pattern, indicated by a green dot. The bulk doping levels of the structure are given on top.

The first layer on the p-side is the p-contact layer (not shown) consisting of a 100-nm thick GaAs layer. It is p-doped with carbon (C) at a doping concentration of $3 \cdot 10^{19} \text{ cm}^{-3}$. This is necessary to obtain an ohmic contact at the semiconductor-metal interface of the electrical contacts. The p-DBR consists of 30 quarter-wave layer pairs of AlAs/GaAs with doping levels of $(5, 4, 3, 2) \cdot 10^{18} \text{ cm}^{-3}$ for the DBR pairs (1 - 15, 16 - 20, 21 - 25, 26 - 30), respectively. This doping scheme helps to reduce electrical losses while only slightly increasing optical losses, since the electric field at the beginning of the p-DBR is low, limiting losses from FCA. At the AlAs/GaAs material interfaces, a 16-nm thick molefraction grading is applied to smoothen the valence band discontinuities at these hetero-interfaces. This will be discussed in more detail in Chapter 7. In our initial design, we used five discrete $\text{Al}_x\text{Ga}_{(1-x)}\text{As}$ layers of different molefraction x [27].

With a linear grading [28] better electrical performance can be expected, but MBE growth of such a grading is challenging. Consequently, it was not implemented in our first design.

The active region consists of 2×3 $\text{In}_{(x)}\text{Ga}_{(1-x)}\text{As}$ QWs embedded in undoped GaAs positioned in two adjacent antinodes of the standing wave pattern (green dots in Figure 2.5). In both antinodes they are spaced by 10 nm of GaAs. The device is designed for an internal operation temperature of $\approx 100^\circ\text{C}$ and a wavelength of 965 nm. Therefore, the peak photoluminescence (PL) of the QWs at room temperature is detuned by 25 nm from the design wavelength of 965 nm to ensure maximum gain at high current injection and thus high temperature [16].

The partially reflective intermediate n-doped DBR (n-DBR) consists of 11 AlAs/GaAs quarter-wave layer pairs. This results in a reflectivity of the n-DBR of nearly 93%. The doping concentration level is held constant at $2 \cdot 10^{18} \text{ cm}^{-3}$, the dopant is silicon (Si). A molefraction grading is not used in the n-DBR, since the expected reduction in electrical resistance is minor compared to the contribution from the p-DBR [24]. In our first realization the number of pairs was chosen at a high value of 11 to ensure lasing in cw operation.

The GaAs CSL is 6- μm thick and n-doped at a concentration of $2 \cdot 10^{18} \text{ cm}^{-3}$. Between the CSL and the following AR section, the 150-nm thick GaAs n-contact layer at a doping concentration of $6 \cdot 10^{18} \text{ cm}^{-3}$ is inserted. The AR section is undoped and consists of 14 AlAs/GaAs layer pairs. The individual layer thicknesses were optimized for low reflectivity in an 8-nm broad wavelength region around the design wavelength of 965 nm. The algorithm for this was a combination of a Monte Carlo procedure in combination with a least-squares fit algorithm.

The EP-VECSEL gain chip is grown in reverse order by molecular beam epitaxy (MBE) on an intrinsically doped GaAs substrate. Growth in reverse order allows for substrate removal, significantly improving the thermal management of the device. A 300-nm thick $\text{Al}_{0.85}\text{Ga}_{0.15}\text{As}$ layer between substrate and device acts as an etch-stop layer. The etch-stop is an important part of the substrate removal process. The complete processing scheme will be described later in Chapter 4.

2.3 Simulation of EP-VECSELS

To design and optimize our devices, we use two important simulation tools. One is a program for the design of multilayer structures; the other is a coupled electro-opto-thermal numerical model of the EP-VECSEL. Both will be briefly described in this section.

2.3.1 *Multilayer structure simulation*

The EP-VECSEL gain structure consists of typically several hundred layers with a total thickness of up to 13.5 μm . Under the assumption of an incident plane wave, the electric field in- and outside of the device can be calculated using a transfer matrix algorithm [29]. A program based on this algorithm allows us to design and characterize our multilayer structures. Quantities like the electric field standing wave pattern, the wavelength-dependent field enhancement or the GDD distribution can be directly calculated with this program.

2.3.2 *EP-VECSEL numerical simulations*

The coupled electro-opto-thermal numerical model of the EP-VECSEL is described in [24, 30] and was developed in a collaboration with the group of Prof. B. Witzigmann at the University of Kassel. It uses a multi-dimensional model based on microscopic theory for the description of the physical properties in the device.

A drift-diffusion model is used for the calculation of carrier transport. The continuity equation is implemented to solve for the hole and electron densities and the Poisson equation for the electrostatic potential. A thermodynamic model complements the equations and solves for the temperature, whereas the transport equations are modified to include the temperature as an additional carrier driving force. A thermionic emission model addresses the abrupt hetero-interfaces. The QWs in the active region are modeled as scattering centers of the bulk carriers, separating the carrier population into bulk unbound and QW population obeying the solution of the Schrödinger equation. The optical problem is solved with a transfer matrix method coupled with an effective index method. The model delivers a self-consistent solution and device variables like carrier distribution, current densities or internal temperature can be derived. From the simulation model we are able to extract guidelines and trends for the design and improvement of our EP-VECSELS.

Chapter 3

Passively Modelocked VECSELs

Lasers can operate in different operation modes. Besides emitting in cw mode with constant power, pulsed operation is also possible, where the laser emits a train of consecutive pulses. There are various techniques for achieving pulsed operation. One possibility lies in the modulation of the quality factor (Q -factor) of the laser cavity. Hence, this method is referred to as Q -switching [31, 32]. With this technique, short pulses in the nanosecond down to the picosecond range can be generated with high pulse energies. The repetition rate of the pulses lies in the order of a few Hz up to a few MHz, but does not necessarily correspond to the frequency set by the cavity round-trip time.

Much shorter pulses down to a few femtoseconds can be achieved by using modelocking techniques. The pulses are then formed by constructive interference of the different axial modes of the laser. This means that a fixed phase relationship exists between these modes, or in other words that they are ‘locked’ to each other in phase, hence, the term ‘modelocking’. The more modes that are locked to each other, the broader the spectral bandwidth and the shorter the resulting pulses. This technique was first described by DiDomenico [33], Hargrove [34] and Yariv [35] and will be discussed in more detail in the following section.

Q -switching and modelocking may also occur simultaneously. In the so-called Q -switched modelocking (QML) regime, a pulse train of pico- or femtosecond pulses is modulated by an envelope of microsecond Q -switched pulses at a much lower repetition rate. Especially for modelocked DPSSL, QML instabilities are a major issue, since they may lead to damage of intra-cavity elements like mirrors or

SESAMs. VECSELs have the advantage of a large gain cross-section, which suppresses Q -switching instabilities [36]. This makes them ideally suited for high-repetition rate modelocking with high average output power.

In this chapter the basics of passive modelocking with a saturable absorber will be explained. Special attention will then be paid to the pulse formation process in passively modelocked VECSELs. The concept of the SESAM will be introduced, including the different device parameters and design possibilities. Finally, the measurement setup for the characterization of important SESAM parameters will be described.

3.1 Active and passive modelocking

The requirement for achieving modelocked operation is a loss modulation, which provides a larger net gain for pulsed operation than for cw operation. This loss modulation can be either active or passive. Figure 3.1 shows the laser cavity and loss modulation for an actively and passively modelocked laser. For active modelocking (Figure 3.1(a)), the losses in the cavity are modulated by an externally driven element like an acousto-optic or electro-optic modulator (AOM or EOM). Net gain is only obtained at the minimum of the sinusoidal loss modulation, opening a window for pulsed operation. If the loss modulation is synchronized to the cavity round-trip time T_R , a pulse is built up within the net gain window. The typical pulse duration that can be obtained from an actively modelocked laser is in the picosecond range. Much shorter pulses can be obtained using passive modelocking. This requires a cavity element with an intensity-dependent loss like a saturable absorber. In this case, the loss of the saturable absorber is modulated by the pulse itself (Figure 3.1(b)).

Each time the pulse passes over the OC, a small fraction of the power is coupled out and a pulse is emitted. This results in a pulse train where the repetition rate is given by the cavity round-trip frequency

$$f_{\text{rep}} = \frac{c_0}{2L} , \quad (3.1)$$

where c_0 is the speed of light and L is the optical cavity length. Of course this only holds if a single pulse circulates in the laser cavity and is referred to as fundamental modelocking.

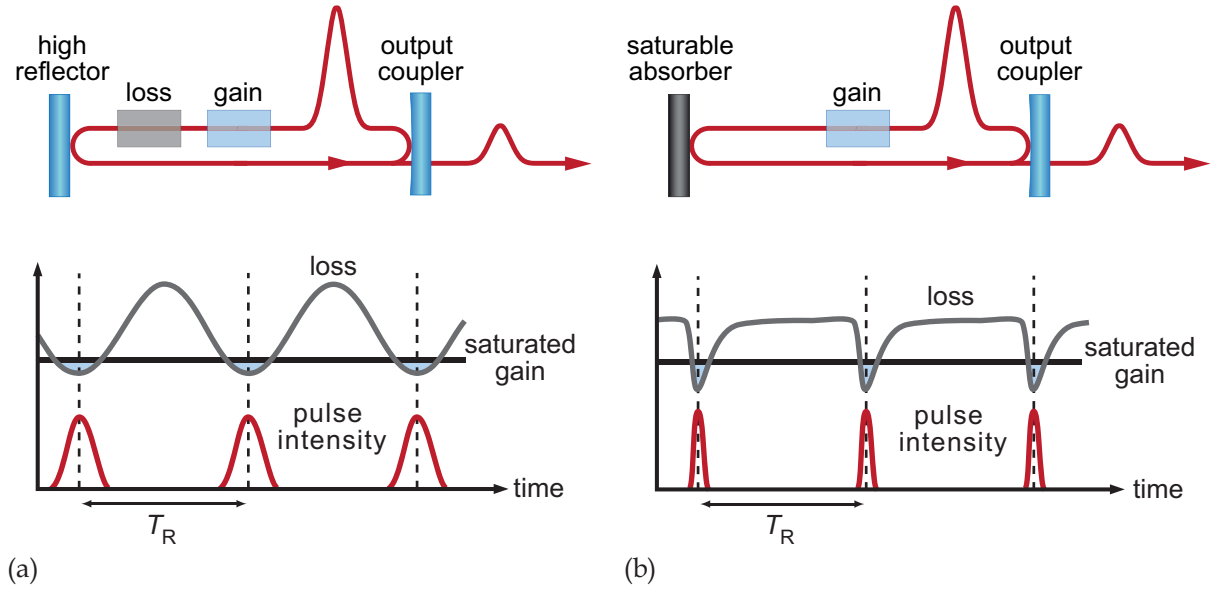


Figure 3.1 Laser cavity and loss modulation for active and passive modelocking. (a) For active modelocking, the losses in the cavity are modulated by an optical switch driven by an externally applied signal. Net gain is only obtained at the minimum of the sinusoidal loss modulation, opening a window for pulsed operation. (b) For passive modelocking, the loss of the saturable absorber is modulated by the pulse itself. The saturable absorber can be integrated into a mirror and act as a cavity end mirror.

It is also possible to operate with multiple, evenly spaced pulses in the so-called harmonic modelocking regime. However, fundamentally modelocked operation exhibits better noise performance for both intensity noise and timing jitter. Furthermore, pulse drop-outs cannot occur. Hence, fundamental modelocking is usually the preferred operation regime. Typical repetition rates of modelocked lasers range from a few MHz even up to hundreds of GHz [37].

3.2 Mechanisms of passive modelocking

Passive modelocking using a saturable absorber can be classified by three different mechanisms [9], shown in Figure 3.2. Generally, the classification depends on the recovery time of the absorber. If the recovery time is much smaller than the pulse duration, the saturable absorber is called fast. If it is the other way around, the saturable absorber is referred to as slow. This case is further split up depending on the gain saturation of the gain material. In all three cases there is a net gain window during a short time period, where the pulse can be amplified.

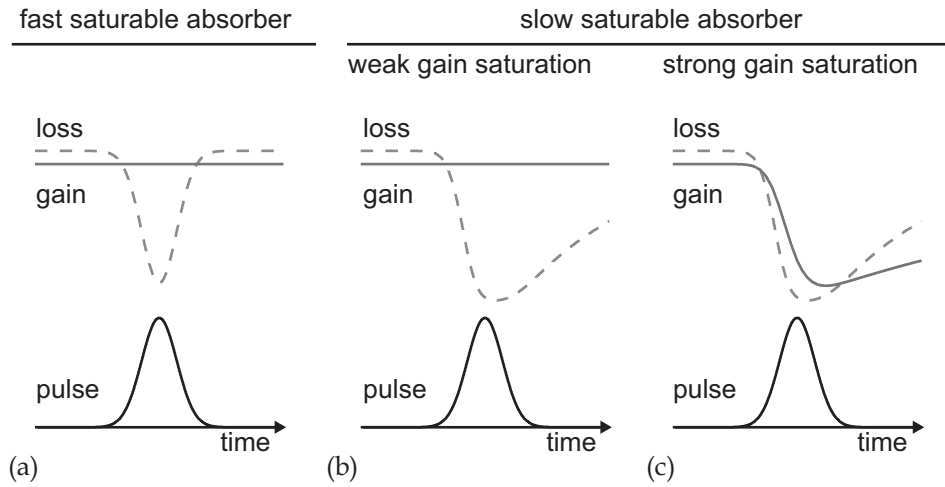


Figure 3.2 Different mechanisms of passive modelocking using a saturable absorber. (a) Fast saturable absorber with a recovery time shorter than the pulse duration. (b) Slow saturable absorber with weak gain saturation and (c) strong gain saturation.

3.2.1 Fast saturable absorber

Passive modelocking with a fast saturable absorber is shown in Figure 3.2(a). Constant gain is assumed and the recovery time of the absorber dominates the pulse characteristics. A typical example of this modelocking regime is Kerr-lens modelocking (KLM) [38, 39]. In KLM, the Kerr non-linearity leads to an intensity-dependent lensing effect of the gain material, also referred to as self-focusing. If the cavity is operated at the stability limit or with an intra-cavity aperture, the self-focusing effect leads to a reduction in losses and thus favors modelocked operation. Response and recovery time for this effect are in the range of a few femtoseconds. Consequently, the shortest pulses from a modelocked laser have been obtained with this method [40, 41]. On the downside, this technique is not self-starting, but needs an external disturbance. Furthermore, operation at the stability limit of the cavity makes long-term stable operation challenging.

3.2.2 Slow saturable absorber with constant gain

Weak gain saturation can be found in many solid-state materials, since they exhibit a typical upper state lifetime in the micro- or even millisecond range. Furthermore, they have a significantly smaller gain cross-section than semiconductor or dye lasers. The resulting saturation energy of the gain material is significantly larger than typical intra-cavity pulse energies. Therefore, constant gain can be assumed. The combination of constant gain with a slow saturable absorber is shown in

Figure 3.2(b). The resulting net gain window is wide and after saturating the absorber there seems to be no mechanism, which favors pulsed operation over cw operation. Nevertheless, stable modelocked operation can be achieved in this regime. The reason is the following: the leading edge of the pulse is absorbed much stronger by the saturable absorber on each cavity round-trip than the trailing edge. This leads to a constant time shift of the pulse, also shifting the net gain-window on each round-trip. The background cw noise on the other hand is not shifted back and consequently moves out of the net gain window. Using numerical simulations it has been shown that pulses even twenty times shorter than the recovery time of the absorber can be achieved in this regime [42]. Typical pulse durations are in the order of a few picoseconds.

In this modelocking regime, significantly shorter pulses in the femtosecond range can be obtained. This requires an additional pulse-shaping mechanism. Most commonly found in femtosecond DPSSLs is soliton-modelocking [43]. Soliton-modelocking is based on an interplay of negative GDD and self-phase modulation (SPM). If GDD and SPM are properly balanced, they compensate each other in such a way that the soliton shape (sech²-pulse, hyperbolic secant squared envelope) is maintained in the time and frequency domain. Nevertheless, the saturable absorber still plays an important role. It starts modelocked operation and prevents the cw background from growing. Pulses as short as 46 fs have been obtained with this technique [44].

3.2.3 *Slow saturable absorber with strong gain saturation*

Semiconductor lasers, just like dye lasers [45], exhibit a short upper state lifetime in the order of nanoseconds in combination with a high gain cross-section. This leads to low saturation energies of the gain and means that the pulse can saturate the gain. This results in a narrow net gain window for the pulse, as it can be seen in Figure 3.2(c). For obtaining stable modelocked operation in this regime it is essential, that the absorber saturates at lower pulse energies than the gain.

3.3 Pulse formation in passively modelocked VECSELs

3.3.1 Gain and absorber saturation

The passively modelocked EP-VECSELs described in this thesis belong to the class of semiconductor lasers and their modelocking mechanism is therefore based on the slow saturable absorber in combination with strong gain saturation. The condition for stable modelocked operation in this regime is given by

$$\frac{E_{\text{sat,abs}}}{E_{\text{sat,gain}}} = \frac{A_{\text{abs}} \cdot F_{\text{sat,abs}}}{A_{\text{gain}} \cdot F_{\text{sat,gain}}} \ll 1, \quad (3.2)$$

where $E_{\text{sat,abs/gain}}$ is the saturation energy, $A_{\text{abs/gain}}$ is the cavity mode area and $F_{\text{sat,abs/gain}}$ is the saturation fluence, each for the absorber and gain, respectively. This equation can be satisfied by either choosing a saturable absorber with a lower saturation fluence than the gain or by using a smaller spot size on the absorber.

In our experiments we use semiconductor saturable absorber mirrors (SESAMs) to start and stabilize modelocked operation. Absorber parameters of SESAMs can be adapted over a wide range to match the requirements given by this modelocking mechanism. Their design and characterization will be described in detail in the following section. Before that, the pulse formation in passively modelocked VECSELs will be explained in more detail.

3.3.2 Quasi-soliton modelocking

Besides the pulse shaping characteristics given by the gain and absorber saturation, an additional pulse formation mechanism can be found in passively modelocked VECSELs. It is a soliton-like pulse shaping mechanism already discovered by Martinez et al. in passively modelocked dye lasers [46]. Whereas ordinary solitons are based on an interplay of dispersion and the Kerr effect (Section 3.2.2), quasi-solitons involve non-linear index changes in the gain medium and the saturable absorber in combination with positive dispersion.

Due to the Kramers-Kronig relation, the dynamic behavior of the gain and absorber also result in temporal changes in the refractive indices [25]. These changes in the refractive indices lead to phase shifts.

They are shown in Figure 3.3(a) for a picosecond pulse. The sum of the phase shift from the gain medium and the absorber gives the total phase shift.

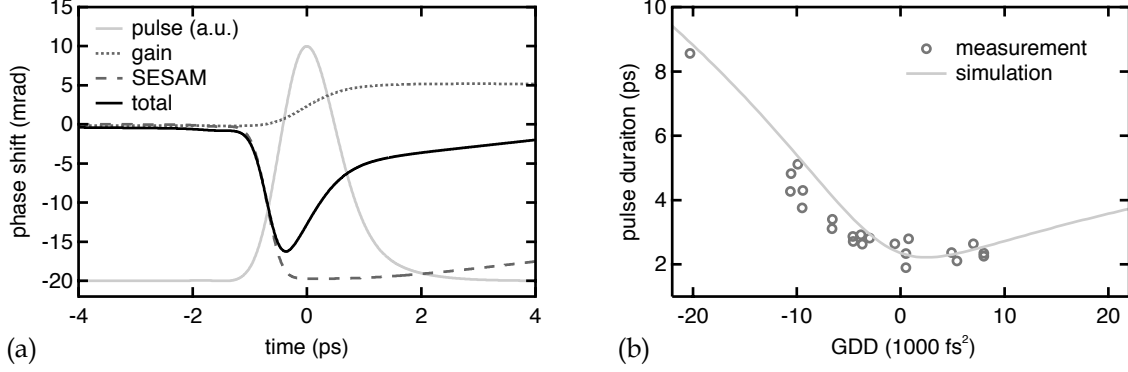


Figure 3.3 Soliton-like pulse shaping mechanism in VECSELS. (a) Non-linear phase shift from the gain medium and the absorber as well as the resulting total phase shift. The positive cavity dispersion compensates this phase shift, resulting in a quasi-soliton. The intensity profile of the pulse is shown in the background in gray. (b) Measured and simulated influence of the GDD on the pulse duration.

The total phase shift is similar to the phase shift coming from SPM in soliton modelocked SSLs, but with an opposite sign. Therefore, positive dispersion is needed to balance these phase shifts to obtain stable modelocked operation in passively modelocked VECSELS. This mechanism is referred to as quasi-soliton modelocking. Quasi-solitons share some properties of ordinary solitons like their stability and near bandwidth-limited nature. On the other hand, the pulse duration scales strongly with the cavity dispersion. The quasi-soliton mechanism was experimentally verified in the picosecond regime [47] and in the femtosecond regime [26] by comparing pulse propagation simulations with real experiments. Figure 3.3(b) shows the simulated influence of the GDD on the pulse duration and the GDD-dependent measurements of the pulse duration.

3.4 Semiconductor saturable absorber mirrors

Semiconductor materials combine many advantages and are ideally suited to be used as saturable absorber:

- Bandgap engineering makes it possible to adapt their design for different laser systems in a wide wavelength range.
- Their saturation-intensities lie in the range typically found in different types of solid-state lasers.
- The recombination dynamics of the absorber can be directly controlled by varying defect density, growth temperature and material composition.

3.4.1 Carrier dynamics in semiconductor absorbers

The semiconductor absorbers typically used in SESAMs consist of one or several QWs or quantum dot (QD) layers. If the photon energy E_{photon} is larger than the bandgap of the chosen semiconductor, photons are absorbed and excite electrons into the conduction band (CB) (Figure 3.4). On a timescale of around 100 fs, the carriers subsequently thermalize. Finally, they recombine or get captured by mid-gap traps; the absorber recovers completely.

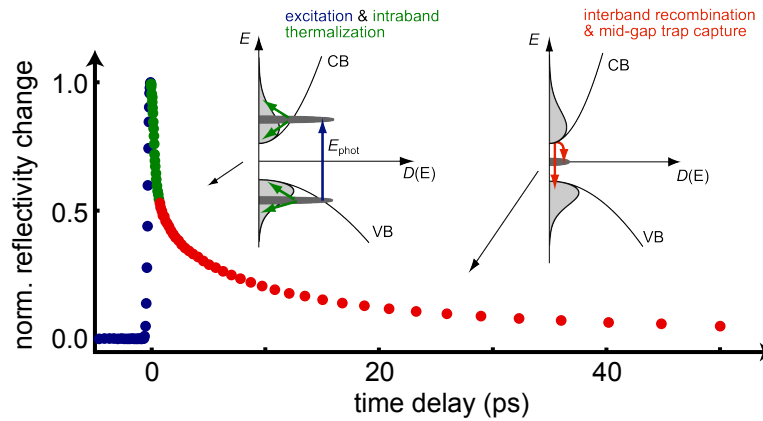


Figure 3.4 Carrier dynamics in a SESAM. The graph shows the normalized reflectivity change as a function of the time delay, revealing the recovery dynamics of the SESAM. The insets show the responsible processes: Electrons are excited from the valence band (VB) into the conduction band (CB) (blue). On a timescale of around 100 fs they thermalize (green). Finally, they recombine or get trapped (red), the absorber recovers completely. This happens on a timescale of a few picoseconds to nanoseconds.

This happens on a longer timescale of a few picoseconds to nanoseconds. These two fundamental recovery processes lead to the double exponential recovery behavior.

The absorber can be directly combined with a DBR since both elements can be realized using semiconductor materials. The absorber is then directly grown on top of a highly reflective DBR. This device is referred to as a semiconductor saturable absorber mirror or short: SESAM [8, 48]. It can replace one of the cavity mirrors and makes the cavity design much more simple compared to other technologies like KLM.

3.4.2 SESAM design and parameters

SESAMs typically consist of a DBR and the absorber section. Additionally, they may have a semiconductor or dielectric top-coating to change the field enhancement or the GDD of the structure. Figure 3.5 shows two different SESAMs, one with an antiresonant and the other with a resonant design [49]. Both SESAMs have a 30 pair AlAs/GaAs DBR and a single $\text{In}_{(x)}\text{Ga}_{(1-x)}\text{As}$ QW embedded in GaAs. The difference lies in the thickness of the last GaAs layer between the absorber and the surrounding air.

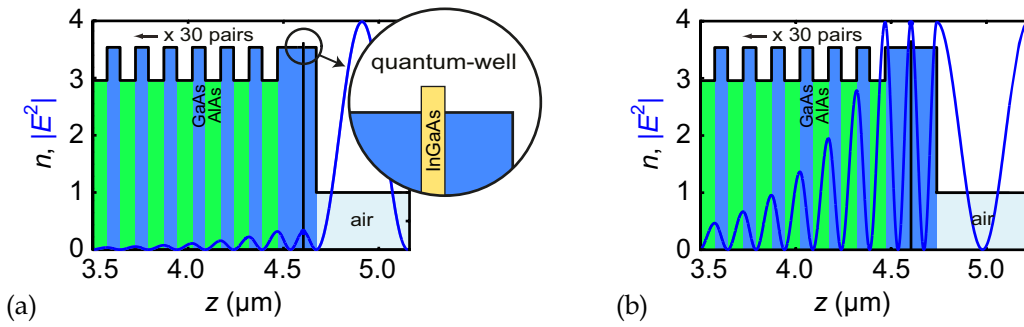


Figure 3.5 Antiresonant and resonant SESAM designs. In both cases, the SESAM consists of a 30 pair AlAs/GaAs DBR and a single $\text{In}_{(x)}\text{Ga}_{(1-x)}\text{As}$ QW embedded in GaAs. Shown in black is the refractive index profile and in dark blue the standing wave pattern of the electric field. (a) Antiresonant design. The standing wave pattern of the electric field (dark blue) exhibits a node at the surface of the SESAM. The field enhancement in the absorber has a value of around 0.32. The inset shows a magnification of the absorber. (b) Resonant design. The field enhancement in the absorber has a value of 4. This reduces the saturation fluence of the SESAM while increasing the modulation depth.

This layer determines the field enhancement in the absorber. Just like for VECSEL gain structures, we can define a field enhancement factor Γ_{abs} for the SESAM:

$$\Gamma_{\text{abs}} = |\mathcal{E}(z_{\text{abs}})|^2, \quad (3.3)$$

with z_{abs} the position of the absorber and \mathcal{E} the electric field.

Figure 3.5(a) shows an antiresonant SESAM design. The thickness of the last GaAs layer is chosen in such a way, that the electric field exhibits a minimum at the semiconductor-air interface. This results in a field enhancement $\Gamma_{\text{abs}} \approx 0.32$ in the absorber. In the case of the resonant SESAM design (Figure 3.5(b)), the electric field exhibits a maximum at the semiconductor-air interface, resulting in a value of $\Gamma_{\text{abs}} = 4$. The field enhancement directly influences important SESAM parameters like the modulation depth and the saturation fluence, which will be introduced in the following section.

3.4.3 Important SESAM parameters

Figure 3.6 shows the non-linear reflectivity curve of a resonant SESAM. For small fluences, the SESAM exhibits a low reflectivity R_{lin} and consequently high losses. This favors modelocked operation over cw operation. For higher fluences, the device begins to saturate, reducing losses. The saturation fluence F_{sat} is defined as the fluence, where the reflectivity has increased by $1/e \approx 37\%$. In a real absorber, there are always some non-saturable losses present. These may come from FCA, residual transmission through the mirror, Auger recombination, defects or scattering losses.

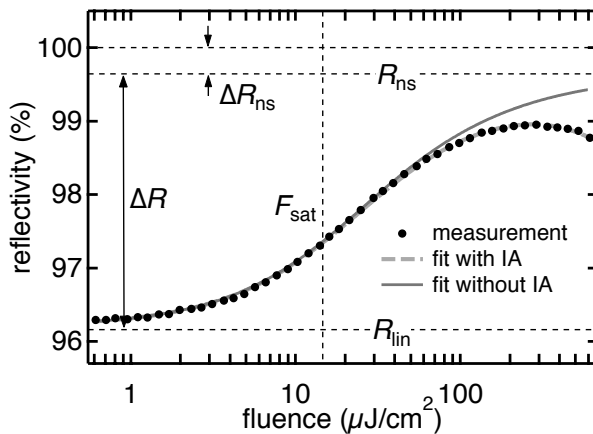


Figure 3.6 Non-linear reflectivity curve and fit function of a resonant SESAM. From the fit function relevant SESAM parameters like the saturation fluence F_{sat} or the modulation depth ΔR can be extracted. Induced absorption (IA) effects need to be included in the fit function to obtain a good fit especially at high fluences.

These are included in the non-saturable losses ΔR_{ns} and reduce the maximum obtainable reflectivity to R_{ns} . The modulation depth is given as $\Delta R = R_{\text{ns}} - R_{\text{lin}}$. At higher fluences, the effect of induced absorption (IA) needs to be taken into account. It leads to the rollover in the non-linear reflectivity curve. Different contributions to the IA effect are two-photon absorption (TPA), FCA and thermal effects [50]. Fitting the fluence-dependent reflectivity curve with a suitable fit-function allows for the extraction of the relevant SESAM parameters. The fit-function we use is based on the partial differential equation for absorber saturation in SESAMs [50]. The reflectivity model function $R(F)$ is

$$R(F) = R_{\text{ns}} \frac{\ln \left[1 + \frac{R_{\text{lin}}}{R_{\text{ns}}} \left(\exp \left(\frac{F}{F_{\text{sat}}} \right) - 1 \right) \right]}{\frac{F}{F_{\text{sat}}}} \exp \left(-\frac{F}{F_2} \right). \quad (3.4)$$

The effect of IA is taken into account by introducing the IA coefficient F_2 . It represents the fluence where the reflectivity has dropped to $1/e \approx 37\%$ because of IA. This equation holds only for a flat-top beam. A numerical correction for a Gaussian intensity distribution is performed during the fitting procedure.

3.4.4 Measurement of the non-linear SESAM reflectivity

Characterization of the fluence-dependent SESAM reflectivity requires a setup that allows for the highly precise measurement of the reflectivity over several orders of magnitude of input pulse fluences. Such a setup was demonstrated by Haiml et al. [50] and improved by Maas et al. [51]. A schematic of the improved setup is shown in Figure 3.7. The laser source for the setup is a commercially available modelocked Ti:sapphire laser (*Spectra-Physics Tsunami*) operating at a repetition rate of around 80 MHz. The pulse duration is configurable between either ≈ 100 fs or $\approx 1.4 - 1.7$ ps. The wavelength can be tuned up to 985 nm. The average output power is wavelength dependent, but at all wavelengths sufficiently high pulse energies are available to saturate the SESAMs under test.

The attenuation part of the setup is used to attenuate the laser output over up to four orders of magnitude to obtain a large measurement range. The half-wave plate is used to select a polarization of the incident laser light. The combination of one rotating polarizing beam splitters (PBS1) and one fixed PBS (PBS2) allow the large

dynamic range of the attenuation while maintaining a bandwidth of more than 100 nm. The Faraday rotator in combination with PBS3 eliminates back reflections into the laser from the measurement section.

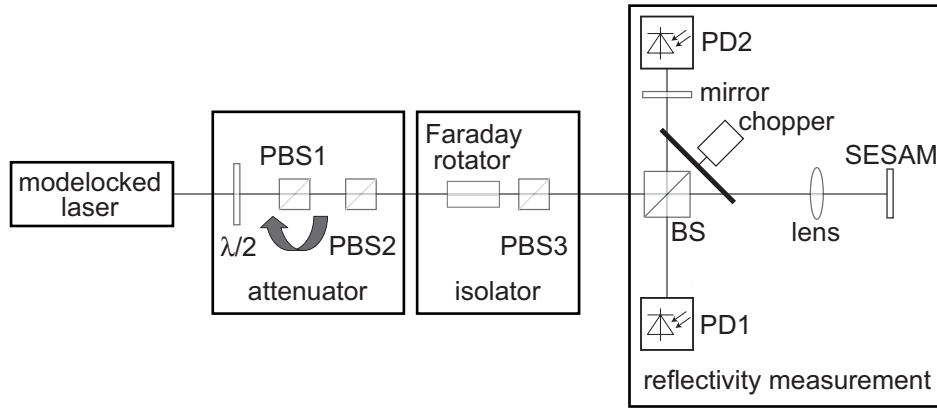


Figure 3.7 Measurement setup for the non-linear reflectivity of SESAMs: The output of a modelocked laser is first coupled into an attenuation stage. The isolator prevents back-reflections. The reflectivity value is obtained by measuring the response of both arms in the reflectivity measurement part and calculating the ratio.

The first part of the reflectivity measurement section is a non-polarizing 50:50 beam splitter (BS). One part of the split beam is reflected by a highly reflective reference mirror. The very small leakage behind the mirror is used to monitor long-term power fluctuations and to control the absolute fluence at the SESAM position using a sensitive photodiode (PD) PD2. The other part of the beam is focused onto the sample with a lens ($f = 20$ mm), resulting in a spot size ≈ 20 μm in diameter enabling high fluences on the SESAM. The reflected beams from both the reference mirror and the SESAM are combined with the BS and overlapped on PD1. PD1 is connected to an adjustable trans-impedance amplifier followed by a 24-bit analog-to-digital converter (ADC) connected to a computer.

By using a chopper wheel the beam from the mirror and from the SESAM can be separated in time and both be detected with the same photo-detector PD1. For this the chopper is positioned in such a way, that the two beam arms are chopped synchronously. From the time-separated PD-signal shown in Figure 3.8 the levels corresponding to mirror (A) and sample (B) can be extracted.

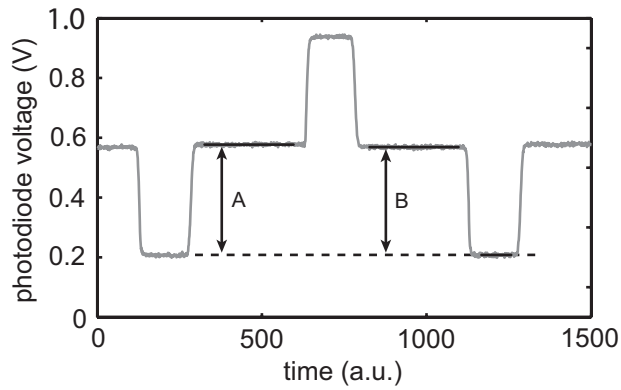


Figure 3.8 Signal analysis for a typical non-linear reflectivity measurement. The photodiode signal contains both the information of the reference mirror (A) and the sample (B).

The ratio gives the relative reflectivity. The absolute reflectivity is calibrated with a dielectric mirror with known reflectivity values, placed at the sample position. More details on the data acquisition and reflectivity calculation can be found in [51]. Advantage of this approach is a higher linearity and accuracy, in contrast to using two separate photodiodes. Furthermore, accuracy is improved by averaging over 500 periods of the chopper signal and thus reducing noise from the detector and the laser. An example of such a reflectivity measurement has been shown in Figure 3.6.

Chapter 4

Semiconductor fabrication techniques

The lasers and saturable absorbers described in this thesis are all semiconductor-based. This allows for a large degree of freedom in the design and the material composition of the devices. Furthermore, standard fabrication techniques well known from the semiconductor industry can be used and adapted for the processing of the devices. This chapter will give a brief introduction to the used semiconductor materials and their growth and characterization. Furthermore, the complete processing scheme for the EP-VECSELs will be described. Issues and solutions of the fabrication process of the gain chips will finally be discussed.

4.1 Semiconductor materials and growth

4.1.1 *Choice of the material system*

The design wavelength of our EP-VECSELs and SESAMs lies in the near infrared (NIR) at 960 nm. Figure 4.1 shows the bandgap energy and the equivalent wavelength as a function of the lattice constant for different III/V-semiconductors. At a wavelength of 960 nm, the AlAs / GaAs / InAs material system is an excellent choice, offering a very mature and established technology for growth and processing. GaAs, AlAs and the ternary compound $\text{Al}_x\text{Ga}_{(1-x)}\text{As}$ ($x \in [0,1]$) are almost lattice-matched (Table 4.1). Furthermore, they exhibit a large difference in refractive indices (contrast), enabling the efficient growth of DBRs without accumulating a significant amount of stress. For a DBR it is beneficial to use materials with a high contrast. This allows using a low number of quarter-wave layer pairs while still achieving a high reflectivity.

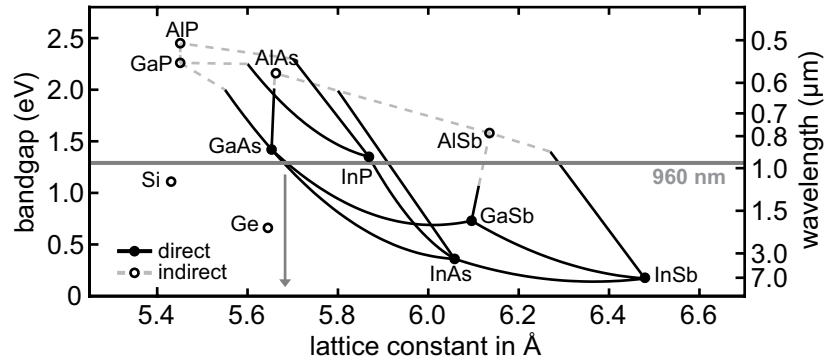


Figure 4.1 Bandgap energy and equivalent wavelength as function of the lattice constant for different III/V-semiconductors. Dots and solid lines indicate a direct bandgap, circles and dashed lines indicate an indirect bandgap.

	GaAs	AlAs	InAs
refractive index n at 1 μm	3.54	2.96	absorption
lattice constant (\AA)	5.65	5.66	6.06
bandgap at 300 K (eV)	1.42	2.15	0.36

Table 4.1: Important properties of III/V-compounds used in this thesis [52].

For the active region, another material with a lower bandgap is necessary. For the growth of the QWs in the active region, we choose the ternary $\text{In}_{(x)}\text{Ga}_{(1-x)}\text{As}$ compound ($x \in [0,1]$), with an Indium concentration of up to $x = 0.13$, depending on the exact thickness of the QWs. The lattice constant of these layers is larger than the one of GaAs/AlAs. This leads to the growth of strained layers. At a certain critical thickness or after growing several of these strained layers, they may undergo relaxation, resulting in dislocations in the lattice leading to dark-lines, where optical activity is reduced or does not take place.

4.1.2 *Semiconductor growth and calibration*

MBE growth

All semiconductor structures presented in this thesis are grown by molecular beam epitaxy (MBE). The MBE growth process is based on particle beams that are generated by heating solid material sources of highest purity. These beams are directed towards the sample position, where a high-quality substrate is positioned (semi-insulating (SI) GaAs) in our case. The different material beams then form a single crystal material. The MBE chamber is operated under ultra-high vacuum condition (10^{-10} mbar in standby and 10^{-6} mbar in growth operation) to avoid incorporation of impurities into the crystal. For high-quality, low defect-density growth, the growth temperature is typically around 600°C. For lower temperatures, the defect density gets higher, which may be wanted for example for SESAMs with a fast relaxation time. In general, a well-maintained and calibrated MBE-system can achieve excellent growth quality with very low growth errors <1%.

Our MBE system, a *Veeco / Applied EPI GEN III*, features a valved As cracker, two solid Al sources, two Ga cells, and one In cell. For n-doping, there is a Si cell available and for the p-doping a carbon tetra-bromide (CBr₄) source.

Growth rate calibration

Our structures rely on a growth error for the layer thickness of below 1%. A DBR where both GaAs and AlAs exhibit a growth error of 1% already results in a shift of the stop-band by nearly 10 nm. To obtain structures from the MBE with this high accuracy, a precise calibration of the growth rate is necessary. Since small errors in the growth rate translate to large shifts in the reflection spectrum of the devices, we compare spectral reflectivity measurements of the grown structures with their simulated reflectivity spectrum. From this comparison we can then derive the growth errors by assuming and fitting a certain error in the layer thickness of the different used materials. This procedure is shown in Figure 4.2 for a QW-SESAM with a low-GDD topcoating. Shown in black is a spectrophotometric measurement obtained using an *Agilent Cary 6000i*. The simulated spectrum is shown with a solid, gray line, the fit to the measured data in a dashed, gray line. For the fit only measurement points above 980 nm are considered, where the effect of the QW absorption is negligible.

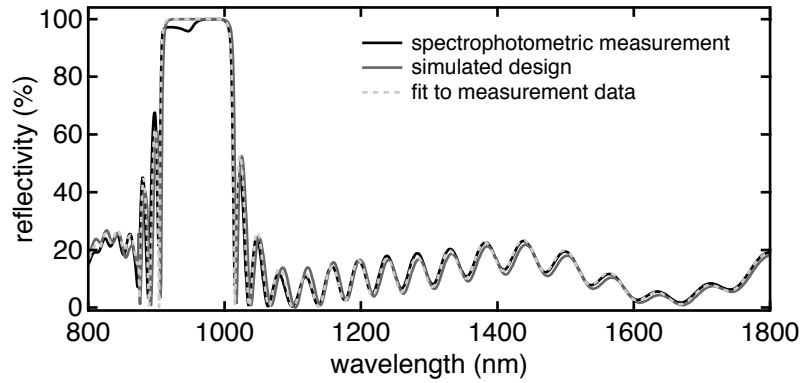


Figure 4.2 Spectrophotometric measurement, simulation and fit of the reflectivity spectrum of a QW SESAM with a low-GDD topcoating for analysis of the growth error.

Table 4.2 shows a summary of the extracted growth errors for the different materials. Values below 1% are achieved for the MBE-grown semiconductor materials. The FS layer is deposited with plasma enhanced chemical vapor deposition (PECVD). This method has a lower accuracy than the MBE-growth explaining the higher deposition error.

Material	growth error
GaAs	+ 0.4 %
AlAs	- 0.9 %
$\text{Al}_{0.2}\text{Ga}_{0.8}\text{As}$	+0.9 %
fused silica (FS)	- 5.1 %

Table 4.2: Growth error analysis of a QW-SESAM. The FS top-coating is deposited by PECVD, resulting in a higher deposition error than for the MBE-grown layers.

For the initial growth rate calibration we don't use a full structure, but a specially designed test structure. Nevertheless, the measurement and fitting procedure is the same for this test structure.

SEM and TEM imaging

Besides the calculation of the precise layer thicknesses from the reflectivity spectra, we can also measure the physical thickness of the grown layers with a scanning

electron microscope (SEM, *Zeiss ULTRA 55 / ULTRA plus*). Although the precision of the SEM is not good enough to determine absolute values, relative thicknesses of different layers can be compared. Furthermore, SEM-images help to identify major systematic errors in the layer-stack, like missing layers.

For a more precise image we can also use transmission electron microscopy (TEM). The accuracy of these images is a lot higher and allows the identification of local defects. On the other hand, sample preparation for the TEM is very time-consuming and this method is therefore only used in special cases. Figure 4.3 shows an SEM image of the entire layer stack of an EP-VECSEL. The insets show TEM images with a much higher resolution.

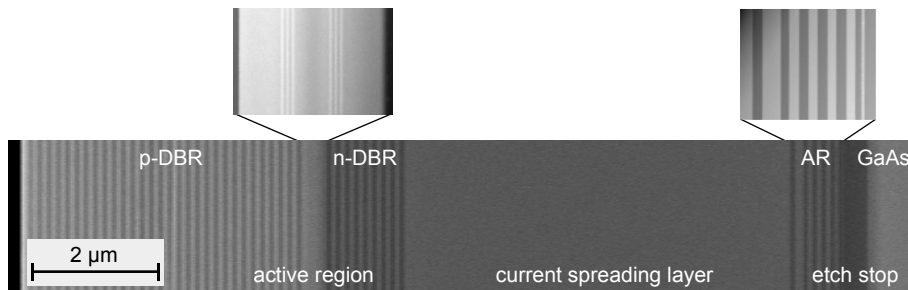


Figure 4.3 SEM image of an EP-VECSEL, grown in reverse order for substrate removal on a GaAs wafer. The insets show TEM images, which provide a much higher resolution.

Calibration of the QW-photoluminescence

Aside from the precise layer thickness, we also need to calibrate the emission wavelength of the $\text{In}_x\text{Ga}_{1-x}\text{As}$ QWs used in the active region of the EP-VECSELs and in the absorber section of the SESAMs. The peak wavelength of the QW-PL is measured with a PL mapper (*Accent RPM2000*) at room temperature and the indium content and the QW-thickness need to be corrected if applicable.

Doping calibration

For the electrical pumping of our VECSELs we need to dope the structures. For a given growth rate, we therefore also need to calibrate the doping concentration for the different materials and dopants. For the measurements of the doping concentration, we use two different systems: a Hall effect measurement system (*Accent HL5500PC*) and an electro-chemical C-V profiling system (*Dage CVP 21*).

Measurement and comparison of doping concentrations with both systems gives a sufficiently high accuracy for our structures.

4.2 Processing

In this section, a short overview and description of the used processes for the laser fabrication will be given first. Then the complete processing scheme of our EP-VECSELs will be described, also addressing encountered issues and simplifications in the complicated process flow.

4.2.1 *Fabrication methods*

Cleaving of III/V semiconductors

Our semiconductor devices are all grown on 3" GaAs substrates. Since we usually only want to process a part of the wafer, we need to prepare the individual samples. III/V semiconductors exhibit natural cleavage planes, along which they can be split. To achieve this, we use a diamond wafer scribe to make a scribe at a defined position. Starting from this scribe, we can then split the wafer along one of the cleavage planes, giving a very smooth surface for the cleaved samples.

Cleaning steps

Throughout the processing scheme we use standard cleaning steps whenever applicable to ensure the least possible contamination with particles or unwanted residues. Some of the cleaning steps and chemicals are:

- Acetone, isopropanol (IPA) and de-ionized (DI) water for removing particles and photoresist
- O₂-plasma asher (*Technics Plasma 100-E*) for removing organic residues and remaining photoresists
- Trichloroethylene (TCE) for removing vacuum grease after inductively coupled plasma (ICP)-etching and wax after lapping
- Hydrochloric acid (HCl) for deoxidizing GaAs before depositing metals to improve the electrical contact

Photolithography

Photolithography is a well-established technology to transfer patterns or geometric structures from a mask to a sample. We use a two-step process, where we first transfer the pattern from the mask to the photoresist on the sample and then transfer the pattern to a SiN_x-hardmask using RIE-etching. Typical elements of a photolithography process are the following:

- **Cleaning of the sample:** We always start our process by rinsing the samples in DI water. This removes particles from the surface of the samples.
- **Spinning of photoresist on the sample:** Using a spin-coater, we apply a thin, homogeneous film of photoresist on the sample. The exact thickness depends on the resist and the spinning speed and time. An adhesion-promoter like hexamethyldisilazane (HMDS) may be used before the spinning to ensure adhesion of the thin resist layer on the sample. For the spinning process we use a *Sawatec SM 180 BM* spin module.
- **Softbaking:** To improve stability of the resist, the sample is heated on a hotplate, typically to temperatures around 100°C.
- **Exposure:** The desired pattern is transferred from the mask to the resist using a mask aligner (*Süss MicroTec MA6*). First sample and mask are aligned using especially designed alignment markers, then the resist is exposed using an ultra-violet (UV) lamp in our case. Depending on the type of resist, either the exposed resist is removed during subsequent development (positive resist) or the unexposed resist is removed (negative resist), leaving behind the pattern of the mask (or the negative pattern). In our processing scheme we use both kinds of resists.
- **Development:** The exposed/unexposed resist is removed using a specific developer for the chosen photoresist. The desired pattern is now transferred to the resist on the sample. More details on the underlying chemical processes during exposure and development can be found in [53].
- **Hardbaking:** For certain resists and recipes it is beneficial to bake the sample again after development. This further increases the stability of the resist pattern.

- **Etching:** The sample can now be etched in the RIE to transfer the pattern to the SiN_x -hardmask. Using this two-step process with a hardmask ensures a higher selectivity during the subsequent ICP-etching.
- **Resist removal:** After successful etching of the hardmask, the remaining photoresist can now be removed using acetone, IPA and O_2 -plasma ashing.

Plasma machines

For the processing of the EP-VECSEL gain chips we rely on various plasma machines for the deposition or etching of layers. They are all based on the following operation principle: gaseous chemicals are brought together in a plasma reactor with exactly controlled fluxes. At a controlled pressure and temperature, a plasma is ignited and supplied with energy using a radio frequency (RF) electric field inside the reactor. The plasma significantly accelerates physical and chemical processes inside the chamber. The used plasma machines are the following:

- **Plasma-enhanced chemical vapor deposition (PECVD):** For the deposition of thin dielectric films onto semiconductor samples we use an *Oxford Instruments PECVD 80+*. The materials we typically deposit are silicon nitride (SiN_x) and silicon oxide (SiO_x , also referred to as fused silica (FS)). Both materials are used for optical top-coatings of SESAMs, SiN_x is additionally used as a hard-mask for our photolithography processes. Both deposition recipes are based on a chemical reaction of silane (SiH_4) with ammonia (NH_3) for SiN_x and with nitrous oxide (N_2O) for SiO_x , respectively. With this machine we can deposit films of precise thickness (relative errors of around 5%) with layer thicknesses up to a few μm . Typical deposition rates for SiN_x are around 19 nm/min and around 40 nm/min for SiO_x .
- **Reactive ion etching (RIE):** The process of reactive ion etching (dry etching) is used in our processing scheme to transfer the mask pattern from the photolithography onto the SiN_x -mask. This requires etching the SiN_x -mask. Principally, two types of etching processes can be achieved inside the plasma chamber. If chemically inert gases like argon (Ar) or nitrogen (N_2) are used, they are first ionized in the plasma and the generated electrons charge the chamber. As a result, the ungrounded sample tray builds up a negative charge leading to a voltage in the order of a few 100 V. This accelerates the positively

charged ions towards the sample, bombarding the surface and leading to a so-called physical etching. The etch profile is typically v-shaped with no under-etch. On the other hand, if the recipe is fluorine (F)-based, the etching process is driven mainly by chemical reactions of radicals and consequently the process is referred to as chemical etching. This results in an isotropic, round etch-shape with a strong under-etch. Combining physical and chemical etching can result in smooth, straight sidewalls, if the recipe is well-optimized. We use a fluorine-based recipe with CHF_3 and O_2 , resulting in a chemical, isotropic etch. The machine we use for this is an *Oxford Instruments RIE 80+*. Etch rates of around 90 nm/min for SiN_x are typically obtained.

- **Inductively coupled plasma (ICP) etching:** ICP-etching is in principle similar to RIE-etching. The difference is an additional high power RF generator, that enables significantly higher etch rates than the RIE. We use it to etch GaAs and AlAs with etch rates of up to 2.5 $\mu\text{m}/\text{min}$. The recipe is based on chlorine (Cl_2) and Ar, resulting in a combination of physical (Ar) and chemical (Cl_2) etching. The recipe is optimized to obtain straight sidewalls. The machine we use is an *Oxford Instruments ICP 180*.

Wafer bonding

Table 4.3 shows a list of different semiconductor and heatsink materials and their thermal conductivity. The GaAs substrate exhibits a low thermal conductivity and is therefore removed and replaced by a heatsink with higher thermal conductivity. To remove the GaAs substrate from our devices, we first need to bond them to a heatsink to maintain the mechanical stability of the sample. Although copper (Cu) exhibits a higher thermal conductivity, we use CuW as a heatsink material. It has the same coefficient of thermal expansion (CTE) as GaAs, reducing stress during rapid thermal annealing. Diamond-based materials like copper-diamond are also CTE-matched to GaAs, but are more expensive and are consequently only used if a design has been successfully tested on CuW. For the bonding process, we use a tin/gold (Sn/Au) alloy and an *AML AWB* wafer bonder.

material	thermal conductivity κ (W·K ⁻¹ ·m ⁻¹)
GaAs	45
AlAs	91
Al _{0.85} Ga _{0.15} As	14
copper-tungsten* (CuW)	180 - 220
copper (Cu)	400
copper-diamond* [54]	550
silver-diamond* [55]	650
CVD diamond	1000 - 1800

Table 4.3: Thermal conductivity of different materials relevant to the heatsinking of EP-VECSEL gain structures. CTE: coefficient of thermal expansion; CVD: chemical vapor deposition; *: CTE matched to GaAs.

Lapping

For time-efficient removal of the substrate from the devices, we first use a lapper system to mechanically thin the substrate to a given thickness. The used system is a *Logitech PM5 Autolap*.

Wet-etching

For certain etching steps, we rely on wet-chemical etching, for example if we want to completely remove the GaAs substrate. Etching in the ICP does not provide a good enough selectivity to differentiate between the structure and the substrate. We use a two-step process with an Al_{0.85}Ga_{0.15}As etch-stop layer to remove the remaining GaAs substrate [56]:

- Citric acid (C₆H₈O₇) / hydrogen peroxide (H₂O₂): This solution etches the GaAs, but has a high selectivity towards the Al_{0.85}Ga_{0.15}As etch-stop layer, if the pH value is chosen correctly.

- Hydrofluoric (HF) acid: The etch-stop layer is removed using HF acid. Al exhibits a higher reduction potential than Ga. Therefore only Al is oxidized in HF acid and becomes soluble, resulting in the selectivity towards GaAs. HF acid can also be used to etch SiN_x or SiO_x selectively towards GaAs.

Evaporation of metals

To create ohmic contacts at the semiconductor-metal interface of the electrical contacts, two different optimized layer-stacks are evaporated onto the device. On the p-doped side, we use titanium/platinum/gold (Ti/Pt/Au), on the n-doped side we use Ge/Au/Ge/Au/Ni/Au (Ge: germanium, Ni: nickel). All of these layers are evaporated using a *Plassys MEB550SL* system.

Rapid thermal annealing (RTA)

Using a highly doped contact layer and an optimized metallization layer stack is not sufficient to obtain ohmic contacts with low electrical resistance for our devices. We need to additionally anneal the EP-VECSEL gain chips in an RTA oven. We use a *J.I.P. Elec JetFirst 100* system. Figure 4.4 shows the effect of annealing on the IV-characteristics of an EP-VECSEL gain chip. The device was measured before annealing (shown in gray) and after annealing (shown in black) in the RTA for 90 s at 400°C. Without annealing, the turn-on voltage and the series resistance of the device is increased, leading to higher ohmic losses. This leads to a thermal rollover already at low injection currents, limiting the achievable output power. The reason for this lies in the Schottky-characteristic of the semiconductor-metal interface if the doping levels, metallization and annealing parameters are not properly chosen.

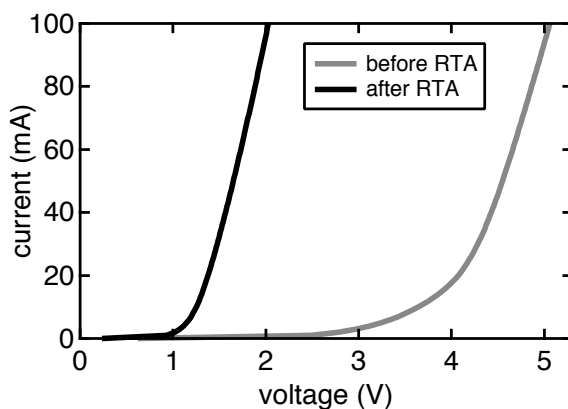


Figure 4.4 Effect of annealing on the IV-curve of an EP-VECSEL gain chip. The device was measured before (gray line) and after annealing (black line) in the RTA for 90 s at 400°C.

4.2.2 *EP-VECSEL process flow*

In this section the different processing steps starting from the MBE-grown wafer to the finished EP-VECSEL gain chip are briefly described.

Selection and cleaving of the samples

First, a 5-mm-wide bar is cleaved from one of the four quarters of the whole wafer. The reflectivity spectra over this bar are measured and the area with the smallest growth error identified. Then 11.5 mm x 12 mm samples are cleaved from this area of the wafer from which the EP-VECSELs will be fabricated.

Definition of the alignment markers

Since we process the semiconductor material from the topside and after substrate removal also from the bottom, we need to make sure that top and bottom contacts are aligned with respect to each other. This is achieved by etching alignment markers through the whole layer-stack. They are defined by photolithography and dry-etched with the ICP. The etch depth needs to be at least 13.5 μm to go through the whole layer-stack and requires a recipe optimized for straight sidewalls.

Bottom contact definition and metallization

Next, a 350-nm thick SiN_x layer is deposited with the PECVD as an electrical isolation. The bottom disc contacts are defined in this layer using photolithography and dry-etching with the RIE. Then the whole chip is metallized with Ti/Pt/Au using the evaporator to form the bottom contacts.

Wafer bonding

In the following step, the samples are flipped and bonded to the CuW heatsink at a temperature of 350°C and a pressure of 495 N/cm² (force: 683 N) with a Sn/Au alloy using the wafer bonder. The CuW-wafers are 300 μm thick and have a diameter of 25 mm.

Substrate removal

The GaAs substrate is removed in two steps: First, it is thinned down mechanically from 600 μm to around 60 μm using a lapper system. We use an Al_2O_3 abrasive with 3 μm grain size. The rest of the substrate is removed by wet-chemical etching using a citric acid/ H_2O_2 solution as described in Section 4.2. The $\text{Al}_{0.85}\text{Ga}_{0.15}\text{As}$ etch-stop

layer is removed using HF-acid and ensures an optical-grade surface roughness. The alignment markers from the topside are now visible.

AR-definition

Next, the AR-section is defined by photolithography and dry-etching down to the n-contact layer using the ICP.

Laser separation

To electrically and physically isolate neighboring EP-VECSELs on the chip, they are separated from each other with an ICP dry-etching step using a SiN_x hard mask, where deep trenches down to the bottom metallization are formed. Afterwards, the whole chip is again covered with SiN_x to protect the sidewalls against oxidation.

Top contact openings

Just like the bottom contact openings, the top-contact openings are defined in a PECVD-deposited SiN_x layer using photolithography and RIE-etching. Before that, the trenches from the previous ICP-etch need to be filled with photoresist (planarized) to ensure sufficient homogeneity of the resist of the top-contact opening photolithography.

Top contact metallization

To prepare the sample for the n-metallization, all parts of the chip, which are not meant to be metallized, are covered with a negative photoresist. A second planarization step before spinning the negative resist is optional, but improves the homogeneity of the photolithography. The chip is now metallized with a layer-stack of Ge/Au/Ge/Au/Ni/Au.

Lift-off and annealing

After metallizing the sample, a lift-off process in 50°C warm acetone removes the metal from all unwanted surfaces. The chip is then annealed in the RTA at 400°C for 90 s to form ohmic contacts between the metallization and the semiconductor material. Afterwards, the EP-VECSEL gain chip is ready for testing. Figure 4.5 shows an SEM image of a single, completely processed device on an EP-VECSEL gain chip and reveals the real device dimensions.

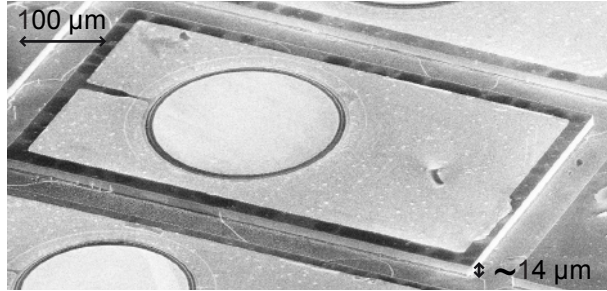


Figure 4.5 SEM image of a single, completely processed device on the EP-VECSEL gain chip.

4.2.3 Challenges in the realization of EP-VECSELs

The realization of an EP-VECSEL provides many challenges due to the critical growth and complicated processing scheme:

- The epitaxial growth consists of many layers with different material composition and the overall structure is also considerably thick (around $13.5\ \mu\text{m}$). Not only the layer thicknesses, but also the doping values have to exhibit small errors to achieve good performance. The resonant gain structure increases the demands on the growth accuracy further.
- The structure is grown in reverse order. Therefore, reflectivity measurements of the device contain limited information, since the high-reflective p-DBR is on top of the structure. Thus, characterization of the growth error of the entire device is not possible. Since the AR-coating is undoped, the electrical properties of the chip also cannot be characterized without etching away parts of the layer-stack.
- The processing scheme is complicated and contains many steps. Furthermore, the devices are processed in a multi-user cleanroom, where a frequent recalibration of the processes is necessary.

To reduce the processing time and make the optimization of the EP-VECSELs more time-efficient, the fabrication scheme of the EP-VECSELs was slightly optimized and simplified during this thesis. The two most important changes are:

- **The AR-definition has been eliminated.** This saves a significant amount of time, since a photolithography step and two dry-etching steps can be skipped. On the other hand, this requires doping the AR-coating to make it conductive

for electrical current, but also opens the possibility to test the devices electrically without completing the whole processing scheme. Figure 4.6(a) shows the influence of the AR-definition on the IV-curve of an EP-VECSEL. Two electrical test samples were fabricated; on one of them the AR-coating was etched away (gray line). The AR-coating was n-doped at a doping concentration of $2 \cdot 10^{18} \text{ cm}^{-3}$. As expected, the series resistance is higher for the sample with AR-coating, but the increase can be tolerated to accelerate the fabrication process.

- **Chromium (Cr) has been added to the p-metallization as a diffusion barrier.** Under certain circumstances, the Sn in the Sn/Au-solder, used to bond the EP-VECSEL gain chip to the CuW-heatsink, may diffuse towards the Ti/Pt/Au p-metallization.

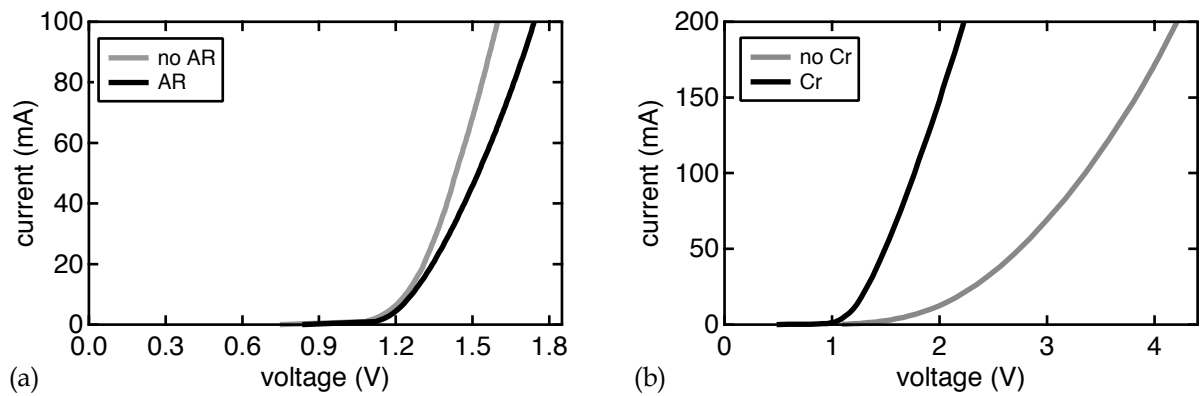


Figure 4.6 (a) Effect of the AR-definition on the IV-curve of an EP-VECSEL gain chip. On one of the electrical test samples (gray line) the AR-coating is completely etched away, on the other test sample of the same size (black line) not. (b) IV-curve of an EP-VECSEL (110 μm BCD) with and without a chromium layer as diffusion barrier in the Sn/Au solder.

Although Pt also acts as a diffusion barrier, the effect may be insufficient in some cases. Consequently, we have included an additional Cr-layer in the p-metallization to enhance the diffusion-barrier effect [57]. The complete layer-stack now consists of Ti/Pt/Au followed by Ti/Cr/Au. Figure 4.6(b) shows IV-curves of two EP-VECSELs of the same BCD of 110 μm . On one of the samples we used Cr as an additional diffusion layer (black line), on the other not. The sample without the Cr (gray line) has a much higher voltage drop at the same current and the turn-on behavior of the diode is not visible. This is due to the Schottky-behavior of the semiconductor/metal

interface, similar to what we have already seen in Figure 4.4. The effect is increased in case the Au/Sn solder comes too close to the semiconductor/metal interface. Again, this leads to a high series resistance of the device, increasing ohmic losses and strongly reducing the achievable output power of the device due to a thermal rollover already at low injection currents.

Chapter 5

First experimental results

Based on the design described in Chapter 2, we fabricated an EP-VECSEL gain chip with 61 geometrically different lasers. In this chapter, the experimental characterization of these lasers is presented. First, the test setup and the electrical characteristics of the devices are described. In the second section, cw measurements are presented and the performance limitations of this design are discussed. The results presented in this chapter have been partly published in [58].

Figure 5.1 shows images of the fabricated chip. Each of the four sections visible in Figure 5.1(a) contains 61 lasers with different BCDs and top contact openings. The structure height is around $13.5\text{ }\mu\text{m}$.

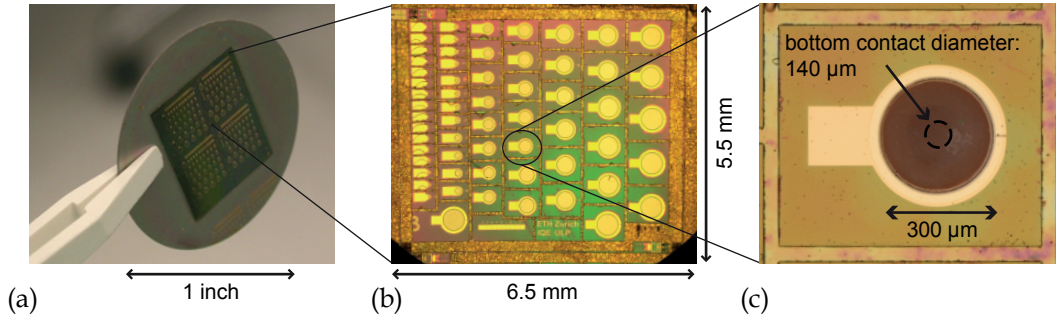


Figure 5.1 Images of the fabricated EP-VECSEL gain chip. (a) One-inch CuW wafer with 4×61 geometrically different lasers. (b) Zoom on one section. The 61 different lasers have different BCDs and top contact openings. (c) Zoom on a single laser with a BCD of $140\text{ }\mu\text{m}$ and a top contact opening of $300\text{ }\mu\text{m}$. The device height is around $13.5\text{ }\mu\text{m}$.

5.1 Test setup

The test setup for the EP-VECSEL gain chip is shown in Figure 5.2(a). The CuW heatsink with the different devices is mounted onto a copper heatsink, which is temperature-stabilized with a thermoelectric cooler (TEC) and a temperature controller. The individual lasers can be contacted with the help of a microscope (not shown) using a probe needle. The standard test cavity consists of a curved output coupler with a radius of curvature (ROC) of 25 mm, which was placed at a distance of 24.5 mm from the gain chip (Figure 5.2(b)). The output power was detected with a power meter and the voltage was measured using the current driver.

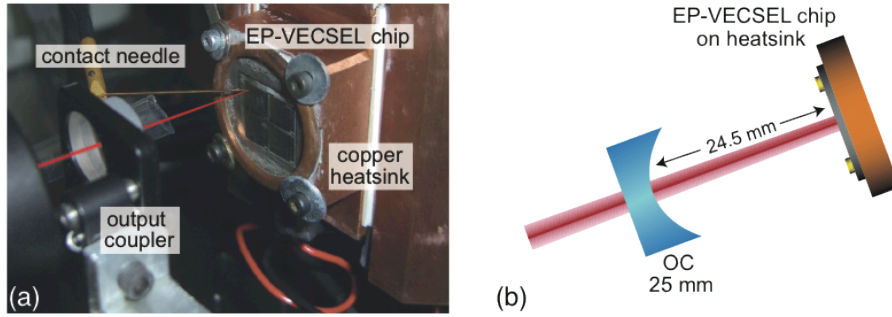


Figure 5.2 Straight cavity for the cw characterization. (a) Image of the cavity with the EP-VECSEL gain chip mounted on the copper heatsink, the curved OC and a probe needle for the electrical contact. (b) Cavity schematic. The OC had a ROC of 25 mm and was placed at a distance of around 24.5 mm from the EP-VECSEL gain chip.

5.2 Electrical characterization

5.2.1 Threshold behavior and resistance

In a first step, the threshold behavior and the electrical resistance of the devices were evaluated. Figure 5.3(a) shows the lasing threshold current I_{th} as a function of the BCD. A linear increase with the BCD can be observed. In Figure 5.3(b), the differential resistance at threshold ∂R_{th} is plotted for the different device sizes. We chose this parameter because it takes the device geometry into account. ∂R_{th} shows a hyperbolic behavior. This can be explained with the following. In EP-VECSELs with a bottom p-DBR, the hole current is confined to the bottom disc contact size. Therefore, the device resistance scales inversely with the bottom contact radius [24].

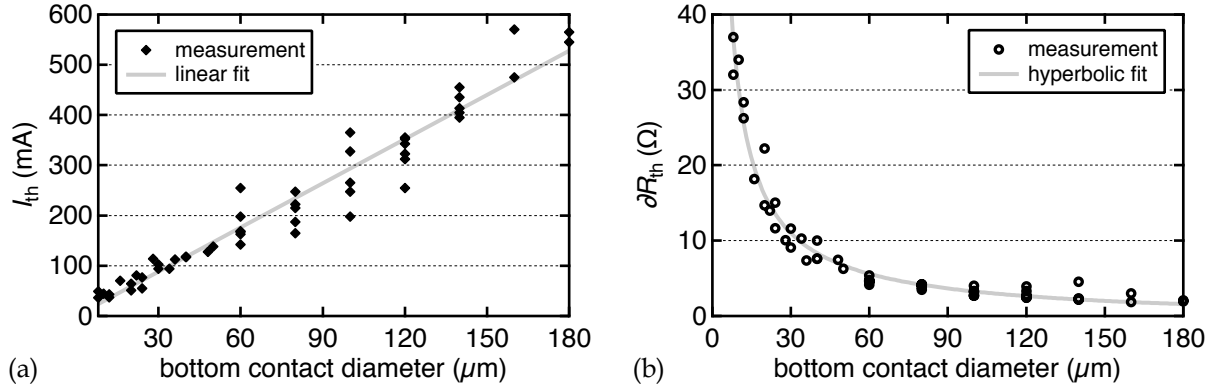


Figure 5.3 (a) Lasing threshold current and (b) differential resistance at lasing threshold as a function of the BCD. The threshold current increases linearly with the BCD, the differential resistance at threshold shows a hyperbolic behavior with decreasing values for larger devices.

5.2.2 Current confinement

A major challenge for EP-VECSELs is a confined, Gaussian-like current injection profile. This is essential for achieving transversal TEM_{00} -mode operation necessary for stable passive modelocking. We determined the current injection profile using spatially resolved electroluminescence (EL) measurements, where the EL is imaged onto a charge-coupled device (CCD) camera. Figure 5.4 shows the EL-profiles of EP-VECSELs with different BCD. Devices up to a BCD of $100\ \mu\text{m}$ show a confined, Gaussian-like current injection profile. For larger devices, the EL-profiles exhibit a dip in the center, increasing with the device size.

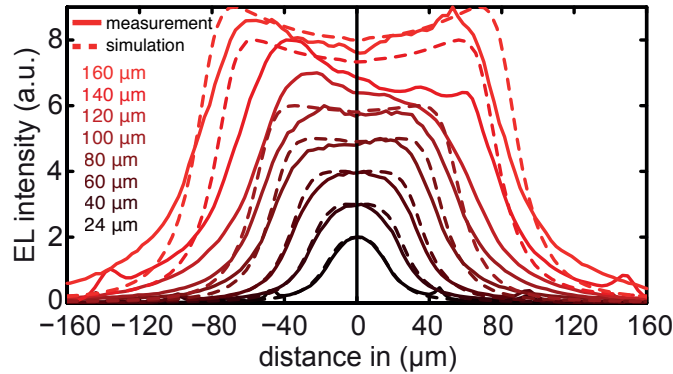


Figure 5.4 Measured (solid lines) and simulated (dashed lines) electroluminescence (EL) profiles of EP-VECSEL gain chips with different BCD. Devices up to a BCD of $100\ \mu\text{m}$ show a homogeneous current injection profile.

The measurements (solid lines) were also compared to our simulation model (dashed lines). For small devices an excellent agreement can be found between the measurements and the simulation results.

5.3 Continuous-wave characterization

As a next step, the devices on the EP-VECSEL gain chip were characterized with regards to their cw characteristics. Powerscaling with device size, spectral properties and the beam quality were determined.

5.3.1 Output power and powerscaling

Figure 5.5 shows a light-current-voltage (LIV)-curve of the largest EP-VECSEL with a BCD of $180\text{ }\mu\text{m}$. Up to 120 mW are obtained in cw multi-mode operation at the thermal rollover. The heatsink temperature was stabilized to 3°C and the OC transmission was 10%.

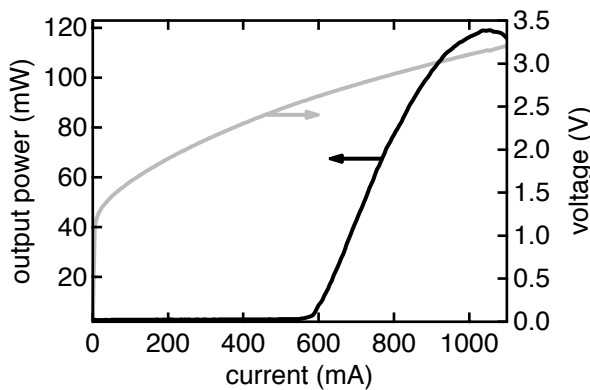


Figure 5.5 LIV-curve of the largest laser with a BCD of $180\text{ }\mu\text{m}$. Up to 120 mW of multi-mode cw output power are achieved. The heatsink temperature was 3°C and the OC transmission 10%.

The transmission of the OC was optimized for the highest achievable output power. The optimum was found to be at 10% transmission. Figure 5.6 shows the influence of the OC transmission on the output power of the $180\text{-}\mu\text{m}$ -BCD device. The heatsink temperature was stabilized at 20°C for these measurements. The OC transmission was varied between 1.5% and 30%. Even for a transmission value of 30%, lasing operation was still achieved at reduced output power.

Compared to an OP-VECSEL, these values seem very high, were typical values are in the few-percent range. On the other hand, the EP-VECSEL consists of two coupled cavities, one between the p-DBR and the n-DBR and the other the external cavity. Our initial design with 11 AlAs/GaAs n-DBR pairs had an n-DBR reflectivity of nearly 93%.

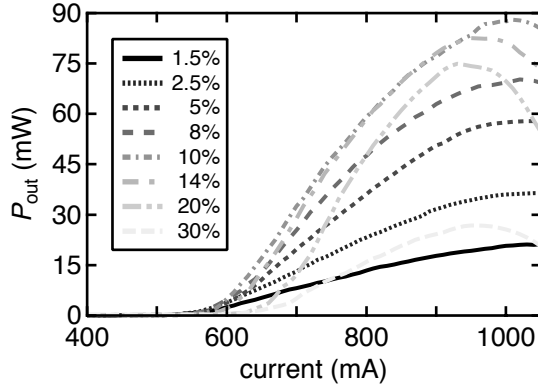


Figure 5.6 Effect of the OC transmission on the output power of a 180- μm BCD EP-VECSEL. The ROC was 25 mm and the heatsink temperature 20°C.

This means that only 7% of the power is transmitted to the external cavity. From these 7%, a certain fraction is then extracted by the OC, requiring much higher transmission values to achieve the same effective transmission. As an example, an effective transmission of 1% can be achieved with an OC transmission of around 14% if a simple multiplication of the transmission values is considered. This estimation leads to values close to the real OC transmission, but needs to be seen as a simplification, since the dynamics of the coupled cavities are more complex.

To investigate the influence of the BCD on the output power, LIV-curves were recorded for the other devices on the chip with different BCDs. In each case, the maximum achievable output power was determined. Figure 5.7(a) shows the output power as a function of the BCD. A linear increase with the BCD can be observed.

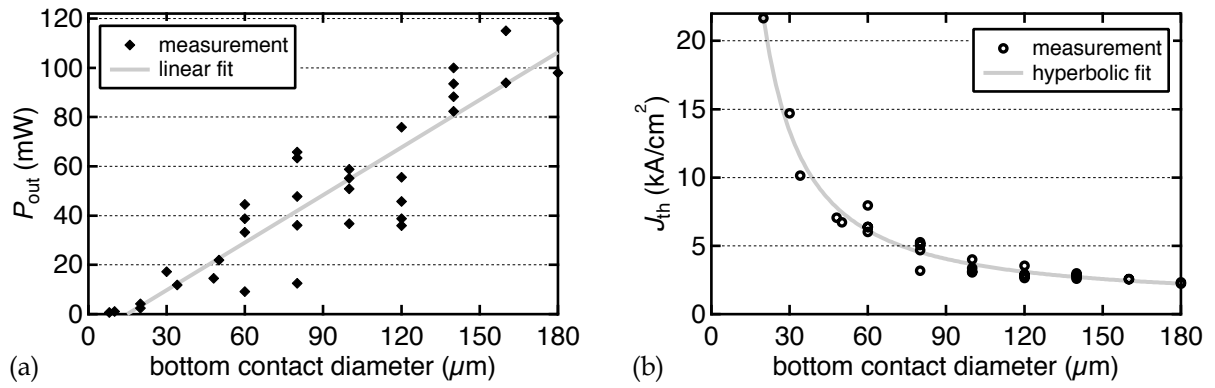


Figure 5.7 (a) Output power and (b) threshold current density as a function of the BCD. The output power increases linearly with the BCD, whereas the threshold current density shows a hyperbolic behavior.

In case of ideal powerscaling, one would expect an increase of the power with the area of the devices. This gives an indication of thermal issues for larger devices. Furthermore, the threshold current density as a function of the BCD shown in Figure 5.7(b) shows a hyperbolic behavior towards larger devices, again indicating thermal problems. The powerscaling limitations will be further discussed in the following section after analyzing the spectral properties of the devices.

5.3.2 Spectral properties of the EP-VECSELs

Figure 5.8(a) shows a typical optical multi-mode cw spectrum for a 100- μm -BCD EP-VECSEL recorded at an injection current of 390 mA and a heatsink temperature of 20°C. In Figure 5.8(b) the shift of the optical spectrum for the same device is plotted as a function of the injection current. A redshift and a spectral broadening can be observed for increasing currents. The redshift can be explained by an increase of the internal device temperature at higher currents due to resistive losses. Both the cavity mode and the gain peak exhibit a temperature-dependent shift of 0.07 nm/K and 0.3 nm/K [16], respectively, leading to the redshift of the emission wavelength at high currents. This relation also provides an excellent method to extract the internal device temperature using the temperature-dependent wavelength-shift of the optical spectrum.

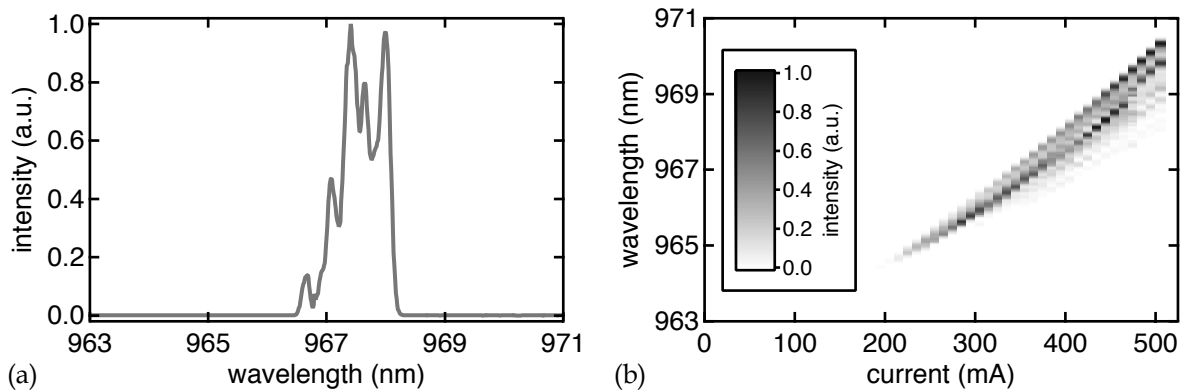


Figure 5.8 (a) Optical multi-mode cw spectrum for a 100- μm -BCD EP-VECSEL recorded at an injection current of 390 mA and a heatsink temperature of 20°C and (b) wavelength shift of the optical spectrum above lasing threshold as a function of the injection current. For each measured value of the current, a spectrum like the one in Figure 5.8(a) is recorded. A redshift and broadening of the spectrum is visible for increasing currents.

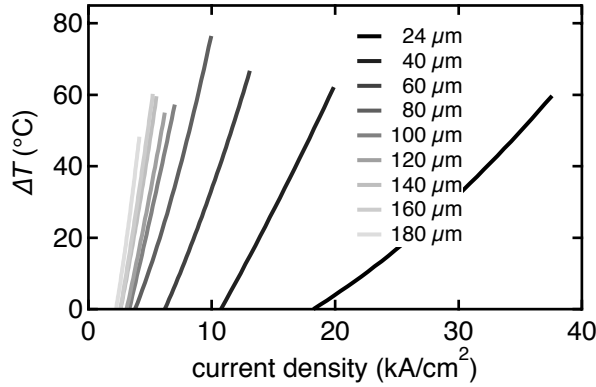


Figure 5.9 Estimated temperature shift as a function of the current density for devices with different BCD. All devices are measured until the thermal rollover occurs. Larger devices heat up more for lower current densities.

To gain better insight into the limitations of powerscaling our devices, we used this method to extract the temperature increase as a function of the current density for devices with different BCDs. For each device size, the shift of the spectrum was measured as a function of the current density up to the thermal rollover point. With the cavity resonance shifting at 0.07 nm/K, the temperature shift can then be determined. The results are plotted in Figure 5.9. Larger devices exhibit the thermal rollover at lower current densities. In case of ideal powerscaling, the temperature increase should be independent of the device size. As this is clearly not the case, an ideal one-dimensional heat flow is not given for our devices. Better performance can be expected by applying the following changes:

- Optimization of the electrical resistance of the EP-VECSEL reduces heating due to ohmic losses and shifts the thermal rollover to higher current densities.
- Choosing a larger device geometry while maintaining the size of the electrical contacts should increase the heat transfer area and therefore reduce the internal device temperature.
- A heatsink with a higher thermal conductivity should further help to reduce the internal temperature. Composite diamond materials like copper-diamond are promising candidates (see Chapter 4).

5.3.3 Beam quality of the EP-VECSELs

Excellent beam quality is an important prerequisite for achieving stable modelocked operation of an EP-VECSEL. In Section 5.2.2, measurements of the current injection profile have already been presented, revealing a Gaussian-like injection profile for devices below 100 μm BCD that should support transversal TEM_{00} -mode operation. To characterize the beam quality of our EP-VECSELs, we measured the M^2 -value of the laser beam for different BCD-devices. Table 5.1 shows a summary of the measurements. In all cases a straight cavity was used with an OC with a ROC of 25 mm and a transmission of 10%. The heatsink temperature was kept at 3°C.

device size (BCD)	cavity configuration	output power	M^2 - value
180 μm	straight cavity	120 mW	> 20
80 μm	straight cavity	30 mW	3.6
80 μm	straight cavity with intra-cavity aperture	5 mW	1.0

Table 5.1: Beam quality measurements of our EP-VECSELs with different BCDs in different cavity configurations.

For the maximum output power of 120 mW obtained from the 180- μm -BCD device, the laser was operating in the multi-mode regime with an $M^2 > 20$. Using a smaller device with a BCD of 80 μm and optimizing for the highest output power with the best beam quality (lowest M^2 -value), 30 mW with an $M^2 = 3.6$ were achieved. Introducing an intra-cavity aperture, an $M^2 = 1.0$ was obtained, but at a significantly reduced output power level of 5 mW.

Despite the Gaussian-like current injection profile, the achievable beam quality from our EP-VECSELs was insufficient for passive modelocking experiments. This can be attributed to the high reflectivity of the n-DBR, as it will be discussed and experimentally verified in the following chapter.

Chapter 6

Beam quality and gain

characterization of EP-VECSELs

In the previous chapter we have seen that a high intermediate n-DBR reflectivity has a negative effect on the beam quality of EP-VECSELs. To study and quantify this effect better, we characterized the beam quality as a function of the n-DBR reflectivity. For this purpose, three EP-VECSELs with a different number of n-DBR pairs were available from our collaborator *Philips U-L-M Photonics*. These EP-VECSELs also offer the opportunity to determine relevant gain properties like the gain bandwidth and the gain saturation behavior as a function of the resonance. A good knowledge of these parameters is important for passive modelocking experiments and for modeling of these devices.

At the beginning of this chapter, the design of the *Philips U-L-M Photonics* EP-VECSELs will be described. Especially the design differences to our EP-VECSELs will be highlighted. Then an electrical and cw multi-mode characterization will be presented. Subsequently, the beam quality of these devices will be characterized. In the following section, spectral gain measurements of these EP-VECSELs will be presented, followed by gain saturation measurements. Finally, passive modelocking experiments using the most suitable device will be described. Parts of this chapter have been published in [58, 59].

6.1 Design of the characterized devices

Like our devices, the *Philips U-L-M Photonics* EP-VECSELs are based on the GaAs/ $\text{Al}_{(x)}\text{Ga}_{(1-x)}\text{As}$ material system. The highly reflective p-DBR and the intermediate n-DBR consist of alternating quarter-wave layers of $\text{Al}_{0.12}\text{Ga}_{0.88}\text{As}$ and $\text{Al}_{0.9}\text{Ga}_{0.1}\text{As}$. The active region consists of three $\text{In}_{(x)}\text{Ga}_{(1-x)}\text{As}$ QWs embedded in GaAs, positioned in one antinode of the standing wave pattern of the electric field. The peak PL wavelength of the QWs is detuned to shorter wavelengths by 12 nm from the design wavelength of 980 nm. An oxide aperture is used to confine the current in the active region to 100 μm in diameter. The BDC has a diameter of 140 μm , the top ring contact has an opening of 200 μm . The three devices exhibit 9, 11 and 13 intermediate n-DBR pairs, resulting in a field enhancement of 12, 22 and 35, respectively. The CSL is realized by mechanically thinning down the n-doped substrate. The doping level concentration of the substrates is between $0.5 - 1.0 \cdot 10^{18} \text{ cm}^{-3}$. The resulting thickness of the CSL for the three devices is 150 μm (13 pairs), 56 μm (11 pairs) and 60 μm (9 pairs). Due to the thicker CSL these EP-VECSELs have higher optical losses due to FCA than our devices. The difference in thickness between the three devices is due to a process optimization in the fabrication scheme. Finally, the structures are AR-coated with a single quarter-wave layer of SiN_x . The EP-VECSELs are mounted with the p-side down on an aluminum-nitride (AlN) heatsink tile, which is then soldered to a TO-can mount for easy electrical testing. Figure 6.1 shows an image of the three characterized *Philips U-L-M Photonics* EP-VECSELs. The most relevant device parameters of the three characterized EP-VECSELs are summarized in Table 6.1.

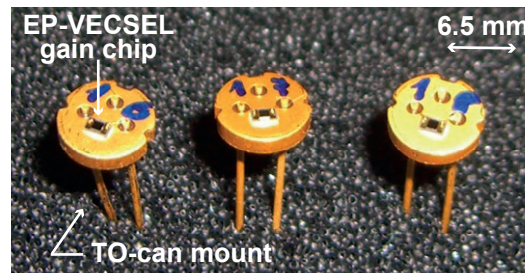


Figure 6.1 Image of the three characterized *Philips U-L-M Photonics* EP-VECSELs, individually mounted on a TO-can mount.

Although there are some design differences to our EP-VECSELs, like the thickness of the CSL, the oxide aperture or the number of QWs, the general relations

between internal reflectivity, output power and achievable beam quality should be similar. This allowed us to investigate the influence of the n-DBR reflectivity on the beam quality to determine design guidelines for our own future designs.

device (n-DBR pairs)	field enhancement	n-DBR reflectivity	CSL thickness
13	35	89%	150 μm
11	22	82%	56 μm
9	12	71%	60 μm

Table 6.1: Overview of the relevant device parameters of the characterized EP-VECSELS from *Philips U-L-M Photonics*.

6.2 Electrical and cw multi-mode characterization

The effect of the different field enhancement of the devices becomes evident when we compare the cw multi-mode LIV-curves. The LIV-curves for the sample with the highest (13 n-DBR pairs) and the lowest field enhancement (9 n-DBR pairs) are plotted in Figure 6.2.

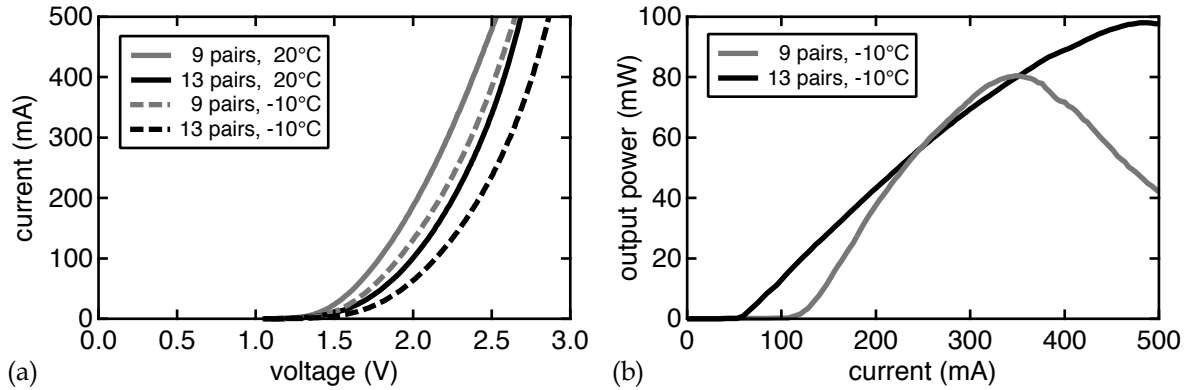


Figure 6.2 (a) IV-curves of the two different devices measured at -10°C (dashed) and 20°C (solid). (b) cw multi-mode LI-curves at -10°C measured in a straight cavity using an OC with a ROC of 15 mm and a transmission depending on the field enhancement (9 pairs: 5.7%, 13 pairs: 10.6%).

Figure 6.2(a) compares the IV-curves of the two devices for two different heatsink temperatures. The device with 9 pairs shows a lower voltage drop and both devices show an increase in voltage with decreasing temperature, as one would expect from the semiconductor material.

The LI-characteristics in Figure 6.2(b) show the cw multi-mode output power of the two lasers at a heatsink temperature of -10°C , measured in a straight cavity with an OC with a ROC of 15 mm. The optimal transmission for the highest output power depends on the average field enhancement in the QWs of the active region of the structure. The optimum found was 10.6% for the 13-pair device and 5.7% for the 9-pair device. As expected, the 13-pair device reaches a higher output power due to higher gain (see Chapter 2). On the other hand, the thicker CSL, which introduces a higher optical loss due to FCA, limits the achievable output power.

6.3 Beam quality characterization

To determine the beam quality of the EP-VECSELs, the three devices were characterized in a straight cavity using OCs with different transmission values and a ROC of 15 mm. In each case, the laser cavity was optimized for the highest output power with the best beam quality (lowest M^2 -value). Table 6.2 shows a summary of the best measurement for each of the three devices.

device (n-DBR pairs)	transmission OC	output power	M^2 -value
13	10%	34 mW	2.6
11	5%	15.1 mW	1.1
9	2.5%	8.2 mW	1.1

Table 6.2: Beam quality measurements of the *Philips U-L-M Photonics* EP-VECSELs and the cavity configuration.

For the EP-VECSEL with 13 n-DBR pairs, an output power of 34 mW with an $M^2 = 2.6$ is obtained. For the other samples with a reduced number of n-DBR pairs we could achieve fundamental transverse-mode operation with an $M^2 = 1.1$, but at a reduced output power level of 15.1 mW and 8.2 mW for the 9- and 11-pair devices, respectively. The measurements demonstrate that a highly reflective intermediate DBR can reduce the mode control of the OC and thus the transverse beam quality. A trade-off between high output power and good beam quality needs to be accepted.

6.4 Spectral gain characterization

The EP-VECSEL gain structure is a resonant structure and thus, dependent on the strength of the field enhancement, its gain bandwidth is limited (see Chapter 2). Furthermore, the gain spectrum of an EP-VECSEL shifts depending on the heatsink temperature and the injected electric current due to the temperature dependence of the refractive index. Therefore, we have characterized the spectral bandwidth and the small-signal gain as a function of wavelength, temperature and electric current. This requires the measurement of the wavelength-dependent reflectivity of a pumped EP-VECSEL gain chip.

6.4.1 Measurement setup

The setup we used for this purpose is a high-precision reflectivity measurement system [60]. A schematic of the setup is shown in Figure 6.3.

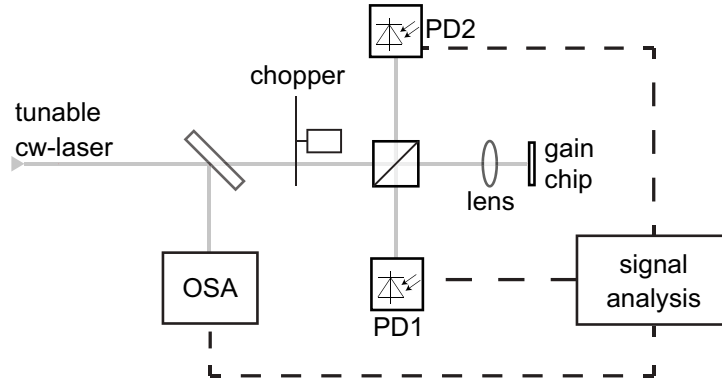


Figure 6.3 Schematic of the spectral gain measurement setup. The beam of a tunable cw Ti:Sapphire laser is first split by a 50:50 beam-splitter. One part of the beam is focused onto the pumped EP-VECSEL gain chip and the amplified beam is detected with PD1. The other part of the beam is detected with PD2 and used as a reference. The chopper is used to detect the offset on PD1 due to EL from the gain chip.

As a laser source we used a commercially available cw Ti:Sapphire Laser (*Spectra Physics 3900S*) with a lasing linewidth < 0.15 nm. The output power is attenuated to 3 mW at 960 nm and drops to 2 mW at higher wavelength. An optical spectrum analyzer (OSA) is used for wavelength control using a motion controller and a feedback loop.

The beam of the laser is first split by a non-polarizing 50:50 beam-splitter. One part of the beam is focused onto the pumped EP-VECSEL gain chip using a lens ($f = 20$ mm). This results in a beam spot diameter of below $25\text{ }\mu\text{m}$. The probe beam is amplified by the gain chip and detected with a silicon photodiode (PD1). The other part of the beam is detected with PD2 and used as a reference. The chopper is utilized to detect the offsets on the PDs due to the EL from the gain chip.

For each measured data point of the gain spectrum, the emission wavelength of the laser is tuned with a birefringent filter and the absolute value of the reflectivity of the gain chip is determined. This requires a calibration of the setup with a highly reflective mirror of known reflectivity R_{HR} . The absolute reflectivity of the gain chip is then given by

$$R_{\text{GC}}(\lambda) = R_{\text{HR}}(\lambda) \frac{S_{\text{HR,PD2}}(\lambda) S_{\text{GC,PD1}}(\lambda)}{S_{\text{HR,PD1}}(\lambda) S_{\text{GC,PD2}}(\lambda)}. \quad (6.1)$$

By additionally averaging over 200 iterations of the measurement signal an absolute accuracy of $< 0.1\%$ is obtained. With each sample this procedure is repeated for different injected electric currents and heatsink temperatures.

6.4.2 Spectral gain measurements

The characterized samples are the *Philips U-L-M Photonics* EP-VECSELs with 9 and 13 n-DBR pairs. Figure 6.4(a) shows the measured gain spectra of the EP-VECSEL gain chip with 9 n-DBR pairs as a function of the injected electric current. The unpumped structure (solid black line) shows strong absorption mainly due to the quantum-well absorption and the FCA in the device. The modulations on the gain spectra originate from the CSL, which acts as a Fabry-Perot-etalon and thus a spectral filter because of the residual reflection of the AR-coating. The spacing of the Fabry-Perot fringes can be used to calculate the thickness of the CSL and yields a value of $60\text{ }\mu\text{m}$. Increasing the injected current first results in transparency of the structure (dark gray solid line), for higher currents gain starts to build up.

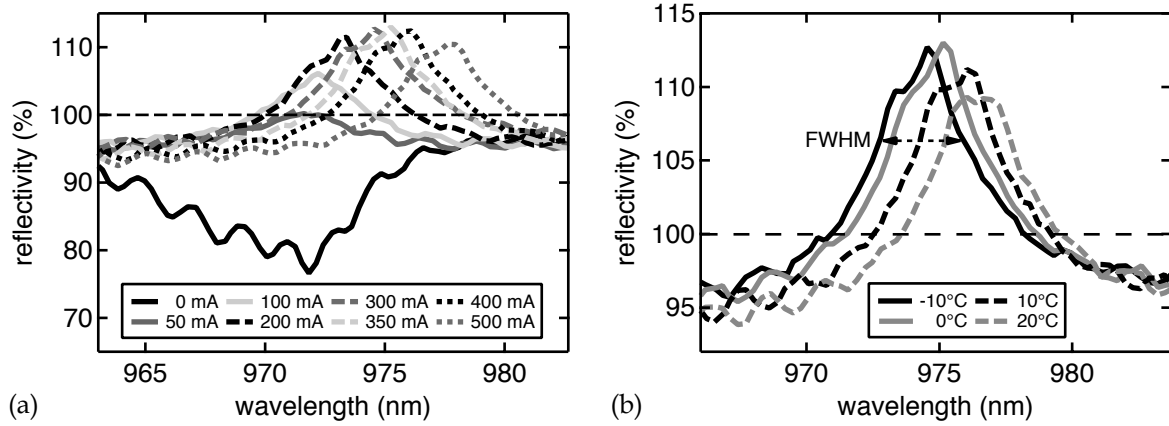


Figure 6.4 Measured gain spectra for the EP-VECSEL with an intermediate n-DBR with 9 quarter-wave layer pairs (i.e. with 9 n-DBR pairs). (a) Reflectivity spectra of the EP-VECSEL for different injected electric currents at a constant heatsink temperature of -10°C . A small-signal gain of 13% is reached at 350 mA. The modulations on the spectra arise from the CSL, which acts as a weak sub-cavity due to AR-coating imperfections. (b) Temperature dependence of the gain for an injected electric current of 300 mA. The gain bandwidth of the device is around 3.1 nm (FWHM).

The unsaturated gain is defined by a reflectivity exceeding 100%, indicated by the black dashed line across. The maximum unsaturated small signal gain of 13% is reached at 350 mA. For even higher currents, a lower gain is observed, because the peak gain wavelength of the QWs shifts stronger with increased temperature than the structural resonance wavelength. This thermal wavelength shift is caused by the Joule heating associated with the electrical loss of the device. Another contribution comes from the optical loss mainly caused by FCA. Figure 6.4(b) shows the measured gain spectra for different heatsink temperatures and a constant injected current of 300 mA. For every current there is a temperature, at which the cavity resonance and the peak gain of the QWs overlap. Decreasing the heatsink temperature results in a larger detuning and thus allows for higher pump currents until this operation point is reached. For a current of 300 mA, a temperature of 0°C is the optimum operation point for maximum gain.

The negative etalon effect caused by the CSL becomes evident when we compare these spectra. At a heatsink temperature of 20°C the minimum of the modulation overlaps with the peak of the gain spectrum, reducing the maximum achievable gain. This device exhibits a gain bandwidth of about 3.1 nm (FWHM) and the gain peak shifts with around 13.1 nm/A and 0.067 nm/K. This corresponds to the typical value

of around 0.07 nm/K found in literature [16]. These measured values are an average over all measured spectra.

Figure 6.5 shows the current- and temperature-dependent gain spectra of the device with 13 n-DBR pairs. The resolution of the gain spectra is limited to 0.15 nm due to the accuracy of the feedback loop, which controls the wavelength of the probe laser. This limits the number of data points for these spectra. In comparison to the EP-VECSEL gain chip with 9 pairs, the maximum achievable small signal gain is significantly higher with 58.6%. On the other hand, the stronger resonance results in a much lower gain bandwidth of around 0.9 nm (FWHM). The temperature-dependent measurements in Figure 6.5(b) show again the spectral filtering effect of the CSL, reducing the achievable small-signal gain at 0°C by almost 15%. The thickness of the CSL calculated from the modulation on the spectra is 150 μm for this device. The structure exhibits a peak gain shift of around 12.8 nm/A and 0.071 nm/K.

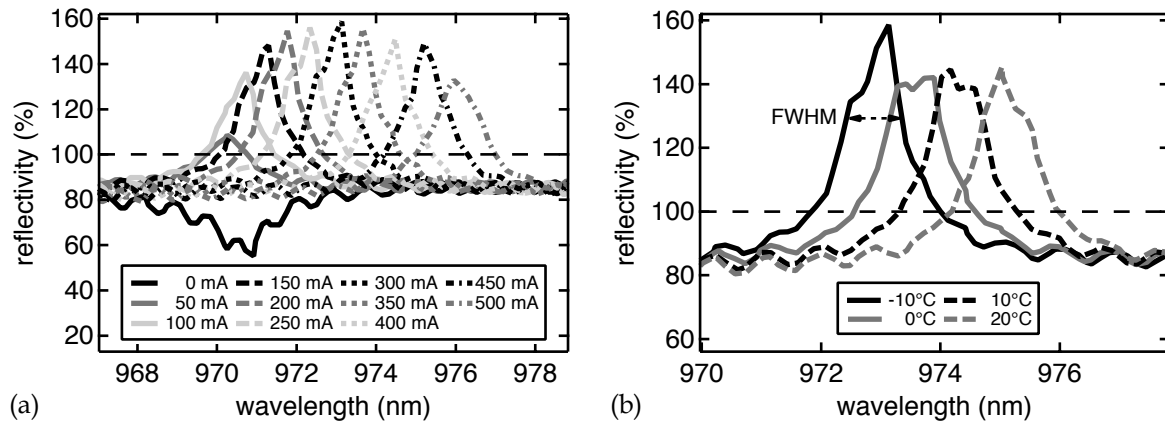


Figure 6.5 Measured gain spectra for EP-VECSEL device with an intermediate n-DBR with 13 quarter-wave layer pairs (i.e. 13 n-DBR pairs). (a) Reflectivity spectra of the EP-VECSEL for different injected electric currents at a constant heatsink temperature of -10°C. The resolution is limited by the accuracy of the feedback loop controlling the wavelength of the probe laser. A small-signal gain of 58.6% is reached at 300 mA. (b) Temperature dependence of the gain spectra for a constant injected electric current of 300 mA. The bandwidth of the structure is around 0.9 nm (FWHM).

All gain parameters extracted from the spectral gain measurements of the two EP-VECSEL gain chips are summarized in Table 6.3.

parameter	9 n-DBR pairs	13 n-DBR pairs
small-signal gain (at -10°C)	13% (350 mA)	58.6% (300 mA)
gain bandwidth (FWHM)	3.1 nm	0.9 nm
peak gain shift with temperature	0.067 nm/K	0.071 nm/K
peak gain shift with current	13.1 nm/A	12.8 nm/A

Table 6.3: Summary of the gain parameters extracted from the spectral gain measurements of the two EP-VECSELS.

6.5 Gain saturation measurements

As already described in Chapter 3, semiconductor gain materials are subject to strong gain saturation effects. To achieve stable modelocked operation, the absorber must saturate before the gain. This requires a good knowledge of the gain saturation behavior of the EP-VECSEL gain chip to choose the correct cavity configuration and SESAM properties. To measure the gain saturation behavior we used a high-precision non-linear reflectivity measurement setup. The measurement method and the setup will be described in the next section.

6.5.1 Measurement method and setup

Figure 6.6 shows the basic approach to determine the saturation behavior of an EP-VECSEL gain chip. First it is necessary to know the exact wavelength of the gain maximum λ_{peak} for a certain injected electric current and heatsink temperature. This is depicted in Figure 6.6(a), using the measured gain spectra of the device with 9 n-DBR pairs at a heatsink temperature of -10°C as an example. Then it is possible to tune a pulsed probe laser to this wavelength and to determine the reflectivity as function of fluence on the chip for this fixed wavelength. An example measurement is shown in Figure 6.6(b) for a wavelength of 974.4 nm for the probe laser, a heatsink temperature of -10°C and a pump current of 300 mA.

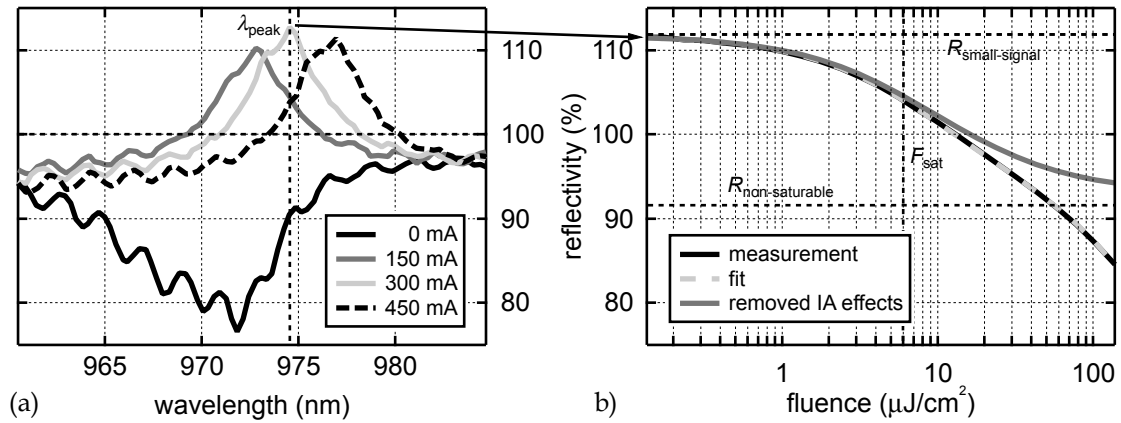


Figure 6.6 Measurement method for the gain saturation of EP-VECSELs. (a) Gain spectrum of the EP-VECSEL device with an intermediate n-DBR with 9 quarter wave layer pairs for different injected electric currents at -10°C . The maximum gain is reached at the wavelength λ_{peak} , to where the wavelength of the picosecond probe laser is tuned for the measurement of the gain saturation. (b) Gain saturation measurement (black) at an injected pump current of 300 mA and -10°C heatsink temperature. From the fit function (light gray, dashed) the parameters small-signal gain reflectivity $R_{\text{small-signal}}$, saturation fluence F_{sat} , the non-saturable reflectivity $R_{\text{non-saturable}}$ and the strength of the induced absorption F_2 can be extracted. The solid dark gray curve shows the gain saturation for which the induced absorption (IA) effects were numerically removed.

From this measurement the saturation fluence, small-signal gain, non-saturable losses and the effect of induced absorption (IA) can be extracted by fitting the data with an appropriate fit-function. The fit-function will be described later in more detail.

A schematic of the setup we use for the measurement of the fluence-dependent reflectivity is shown in Figure 6.7. It is based on the non-linear reflectivity measurement setup presented in Chapter 3 and was slightly modified for gain measurements [60]. For the gain saturation measurements the modelocked Ti:sapphire laser (*Spectra Physics Tsunami*) is tuned to emit pulses with a pulse duration of about 1.4 - 1.8 ps, depending on the exact wavelength. This is necessary to limit the emission bandwidth of the laser to about 0.6 nm. Otherwise it would not be possible to accurately characterize the EP-VECSELs since they exhibit a narrow gain spectrum.

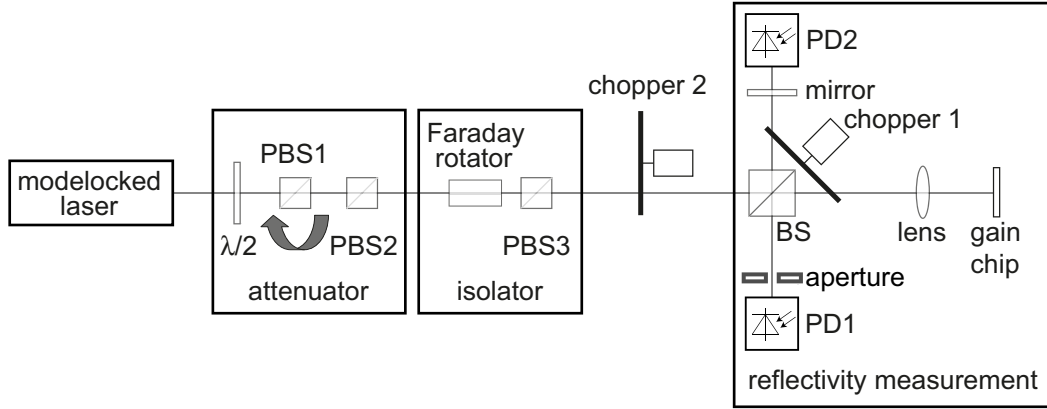


Figure 6.7 Schematic of the gain saturation measurement setup. The setup is a modified version of the non-linear reflectivity measurement setup presented in Chapter 3. The second chopper is synchronized to the first chopper ($f_{\text{chopper1}} = 2 f_{\text{chopper2}}$) and is used to measure the offset on PD1 due to the EL from the gain chip. The aperture is used to suppress the strongly diverging EL.

The fluence-dependent reflectivity is measured by adjusting the power of the probe laser with a controllable attenuation stage and determining the absolute reflectivity value as it has already been described in Chapter 3 for SESAMs. The setup features an additional chopper (chopper 2), which is synchronized to the first chopper ($f_{\text{chopper1}} = 2 f_{\text{chopper2}}$). It is used to determine the offset on PD1 due to the EL from the EP-VECSEL gain chip. The additional aperture is used to suppress the strongly diverging EL. Details about the data acquisition and calculation of the reflectivity can be found in [60].

To extract the relevant parameters from the measurement data, a fit-function based on the partial differential equation for absorber saturation in SESAMs [50] and the Frantz-Nodvik-equation for gain saturation [61] is used. Here, only the final equation of the fit-function will be given, a complete mathematical description and derivation can be found in [50, 60]. The reflectivity model function is

$$R(F) = \exp[g(F)] = R_{\text{ns}} \frac{\ln \left\{ 1 + \exp \left(\frac{R_{\text{ss}}}{R_{\text{ns}}} \right) \left[\exp \left(\frac{F}{F_{\text{sat}}} \right) - 1 \right] \right\}}{\frac{F}{F_{\text{sat}}}} \exp \left(-\frac{F}{F_2} \right), \quad (6.2)$$

where R_{ss} ($R_{\text{small-signal}}$) represents the reflectivity of the small-signal gain. The saturation fluence F_{sat} is defined as the fluence, where the gain has dropped to

approximately $(1 - 1/e) \approx 63\%$ of its initial value. As already mentioned in Chapter 3, a numerical correction must be applied for Gaussian intensity distributions, since Equation (6.2) is only valid for flat-top beams.

For our EP-VECSELs some approximations for the fit function need to be re-evaluated. In the derivation of the fit function we used the approximation $\exp(g_{ss}) \approx 1 + g_{ss}$. This approximation is still good for the device with 9 n-DBR pairs, however, slightly exceeded for the 13 pair structure, which has a small-signal gain $\approx 58\%$. Nevertheless, the parameters extracted from the fit give approximate values of how the device compares to the less resonant one. The second approximation was made with regards to the non-saturable losses. The non-saturable losses are higher due to FCA in the thick CSL. We can take this into account when we introduce an effective small-signal gain

$$g_{ss,eff} = g_{ss} + (100 - R_{ns}) , \quad (6.3)$$

which accounts for the fact that these additive losses also need to be compensated before reaching the gain threshold. Then the definition of the saturation fluence F_{sat} mentioned above is valid also for these devices. The small-signal gain g_{ss} is still defined as a reflectivity value exceeding 100%.

6.5.2 Gain saturation measurements

Figure 6.8 shows the gain saturation measurements for the two devices at a heatsink temperature of -10°C and an injected electric current of 300 mA. The EP-VECSEL with 9 n-DBR pairs exhibits a saturation fluence $F_{sat} = 6.2 \mu\text{J}/\text{cm}^2$ and a small-signal gain $g_{ss} = 12\%$, the device with 13 pairs has a saturation fluence $F_{sat} = 3.2 \mu\text{J}/\text{cm}^2$ and a small-signal gain $g_{ss} = 58.3\%$. The fit function for the 13-pair device still fits the measurements data very well, even though the approximations assumed for the fit function become less valid. Consequently, the extracted parameters should be seen only as an approximation for this device. For both measurements the small-signal gain shows excellent agreement with the value determined from the spectral gain measurements. All parameters extracted from the fit function are summarized in Table 6.4.

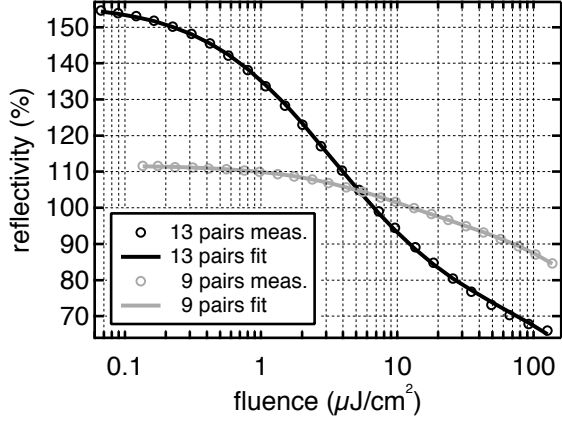


Figure 6.8 Gain saturation measurements of the two devices at a heatsink temperature of -10°C and an injected electric current of 300 mA. The fit function (solid line) is modeled to the measurement data (circles).

parameter	9 n-DBR pairs	13 n-DBR pairs
F_{sat}	$6.2 \mu\text{J}/\text{cm}^2$	$3.2 \mu\text{J}/\text{cm}^2$
g_{ss}	12%	58.3%
R_{ns}	92.3%	69.4%
F_2	$1.26 \text{ mJ}/\text{cm}^2$	$1.0 \text{ mJ}/\text{cm}^2$

Table 6.4: Summary of the gain saturation parameters extracted from the fit function for the two EP-VECSELS, measured at -10°C heatsink temperature and 300 mA injected pump current.

6.6 Passive modelocking experiments

Using the *Philips U-L-M Photonics* EP-VECSEL with 9 n-DBR pairs, we have demonstrated fundamental TEM₀₀-mode operation (Section 6.3). Furthermore, the device exhibits a high gain bandwidth of 3.1 nm (FWHM) at a moderate saturation fluence of 6.2 $\mu\text{J}/\text{cm}^2$. This makes the EP-VECSEL with 9 n-DBR pairs very interesting for passive modelocking experiments. In this section, the cavity setup for the modelocking experiments and the obtained results will be presented.

6.6.1 Cavity setup

For stable modelocked operation the absorber needs to saturate faster than the gain (see Chapter 3). The measured gain saturation fluence of the EP-VECSEL allowed us to select a suitable SESAM with the correct saturation parameters. In addition, we further enhanced the SESAM saturation with a laser cavity design that supports a smaller cavity mode size on the SESAM than on the gain chip. Figure 6.9 shows a schematic of the cavity setup for the modelocking experiments.

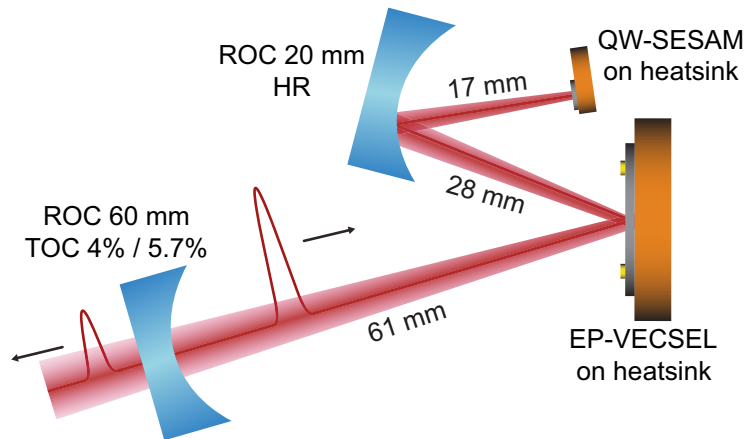


Figure 6.9 Schematic of the cavity setup for the modelocking experiments. The two different used OCs have a ROC of 60 mm and a transmission of 4% and 5.7%, respectively, the highly reflective mirror (HR) has a ROC of 20 mm. Both the EP-VECSEL gain chip and the QW-SESAM are mounted on a heatsink for temperature tuning and stabilization. The resulting beam diameters are $\approx 100 \mu\text{m}$ on the EP-VECSEL and $\approx 40 \mu\text{m}$ on the SESAM.

The laser cavity was set up in a Z-type configuration to match the pumped region on the EP-VECSEL of 100 μm and to be able to focus onto the SESAM with a resulting spot size of $\approx 40 \mu\text{m}$ in diameter. The OC had a ROC of 60 mm and a transmission of 4%. The highly reflective folding mirror to focus onto the SESAM had a ROC of

20 mm. To match the gain saturation of the EP-VECSEL, we used a low-saturation fluence QW-SESAM. It is based on a single AlAs-embedded $\text{In}_x\text{Ga}_{(1-x)}\text{As}$ QW and a 4-pair semiconductor AR-coating with a fused-silica (FS) layer on top to enlarge the field enhancement in the absorber. The measured saturation fluence for the SESAM was $2.9 \mu\text{J}/\text{cm}^2$ and the modulation depth is 3.9%, measured at room temperature at a wavelength of 967 nm (see Chapter 3 for the measurement method and setup).

6.6.2 *Passive modelocking results*

Stable and self-starting modelocking was achieved at a pump current of 480 mA and a heatsink temperature of -17.8°C . With an increased heatsink temperature the small-signal gain of the device decreases, as presented in Figure 6.4(b). This reduces the intra-cavity power of the laser such that the SESAM is not sufficiently saturated anymore to support stable modelocked operation. The SESAM was stabilized to a temperature of 37.2°C to shift the absorption to a longer wavelength, where the saturation fluence for the laser wavelength of 975.1 nm is very similar to the values measured at 967 nm.

The average output power was 7.6 mW with a pulse duration of 9.5 ps (Figure 6.10). The resulting fluences on the EP-VECSEL and the SESAM were $\approx 1.7 \mu\text{J}/\text{cm}^2$ and $\approx 9.9 \mu\text{J}/\text{cm}^2$, respectively. The optical spectrum (Figure 6.10(a)) is centered at 975.1 nm and has a bandwidth of 0.43 nm (FWHM). Figure 6.10(b) shows the intensity autocorrelation and the fit of a 9.5-ps sech^2 pulse. The time-bandwidth-product (TBP) $\Delta\nu\Delta\tau = 1.28$, which corresponds to about four times the transform limit. This means that the pulses exhibit a strong chirp. This is most likely caused by large GDD-values of the resonant gain structure [47]. The microwave spectrum in Figure 6.10(c) is measured in a 5 MHz frequency span and a resolution bandwidth of 100 kHz and is centered around 1.4 GHz, corresponding to the fundamental repetition frequency of the cavity. Figure 6.10(d) shows a beam quality measurement of the modelocked laser with an $M^2 = 1.1$ in both orthogonal directions.

With a higher OC transmission of 5.7% an average output power of 13.6 mW with 31-ps pulses at the same repetition rate of 1.4 GHz was achieved. In this case the pump current was 473 mA, the heatsink temperature of the EP-VECSEL -16.9°C and the SESAM was stabilized to 37.6°C .

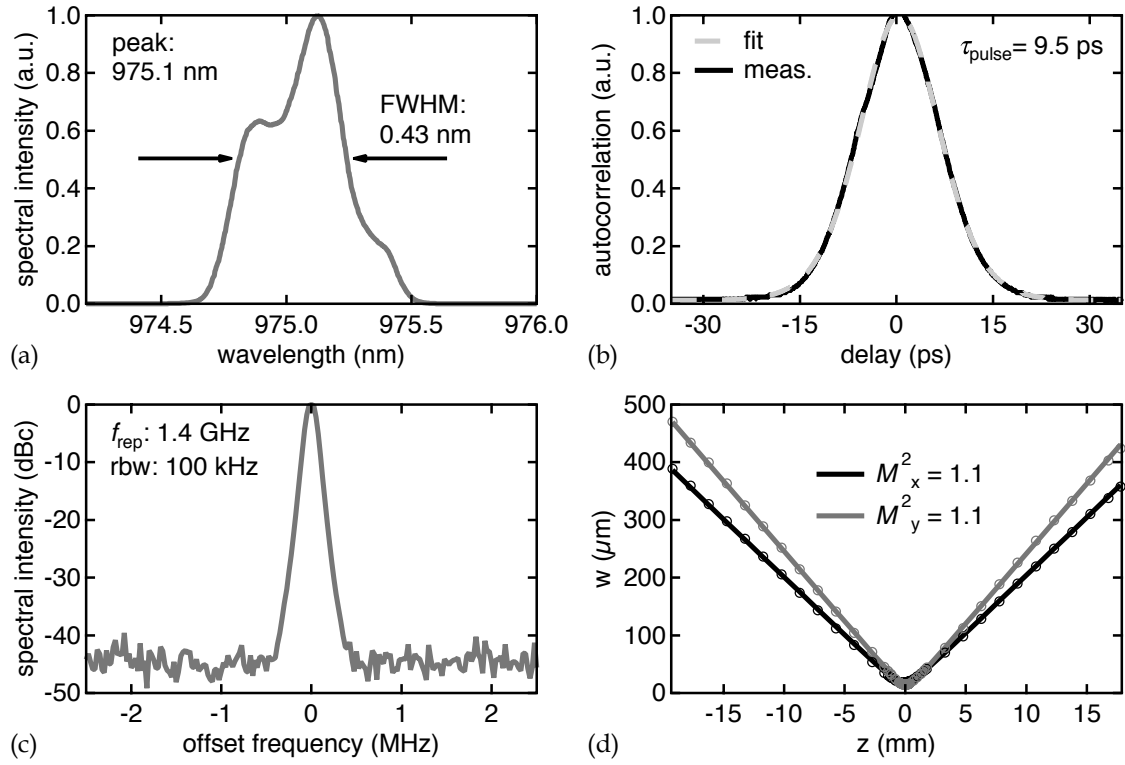


Figure 6.10 Modelocking results obtained from the EP-VECSEL with an intermediate n-DBR with 9 quarter-wave layer pairs and a low-saturation fluence QW-SESAM. (a) Measured optical spectrum with a width of 0.43 nm (FWHM) centered at 975.1 nm. (b) Measured autocorrelation trace (black solid line) and fit of a 9.5-ps sech²-pulse (gray dashed line). (c) Measured microwave spectrum centered at the fundamental repetition frequency of 1.4 GHz with a resolution bandwidth (RBW) of 100 kHz. (d) Beam quality measurement showing an $M^2 = 1.1$ in both orthogonal directions.

These passive modelocking results were an important intermediate step, showing that an EP-VECSEL with an optimized intermediate n-DBR reflectivity is suitable for ultrafast pulse generation.

Chapter 7

EP-VECSEL design improvements

The main limitations we identified from our initial design were thermal limitations and insufficient beam quality (see Chapter 5). In this chapter, design improvements to overcome these limitations are presented. First, an electrical improvement of the p-doped DBR is described, with the aim to reduce Joule-heating of the devices due to ohmic losses. Next, the improved thermal management of the EP-VECSELs using a new mask-set is presented. Then an optimization of the beam quality based on the findings from Chapter 6 is described. In the last section, an overview of the optimized design is given.

7.1 Electrical optimization of the p-DBR

In our EP-VECSEL, a major contribution of the electrical resistance comes from the p-doped DBR on the bottom of the structure. The p-DBR resistance itself is mainly due to the high barriers for carriers at the material interfaces in the DBR. At the same time, the holes in the p-doped material exhibit a smaller mobility than the electrons in the n-doped material. Furthermore, the probability for hole tunneling is decreased. This means that a large part of the device resistance is given by the barrier regions in the p-doped DBR [62, 63].

A standard AlAs/GaAs DBR with abrupt interfaces exhibits band discontinuities at each interface [64, 65]. The equilibration of the Fermi levels by local charge carrier redistribution leads to a bending of the band edges. Depending on the work function and the carrier concentrations of the used material, this may result in sharp potential barriers. This is shown in Figure 7.1 for the case of a p-doped AlAs/GaAs DBR with

abrupt interfaces. These barriers lead to decreased thermal conductivity on the one hand [66, 67], and to increased electrical resistance on the other hand.

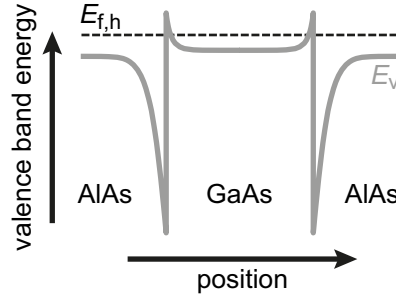


Figure 7.1 Valence band bending and potential barriers at the abrupt heterointerface between AlAs and GaAs in p-doped material.

In our design, having the p-DBR as highly reflective end mirror on the bottom of the structure is essential for achieving a homogeneous, confined current injection profile. This is necessary to support fundamental transversal-mode operation essential for stable modelocking and has already been discussed in Chapter 2. However, a highly reflective p-DBR consisting of many quarter-wave layer pairs necessary for achieving high reflectivity values increases the device resistance substantially. Hence, to reduce electrical losses in the structure, an electrical optimization of the p-DBR is unavoidable.

7.1.1 *p-DBR design for low electrical losses*

To realize a p-doped DBR with reduced electrical resistance, various concepts have been published. For metal-organic vapor phase epitaxy (MOVPE)-grown devices a continuous grading between the two mirror materials can be realized rather easily [68], whereas this is more challenging for MBE-grown devices. One possibility is to ramp the temperature of the material cells in the MBE [28, 69], although the cell behavior strongly depends on the size of the cells. A more common method is the use of a digital alloy [70-72]. Another solution is to use discrete intermediate material composition steps between the two DBR materials [27].

In all cases the electrical performance may be further increased by utilizing different doping schemes such as modulation doping [63, 72], where the doping profile is tailored along the grading or delta doping [73], where an extra sheet charge is introduced between the material interfaces. Another possibility is the use of step doping, where the whole grading is highly doped.

In our initial design, we went for the approach of using discrete material composition steps. To further optimize device performance we then went to a digital alloy design. The option of step doping was also investigated. The initial and the improved designs will be discussed in the following sections.

Figure 7.2(a) shows the simulated valence band characteristic for an AlAs/GaAs interface in p-doped material (adapted from [74]). In case of the abrupt interfaces one can clearly see the sharp and high potential barriers. Using a stepped interface improves the transition; the best solution is a linear grading. In Figure 7.2(b) a TEM-image of all three cases is shown. In case of the stepped grading the individual materials are visible. In case of the graded p-DBR there is no transition visible, even though the air/semiconductor interface is sharply resolved on the right hand side of the image.

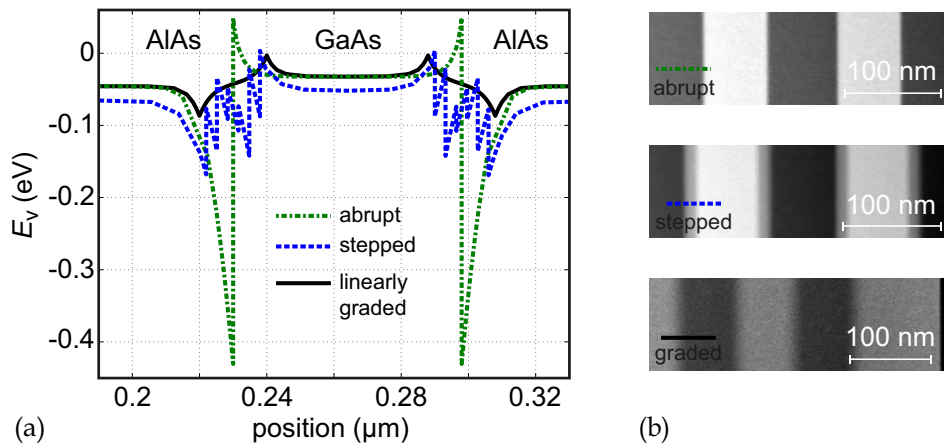


Figure 7.2 Valence band characteristic for different interfaces between p-doped AlAs/GaAs: (a) Simulation of the valence band for abrupt, stepped and graded interfaces (adapted from [74]). (b) TEM-images of the three different interfaces.

Step grading using different material composition

In our first EP-VECSEL design we implemented a stepped molefraction grading, as shortly described in Chapter 2. Figure 7.3 shows the design details of the used AlAs/GaAs p-DBR with a stepped molefraction grading consisting of 5 intermediate $\text{Al}_x\text{Ga}_{(1-x)}\text{As}$ steps of 3.2 nm thickness. In Figure 7.3(a), the refractive index profile (solid black line) and the squared electric field of the standing wave pattern (solid dark gray line) of one p-DBR pair are plotted. The doping level is kept constant (solid light gray line). The molefraction x of the discrete steps in the grading is plotted in Figure 7.3(b) as a function of the grading position.

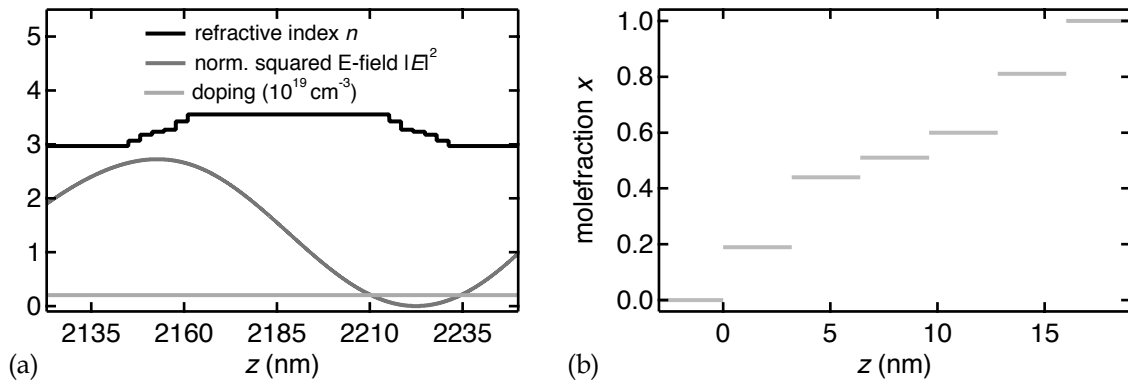


Figure 7.3 Design details of a AlAs/GaAs p-DBR with a stepped molefraction grading consisting of 5 intermediate $\text{Al}_x\text{Ga}_{(1-x)}\text{As}$ steps of 3.2 nm thickness. (a) Refractive index profile (solid black line), squared electric field of the standing wave pattern (solid dark gray line) and doping level (solid light gray line) of one p-DBR pair. (b) Molefraction x of the discrete steps in the grading.

Even though a linear or parabolic grading is expected to perform better, a stepped grading, which is in principal easier to grow, can also be further optimized. The most important parameters for optimization are the thickness, the number of steps and the molefraction x . However, the number of steps and the molefraction cannot be independently changed since they are restricted by the number of cells and calibrated growth rates of the MBE. Using our simulation model we have investigated possible designs for a p-DBR with a stepped grading. Figure 7.4 shows the simulated influence of the number and thickness of steps in the grading on the resistance (Figure 7.4(a)) and reflectivity (Figure 7.4(b)) of the p-DBR. For the simulation, a p-DBR with 30 quarter-wave layer pairs of GaAs/ $\text{Al}_{0.9}\text{Ga}_{0.1}\text{As}$ and a molefraction grading between the two materials was implemented. The

molefraction x of the steps was equally distributed with $x \in [0, 0.9]$. The radius of the devices was set to $80 \mu\text{m}$ and they were fully contacted on both sides. The doping profile was chosen like in the first realized EP-VECSEL, namely $(5, 4, 3, 2) \cdot 10^{18} \text{ cm}^{-3}$ for the DBR pairs (1 - 15, 16 - 20, 21 - 25, 26 - 30), respectively. The model calculates the current as the ohmic current and the thermionic emission at the barriers. Tunneling is neglected. The specified resistance is given for a current of 400 mA.

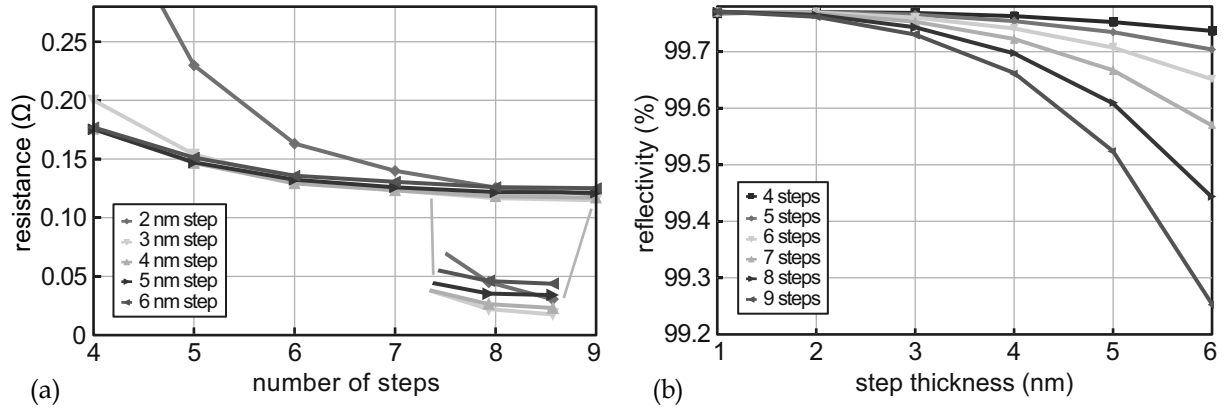


Figure 7.4 Simulated resistance (a) and reflectivity (b) of an optimized p-DBR with stepped molefraction grading for different thicknesses and number of steps.

A higher number of steps leads to smaller potential barriers and consequently lower resistance (Figure 7.4(a)). The optimal thickness depends on the number of steps. As long as the number of steps and the step thickness are not too high, the overall reflectivity of the p-DBR is not significantly influenced by the grading. To give a specific example, increasing the number of steps from 5 to 7 while maintaining the thickness of 3 nm leads to a reduction of the resistance by 27%. The reason for this can be found in the correlation of the barrier height with the density of the accumulated carriers. Spreading the carriers over a larger distance reduces the barriers and thus the resistance.

Digital alloy for linear and bi-parabolic gradings

To realize a more or less continuous grading with our MBE-system, a digital alloy grading was developed. The grading consists of a certain number of GaAs and $\text{Al}_{0.9}\text{Ga}_{0.1}\text{As}$ layer pairs with a fixed pair thickness in the order of 1 – 2 nm. Across the grading the duty cycle is changed from nearly completely GaAs to nearly completely $\text{Al}_{0.9}\text{Ga}_{0.1}\text{As}$. The very small pair thickness and the finite growth transition result in a

continuous grading. The material ratio allows for the design of different grading types, like a linear or bi-parabolic grading. The design details for a bi-parabolic grading are shown in Figure 7.5. This grading type should in theory result in the flattest valence band and thus the lowest resistance.

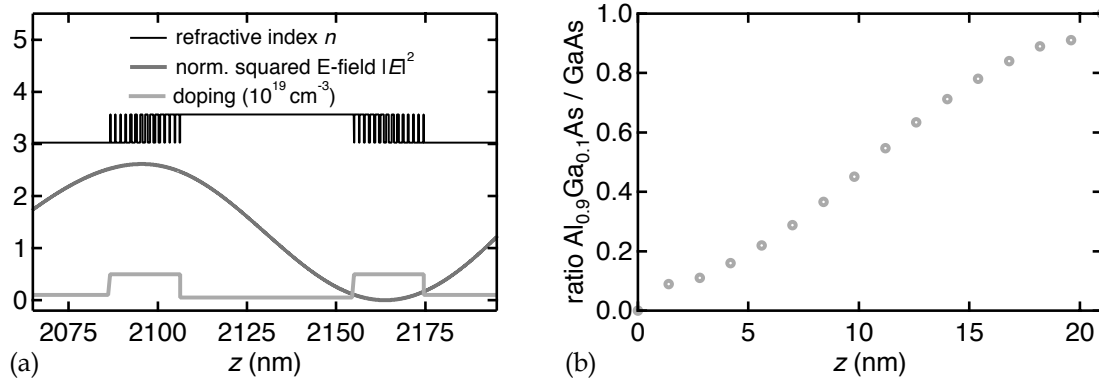


Figure 7.5 Design details of an $\text{Al}_{0.9}\text{Ga}_{0.1}\text{As}/\text{GaAs}$ p-DBR with a bi-parabolic digital alloy grading. (a) Refractive index profile (solid black line), squared electric field of the standing wave pattern (solid dark gray line) and doping levels (solid light gray line) of one p-DBR pair. (b) Ratio of $\text{Al}_{0.9}\text{Ga}_{0.1}\text{As}$ to GaAs as a function of the grading position.

Figure 7.5(a) shows the refractive index profile (solid black line) with the varying duty cycle of the materials (see also Figure 7.5(b)) and the squared electric field of the standing wave pattern (solid dark gray line) for the bi-parabolic grading. The doping level (solid light gray line) can be increased at the position of the gradings to further improve the electrical resistance.

7.1.2 Realized designs of the improved p-DBR

We have realized three different p-DBR designs based on the digital alloy grading. Additionally, a p-DBR without grading (abrupt interfaces) was grown as a reference. Table 7.1 gives an overview over the different designs and the doping scheme of the grading. The bulk doping levels used for all p-DBRs for GaAs and $\text{Al}_{0.9}\text{Ga}_{0.1}\text{As}$ were $0.5 \cdot 10^{18} \text{ cm}^{-3}$ and $1 \cdot 10^{18} \text{ cm}^{-3}$, respectively. For the bi-parabolic digital alloy, we chose 14 pairs for the grading and a pair thickness of 1.4 nm based on [75, 76]. This results in an overall thickness of the grading of 19.6 nm and does not yet reduce the reflectivity of the entire p-DBR structure. On one sample with a bi-parabolic grading we additionally increased the doping in both gradings to $5 \cdot 10^{18} \text{ cm}^{-3}$ (step doping). To have a comparison, we also realized one p-DBR with a linear grading consisting of $5 \times 2 \text{ nm}$ pairs, based on the design we received from one of our collaborators.

The doping levels in the gradings of this device were chosen significantly higher ($7 \cdot 10^{18} \text{ cm}^{-3}$ in the antinode of the optical field and $5 \cdot 10^{19} \text{ cm}^{-3}$ in the node).

label	grading type	doping level grading
abrupt	no grading	-
bi-parabolic	bi-parabolic, 14 x 1.4 nm (19.6 nm)	$1 \cdot 10^{18} \text{ cm}^{-3}$
bi-parabolic, step doping	bi-parabolic, 14 x 1.4 nm (19.6 nm)	$5 \cdot 10^{18} \text{ cm}^{-3}$
linear, step doping	linear, 5 x 2 nm (10 nm)	$7 \cdot 10^{18} \text{ cm}^{-3}$ antinode, $5 \cdot 10^{19} \text{ cm}^{-3}$ node

Table 7.1: Overview of the different realized p-DBR designs.

7.1.3 Improvement of the measurement technique

To characterize the electrical behavior of different p-DBR designs, a test structure is necessary that allows for reliable and time-efficient testing of the devices. Two different possibilities are shown in Figure 7.6. Previously, we have grown our p-DBRs on SI-substrates on a highly doped contact layer (Figure 7.6(a)). For this measurement technique, a mesa is first dry-etched in the ICP to define the structure geometry. The electrical contacts are then defined on top of the mesa and on the contact layer beneath the p-DBR. This test structure works well, if the mesa diameter is kept below around $20 \mu\text{m}$. For larger diameters, the injected current does not necessarily flow uniformly through the device, but rather prefers the path along the side of the mesa due to the lower horizontal resistance in the contact layer. This leads to too high values for the electrical resistance, if homogenous current injection is assumed. Therefore, we developed a more reliable test structure, where the p-DBR is grown on a p-doped substrate (Figure 7.6(b)). Instead of defining the bottom contacts on the contact layer, the backside of the substrate is metallized. Additionally, the substrate is partly etched during the mesa etch to prevent the current from spreading too much in the substrate. This results in a homogenous current distribution and a reproducible measurement of the electrical resistance. For both test structures the electrical resistance is measured using a four-point IV-measurement between the two

contacts to eliminate the influence of the measurement cables and prober needles. The calculated substrate resistance is subtracted afterwards.

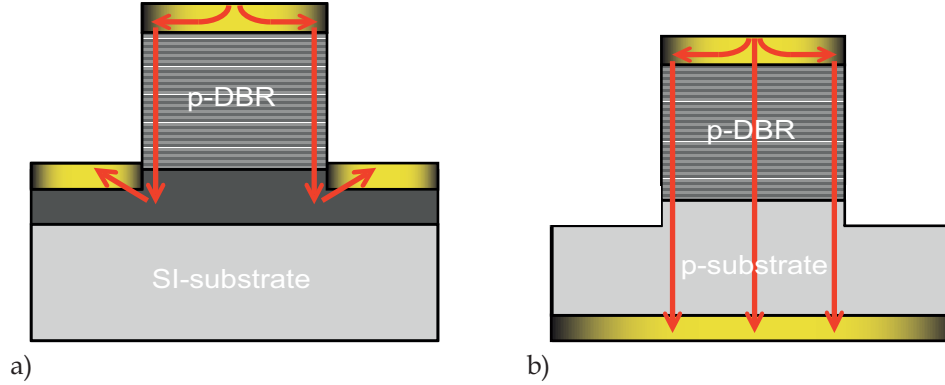


Figure 7.6 Schematic of two different electrical measurement techniques for the p-DBRs. (a) p-DBR grown on a semi-insulating (SI)-substrate. The contacts are defined on top of the mesa and on a highly doped contact layer underneath the p-DBR layer stack. (b) p-DBR grown on a p-doped substrate. The contacts are defined on top of the mesa and on the backside of the substrate.

7.1.4 Electrical measurements of the improved p-DBRs

All designs described in Section 7.1.2 were grown on p-doped substrates (Zn-dopant, $1 \cdot 10^{19} \text{ cm}^{-3}$) and fabricated according to the newly developed test structure. We chose 15 DBR-pairs for all devices. The different realized mesa-radii were $60 \mu\text{m}$, $90 \mu\text{m}$, $120 \mu\text{m}$ and $150 \mu\text{m}$. Four-point IV-measurements were performed with a current density of up to 5 kA/cm^2 . Figure 7.7(a) shows the measured IV-curves of the p-DBR with the abrupt interfaces in comparison to the p-DBRs with a digital alloy grading. The abrupt p-DBR shows a very high voltage drop of more than 8 V for a current density of around 1 kA/cm^2 . Above 1 kA/cm^2 , the voltage is again reduced presumably because of the strong heating due to the high resistance of the device. The digital alloy significantly reduces the voltage drop over the p-DBR from nearly 6 V to below 0.6 V at a current density of 3.5 kA/cm^2 . The voltage drop over the p-doped substrate is calculated and subtracted from the IV-curves.

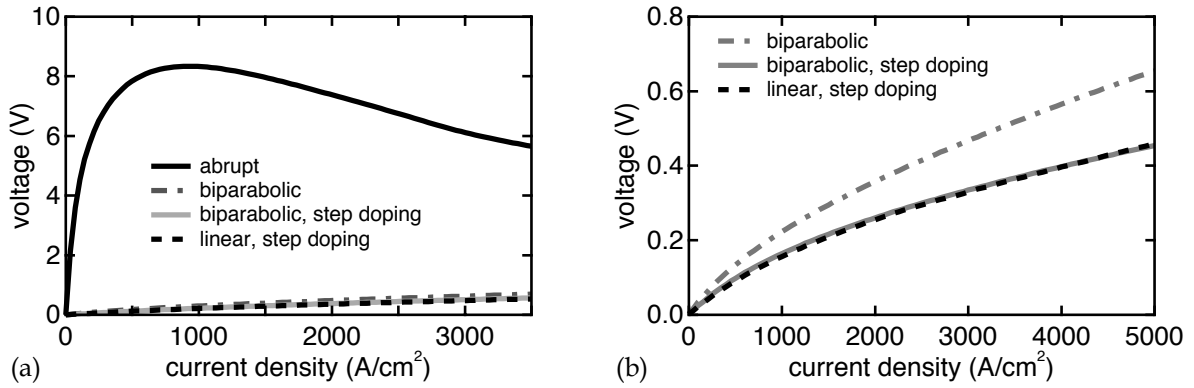


Figure 7.7 IV-curves of the improved p-DBRs. (a) Comparison of the p-DBR with no grading (abrupt) and the p-DBRs with a digital alloy grading. (b) Comparison of the three p-DBRs with a digital alloy grading.

Figure 7.7(b) shows a direct comparison of the three p-DBRs with the digital alloy grading. The device with the bi-parabolic grading without the step doping shows a voltage drop of around 0.52 V at a current density of 3.5 kA/cm². Using step doping in combination with the linear or bi-parabolic grading further reduces the voltage drop to 0.38 V. Note that the average doping level in the linear grading with step doping is higher than in the bi-parabolic grading with step doping.

Although the voltage drop is significantly lower using a digital alloy molefraction grading instead of abrupt interfaces, the IV-curves are not yet a perfectly straight line, meaning that a small voltage drop still occurs at the interfaces. The resistance and the differential resistance for the 15-pair p-DBRs with the different digital alloy gradings are given in Table 7.2 for a current density of 5 kA/cm².

A direct comparison with the stepped compositional grading p-DBR employed in our initial EP-VECSEL design was unfortunately not possible, since the correct growth rates and doping levels for the intermediate $\text{Al}_{(x)}\text{Ga}_{(1-x)}\text{As}$ steps were not calibrated at that time. Therefore, this type of p-DBR could not be grown on a p-doped substrate, which is the prerequisite for the improved measurement technique. Nevertheless, in comparison to typical values found in literature, our p-DBRs exhibit very similar resistance values [72].

label	resistance ($\mu\Omega\cdot\text{cm}^2$)	diff. resistance ($\mu\Omega\cdot\text{cm}^2$)
bi-parabolic	133	85
bi-parabolic, step doping	94	52
linear, step doping	95	53

Table 7.2: Resistance and differential resistance of the 15-pair p-DBRs with the digital alloy grading at a current density of 5 kA/cm².

Besides the electrical behavior, the optical losses in the p-DBR are also of great interest. The largest contribution comes from doping and the associated FCA losses. Therefore, the p-DBR with the bi-parabolic digital alloy grading and step doping is expected to have lower losses than the linearly graded p-DBR with step doping, since the doping levels in the linear grading are much higher. Although the electrical performance of the linearly graded and the bi-parabolically graded p-DBR with step doping are similar, the expected lower optical losses of the bi-parabolic p-DBR make this design the better choice for an EP-VECSEL gain chip.

7.1.5 Further possible improvements

Even though the performance of the bi-parabolic digital alloy p-DBR with step doping is already comparable to state-of-the-art literature values, a few design parameters can still be optimized further. Especially the doping levels in the grading can be further improved for low electrical and optical losses. Doping schemes like modulation doping [63, 72] could also be investigated and a detailed numerical analysis using our simulation tool should give further insight into possible optimization methods.

7.2 Improvement of the thermal management

Another way to overcome the thermal limitations of our initial design is the improvement of the thermal management of the EP-VECSELs. Using our numerical model we have simulated the spatial heat distribution in the devices. Figure 7.8(a) shows the device-internal temperature-increase as a function of the distance from the device center for an 80- μm BCD device with a 300- μm diameter top contact and a device radius of 200 μm (solid black line). Increasing the device radius (solid dark gray: 250 μm , solid light gray: 300 μm) and thus the heat transfer area of the devices reduces the temperature increase in the center of the device significantly. Figure 7.8(b) shows the resulting temperature increase (dashed lines) in the active region and the output power (solid lines) as a function of the injected current and the device radius. Increasing the radius from 200 μm to 300 μm allows an increase of the injected current by nearly 50% while maintaining an active-region temperature of 75°C. This results in an increase of the output power by nearly 70% from about 65 mW to about 110 mW. This correlation shows that a significant amount of heat is dissipated laterally into the device before being transferred to the heatsink.

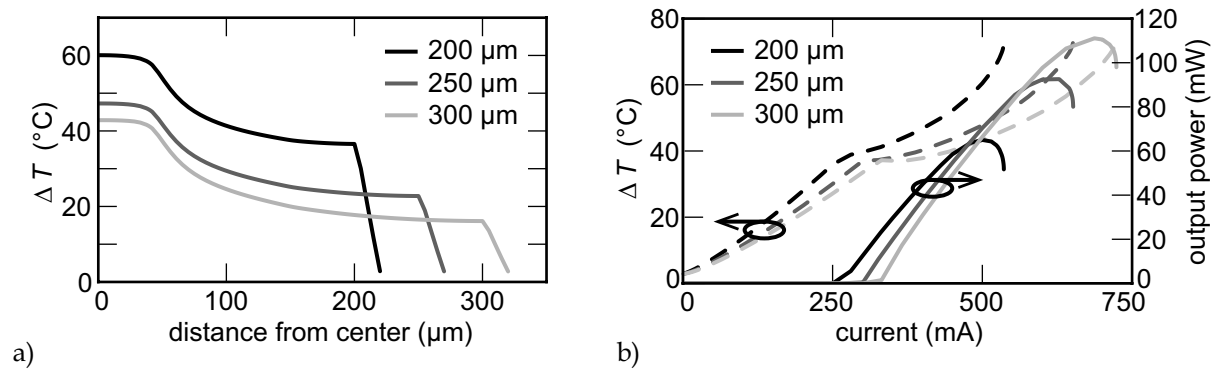


Figure 7.8 Device-internal temperature and output power as a function of the device size for an 80- μm BCD device with a 300- μm diameter top contact. (a) Spatial heat distribution in the device as a function of the device radius. (b) Temperature increase in the active region and output power as a function of injected current and device size.

The increase in output power by scaling the heat transfer area was considered in a new photolithography maskset, making the individual devices larger and symmetric. Figure 7.9 shows an 80- μm BCD device on the old maskset (Figure 7.9(a)) and on the new maskset (Figure 7.9(b)).

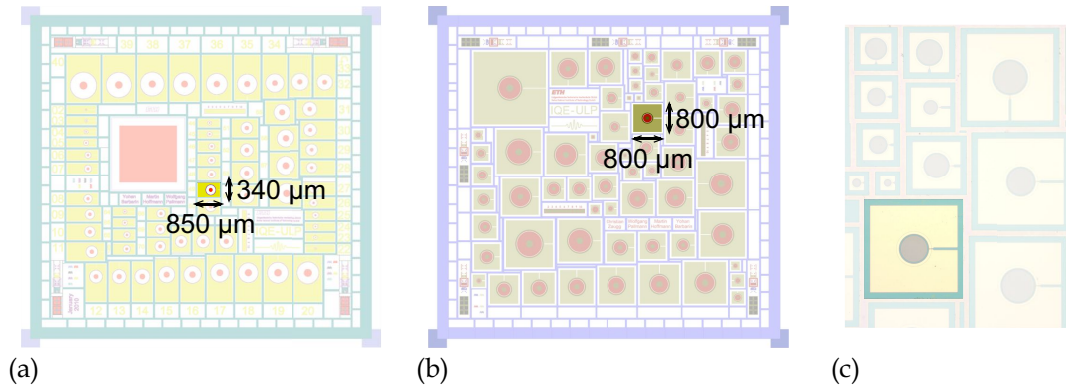


Figure 7.9 Improvement of the thermal management of the EP-VECSELs by using a new maskset. (a) 80- μm BCD device on the old maskset. The device has a reduced heat transfer area and is asymmetric. (b) 80- μm BCD device on the new maskset. The device is symmetric and has a more than two times higher heat transfer area. (c) Image of a realized 80- μm BCD EP-VECSEL using the new maskset.

The device size and thus the heat transfer area on the new maskset is more than twice as large for better heat removal. Furthermore, the device geometry is now symmetric. Asymmetric devices might lead to beam distortions due to different thermal lensing effects in the two axes. Figure 7.9(c) shows a photographic image of a realized 80- μm BCD device using the new maskset. The expected improvements from this adapted maskset are the following:

- more efficient heat removal in the lateral direction;
- increased modal gain of the devices due to the temperature reduction;
- symmetric beam profile due to symmetric heat profile.

All this together should lead to higher power in the fundamental TEM_{00} transversal-mode. Furthermore, we have also designed and implemented a new heat sink with a higher cooling capacity that allows us to cool the EP-VECSEL gain chip down to -21°C . Reducing the temperature of the heat sink allows to inject higher currents into the devices before the thermal rollover occurs and should also help to increase the fundamental transversal-mode output power of the EP-VECSELs.

7.3 Beam quality optimization

The second limitation of our initial EP-VECSEL realization besides the thermal issues was the insufficient beam quality. Fundamental TEM_{00} -mode operation was only achieved at significantly reduced output power levels using an intra-cavity aperture (see Chapter 5). Several higher order transverse modes normally destabilize modelocking because of axial mode beating noise at different frequencies (see Chapter 3). In Chapter 6 the influence of the intermediate n-DBR reflectivity on the output power and the beam quality was discussed. Based on these finding we have optimized the internal reflectivity of our EP-VECSELs. Table 7.3 gives a comparison of the n-DBR reflectivity and the resulting field enhancement of the initial and the improved EP-VECSEL design. The improved design features 9 n-DBR pairs (previously: 11) using the $Al_{0.9}Ga_{0.1}As/GaAs$ material system (GaAs/AlAs). This corresponds to an n-DBR reflectivity of 81% (93%) and a resulting field enhancement of 25 (60). The reduced reflectivity should enable fundamental transversal mode operation.

design	material system	n-DBR pairs	internal reflectivity	field enhancement
initial	AlAs/GaAs	11	93%	60
improved	$Al_{0.9}Ga_{0.1}As/GaAs$	9	81%	25

Table 7.3: Comparison of the n-DBR reflectivity and the resulting field enhancement for the initial and the improved EP-VECSEL design.

7.4 Improved design

In this section, an overview of the improved design will be presented. Figure 7.10 shows a schematic of the improved design of the EP-VECSEL gain structure. The p-contact layer consists of 100 nm of GaAs with a doping level of $2 \cdot 10^{19} \text{ cm}^{-3}$ (previously: $3 \cdot 10^{19} \text{ cm}^{-3}$). The p-DBR exhibits 30 quarter-wave layer pairs of $\text{Al}_{0.9}\text{Ga}_{0.1}\text{As}/\text{GaAs}$.

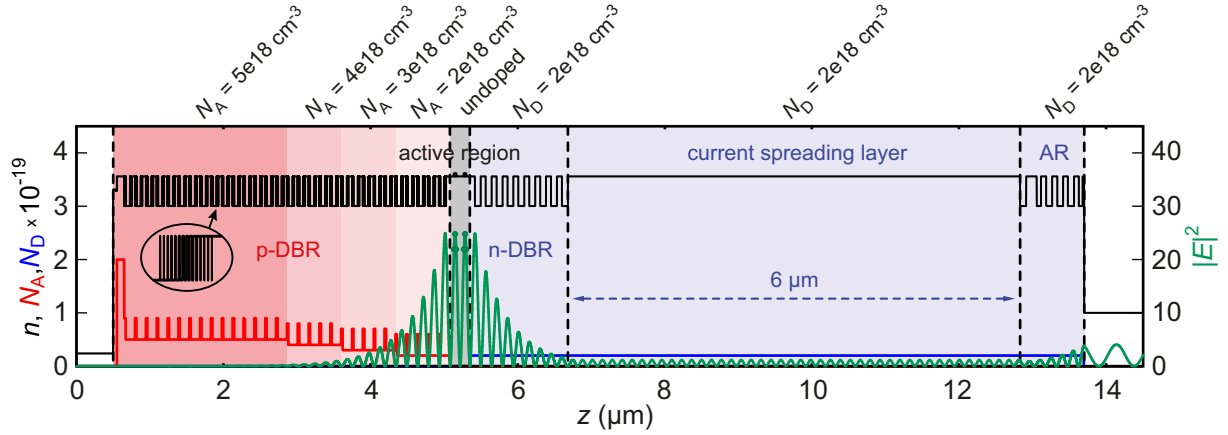


Figure 7.10 Improved design of the EP-VECSEL gain structure. The black lines represent the refractive index profile, the green lines the squared electric field, the red and blue lines the p- and n-doping, respectively. The absolute bulk doping values are also given on top. The inset shows a detailed view of the digital alloy grading in the p-DBR. The QWs are placed in the antinode of the standing wave pattern, indicated by a green dot.

The $\text{Al}_{0.9}\text{Ga}_{0.1}\text{As}/\text{GaAs}$ material system should have a lower electrical resistance than the previously used AlAs/GaAs material system due to the smaller band offset at the hetero-interfaces between the materials [24]. To further reduce the energy-band discontinuities at the material interfaces, we employ a digital alloy bi-parabolic grading (see Section 7.1.2), as shown in the inset in Figure 7.10. Furthermore, we apply an optimized bulk doping profile for low optical and electrical losses just like in the initial design by increasing doping levels in the structure where the electric field (shown in green in Figure 7.10) is low. Near the active region, where the electric field is the highest, the lowest doping levels are used. At the material interfaces in the p-DBR where the electric field has a node, we additionally increase the p-doping level by $4 \cdot 10^{18} \text{ cm}^{-3}$ (step doping, shown in red in Figure 7.10). The undoped active region consists of $2 \times 3 \text{ In}_{(x)}\text{Ga}_{(1-x)}\text{As}$ QWs embedded in GaAs, positioned in two adjacent antinodes of the standing wave pattern, just as in the initial realization. The

PL at room temperature is detuned by 20 nm (previously: 25 nm) from the design wavelength of 960 nm to ensure maximum gain at high current injection and thus high temperature. The intermediate n-DBR has 9 pairs (previously: 11) and is n-doped at a doping level of $2 \cdot 10^{18} \text{ cm}^{-3}$. The CSL is unchanged and consists of a 6- μm -thick GaAs layer at a doping level of $2 \cdot 10^{18} \text{ cm}^{-3}$. The structure is completed by a 12-layer (previously: 14-layer) semiconductor AR-coating to reduce sub-cavity effects from the CSL. The AR-coating is now also n-doped at a doping level of $2 \cdot 10^{18} \text{ cm}^{-3}$ to facilitate processing (see Chapter 4). We determined the n-doping level of $2 \cdot 10^{18} \text{ cm}^{-3}$ to be sufficient for an ohmic contact with low electrical resistance. Therefore, the n-contact layer does not need to be separately implemented anymore.

Chapter 8

Experimental results of the improved design

Based on the improved design described in the previous chapter, we fabricated a new EP-VECSEL gain chip with 63 geometrically different lasers using the new maskset. In this chapter the experimental characterization of the improved lasers is presented. In the first section, the electrical characterization of the devices is described. Then, cw measurements of the different lasers and the beam quality of EP-VECSELs with different BCD are presented. In the following section, passive modelocking experiments using the EP-VECSEL gain chip and the obtained results are described. At the end of this chapter, limitations of the modelocking performance and further optimization possibilities are discussed. The results presented in this chapter have been partly published in [77].

Figure 8.1(a) shows an image of the improved EP-VECSEL gain chip on a one-inch CuW wafer with the 63 different lasers. In comparison to the initial maskset (see Chapter 5), the gain chip has fewer lasers now but the individual devices are much larger for better heat transfer (see Chapter 7). Figure 8.1(b) contains a magnified image of a laser with a BCD of $90\text{ }\mu\text{m}$ and a top contact opening of $324\text{ }\mu\text{m}$. The device itself is $630\text{ }\mu\text{m} \times 630\text{ }\mu\text{m}$.

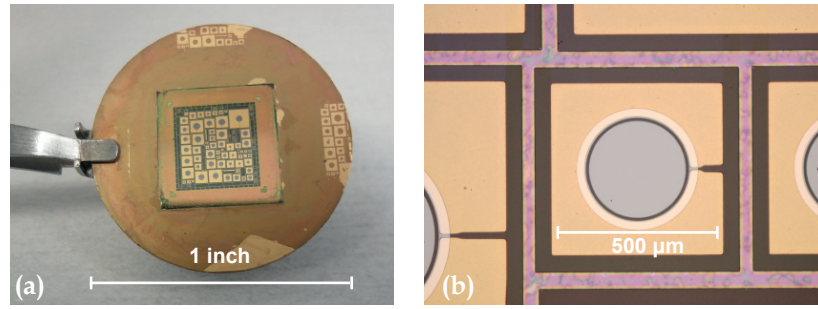


Figure 8.1 Images of the improved EP-VECSEL gain chip using the new maskset. (a) One-inch CuW wafer with 63 geometrically different lasers and (b) magnified image of a device with a BCD of 90 μm and a top contact opening of 324 μm . The structure height is around 13.2 μm .

8.1 Electrical characterization

Like for the evaluation of our initial design, we chose the lasing threshold current I_{th} and the differential resistance at lasing threshold dR_{th} as the two parameters to electrically compare the different devices on the improved EP-VECSEL gain chip. In Figure 8.2 these parameters are plotted as a function of the BCD.

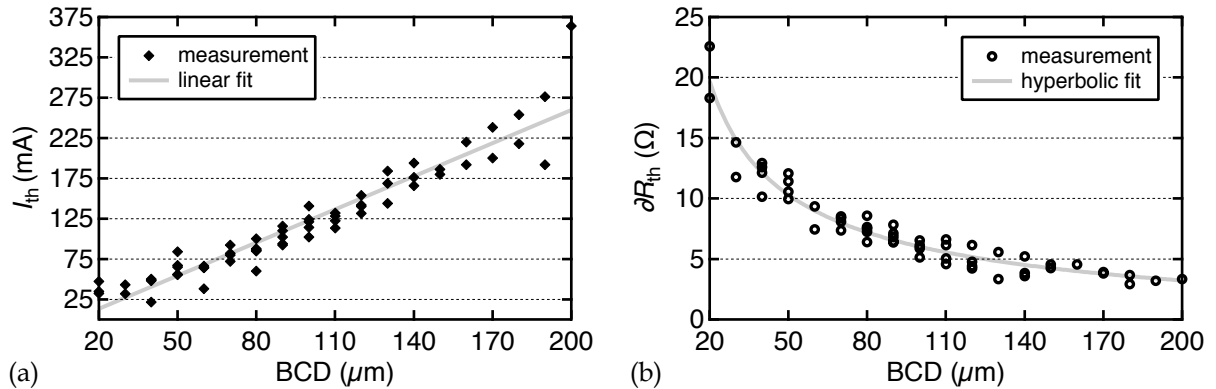


Figure 8.2 (a) Lasing threshold current and (b) differential resistance at lasing threshold as a function of the BCD. The threshold current increases linearly with the BCD, only the largest device shows a significantly higher threshold. The differential resistance at threshold shows a hyperbolic behavior.

The lasing threshold current in Figure 8.2(a) shows a linear increase with the BCD, whereas the differential resistance at lasing threshold in Figure 8.2(b) decreases hyperbolically with the BCD (see Chapter 5). In direct comparison with the initial design (see Chapter 5), the values of I_{th} for a given BCD are much lower for the optimized design. As an example, I_{th} is reduced from around 200 mA (initial design) to around 85 mA (optimized design) for an 80- μm BCD laser. This is mainly due to

the reduced detuning of the emission wavelength of the QWs from the cavity resonance. On the other hand the values of ∂R_{th} for a given size are higher. This can again be explained by the reduced detuning, since the device-internal temperature at higher currents is higher, reducing the differential resistance. It becomes clear, that a direct comparison between the two designs is difficult. Many parameters like the detuning, doping levels, p-DBR design, material system, doping of the AR-coating, device geometry or number of n-DBR pairs have been modified and all influence the performance. The figure of merit to compare the overall performance is the output power.

8.2 Continuous wave characterization

To evaluate the lasing performance of the optimized EP-VECSEL gain chip, the multi-mode performance and powerscaling properties were characterized first. They will be presented in the next section. Subsequently, the beam quality and single-mode performance of the devices will be presented. This is an essential prerequisite for passive modelocking experiments.

8.2.1 Multi-mode performance and powerscaling

The multi-mode cw characterization was performed using the test setup described in Chapter 5 using a straight laser cavity consisting of the EP-VECSEL gain chip and a curved OC.

Highest output power

Figure 8.3 shows an LIV-curve of the largest EP-VECSEL with a BCD of 200 μm . With an OC transmission of 5.5% and a heatsink temperature of -20°C , nearly 170 mW of multi-mode cw output power are generated at an injected current of 984 mA.

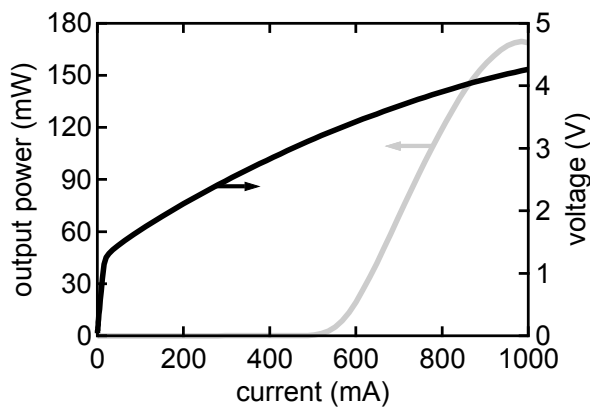


Figure 8.3 LIV-curve of the largest EP-VECSEL with a BCD of 200 μm . Nearly 170 mW of multi-mode cw output power are obtained. The heatsink temperature was -20°C and the OC transmission 5.5%.

Influence of the temperature

The influence of the heatsink temperature on the multi-mode cw LIV-curve of a 100- μm BCD EP-VECSEL is shown in Figure 8.4. The voltage drop increases with decreasing temperature (Figure 8.4(a)), as expected from the semiconductor material. The output power also increases with decreasing temperature. A decrease in heatsink temperature increases the detuning between QW-emission-wavelength and cavity resonance. Therefore, more current can be injected into the device before the thermal rollover occurs. The shift of the thermal rollover to higher currents with lower heatsink temperature can be clearly seen in Figure 8.4(b).

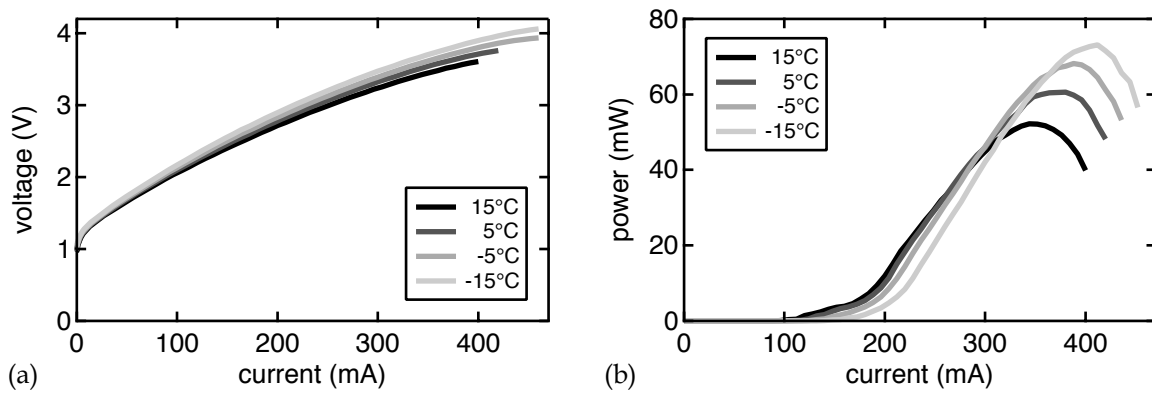


Figure 8.4 (a) IV-curves and (b) multi-mode LI-curves as a function of temperature for an EP-VECSEL with a BCD of 100 μm . The voltage drop, but also the output power, increase with decreasing temperature. The used OC had a transmission of 5.5%.

Influence of the OC transmission

Figure 8.5 shows the influence of the OC transmission on the multi-mode cw output power of a 100- μm BCD EP-VECSEL at a heatsink temperature of 3°C.

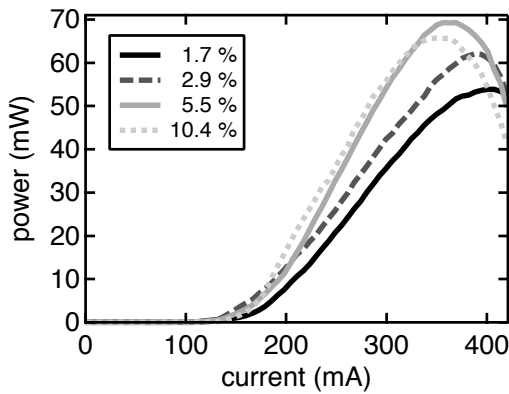


Figure 8.5 Multi-mode LI-curves of an EP-VECSEL with a BCD of 100 μm for different OC transmissions. The heatsink temperature was 3°C.

The output power first increases with higher OC transmission, the optimum is then found at 5.5%. In the measured range of values the influence of the OC transmission on the output power is not very strong. At an OC transmission of 1.7%, 54 mW are obtained, whereas for an OC transmission of 5.5%, 69 mW are generated.

Optical spectral properties

In Figure 8.6(a) a typical optical multi-mode spectrum of a 100- μm BCD EP-VECSEL is plotted for a heatsink temperature of -15°C and an injected current of 330 mA. The optical spectrum as function of the injected current is plotted in Figure 8.6(b). Like previously seen in Chapter 5, the device exhibits a redshift and broadening of the optical spectrum for increasing injected electric currents. The higher bandwidth of the less resonant structure leads to lasing operation in a larger spectral window than for the more resonant initial design.

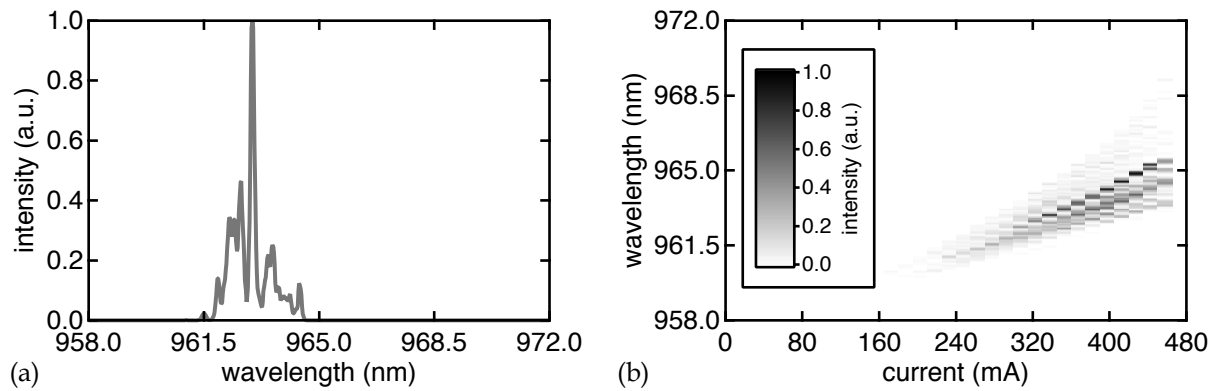


Figure 8.6 (a) Optical multi-mode spectrum of a 100- μm BCD device at a heatsink temperature of -15°C and a pump current of 330 mA. (b) Shift of the optical spectrum as a function of the injected current.

Powerscaling

To investigate the powerscaling characteristics as a function of the BCD, an LIV-curve was recorded for each laser at a heatsink temperature of 3°C using an OC with a transmission of 5.5%. Figure 8.7(a) shows the maximum output power as a function of the BCD. The values are scattered, but an increase with the BCD is clearly visible. The scattered distribution is most likely due to non-uniform defect density and processing of the chip. Especially the high roughness of the used CuW wafers may have a strong influence. The maximum value of the output power at this heatsink temperature is 125 mW.

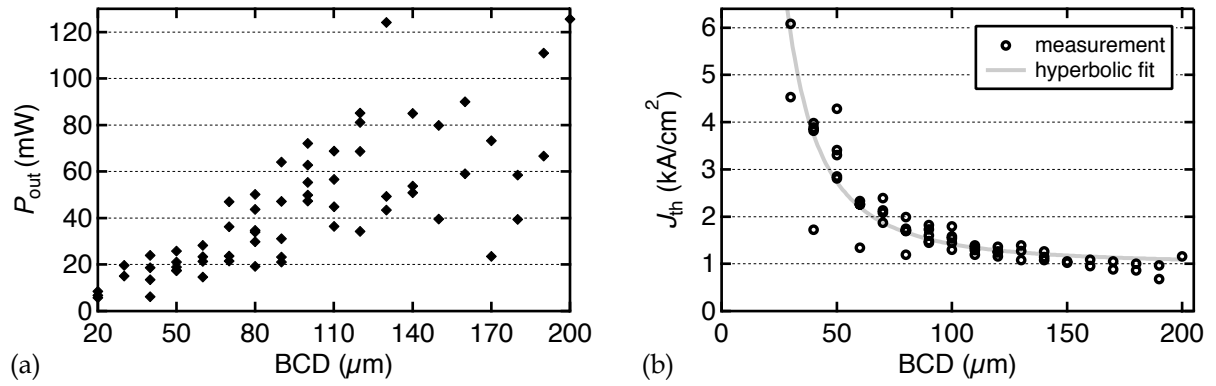


Figure 8.7 (a) Output power and (b) threshold current density as a function of the BCD. The heatsink temperature was stabilized at 3°C , the OC transmission had a value of 5.5%. The output power values are scattered, but an increase with the BCD is clearly visible. The threshold current density shows a hyperbolic behavior.

Figure 8.7(b) shows the dependence of the threshold current density on the BCD. A hyperbolic decrease can be observed towards larger devices. Table 8.1 shows a direct comparison of the cw multi-mode performance of the initial and the improved EP-VECSEL design.

parameter	initial design	optimized design
P_{max} (mW) (cw, multi-mode)	120 mW	125 mW
BCD	180 μm	200 μm
T_{heatsink}	2°C	3°C
$R_{\text{n-DBR}} / I$	93% / 60	81% / 25

Table 8.1: Comparison of the cw multi-mode performance of the initial and the improved design.

Given are the maximum achievable output power and the corresponding heatsink temperature and device size. A slightly higher output power level is achieved with the new design, even though the field enhancement in the active region is only 25 instead of 60. The field enhancement is proportional to the gain (see Chapter 2). This means that the gain penalty associated with the reduction of n-DBR pairs is compensated by the optimization of the device design and should allow for single-mode operation with high output power levels.

8.2.2 Beam quality and single-mode performance

Table 8.2 shows beam quality measurements of differently sized EP-VECSELs. The measurements were carried out in a Z-shaped cavity similar to the one later used for the passive modelocking experiments. Instead of a SESAM a DBR was used. The OC had a ROC of 40 mm and an optimized transmission of 1.1% in this configuration. The heatsink was kept constant at 2°C. For each device, the cavity was optimized for maximum output power with the lowest achievable M^2 -value. As a reference, the cw multi-mode output power from Figure 8.7(a) is also given.

BCD (μm)	output power (mW)	beam quality (M^2 value)	multi-mode power (mW)
70	26	1.0	47
90	33	1.6	64
100	31 / 47	1.6 / 2.5	63
120	26	1.5	85

Table 8.2: Beam quality measurements as a function of the BCD measured in a Z-shaped cavity at a heatsink temperature of 2°C with an OC transmission of 1.1%. As a reference the multi-mode output power in a straight cavity at 3°C and an OC transmission of 5.5% is also given.

For a 70- μm BCD EP-VECSEL, up to 26 mW with excellent beam quality ($M^2 = 1.0$) were achieved. For larger devices the output power still increases slightly, but the beam quality is already reduced. At the same time, the output power ratio compared to the cw multi-mode measurements drops for larger EP-VECSELs. Consequently, the device with a 70 μm BCD was chosen for the modelocking experiments.

8.3 Passive modelocking experiments

In this section, the passive modelocking experiments using the optimized EP-VECSEL gain chip are presented. First the experimental setup and the cavity are described, then the achieved passive modelocking results are presented.

8.3.1 Experimental setup

Figure 8.8 shows the experimental setup for the passive modelocking experiments. A Z-shaped cavity was used to match the resonator mode with the pumped area of the 70- μm BCD device and to focus onto the SESAM. This is necessary to ensure that the losses saturate before the gain, enabling stable modelocked operation (see Chapter 3). The ROC of the OC was 60 mm; the folding mirror had a ROC of 20 mm. This resulted in a mode size radius of around 35 μm on the EP-VECSEL and 20 μm on the SESAM. Both the SESAM and the EP-VECSEL gain chip were mounted on a Peltier-cooled copper heatsink for temperature stabilization and tuning.

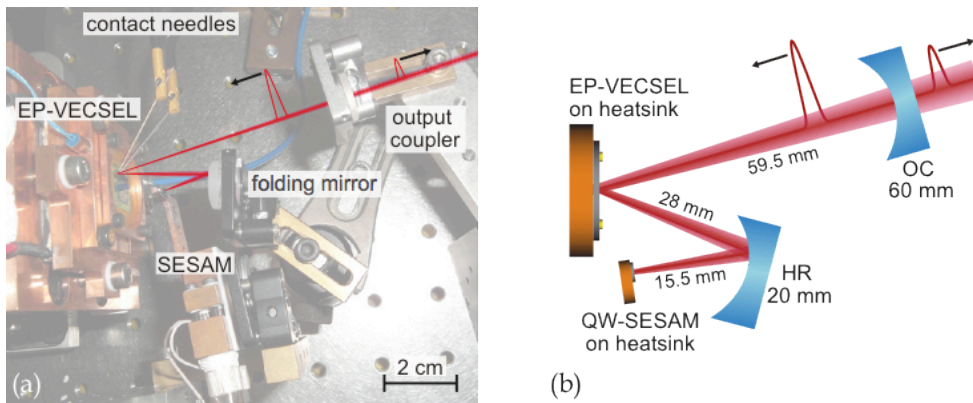


Figure 8.8 Experimental setup for the modelocking experiments. (a) Picture of the Z-shaped laser cavity with the SESAM, folding mirror, EP-VECSEL gain chip and the curved OC. The chip is contacted with two probe needles. (b) Schematic containing details of the cavity.

The SESAM is based on a single AlAs-embedded $\text{In}_x\text{Ga}_{(1-x)}\text{As}$ QW and a 4-pair semiconductor AR-coating with a layer of FS on top. The measured saturation fluence of the SESAM (see Chapter 3 for the measurement method and setup) was 16.5 $\mu\text{J}/\text{cm}^2$ and the modulation depth 0.84% for a wavelength of 963.1 nm and a heatsink temperature of 35.5°C, as later used in the experiment. For a second experiment, a similar SESAM was used with a SiN_x -layer on top. This resulted in a measured saturation fluence of 16.2 $\mu\text{J}/\text{cm}^2$ and a modulation depth of 0.69% for a wavelength of 963.1 nm and a heatsink temperature of 26°C.

8.3.2 Experimental results

Using the SESAM with the SiNx top-coating, stable modelocked operation was achieved at a pump current of 259 mA and a heatsink temperature of -21°C . The OC transmission was 0.5%. The SESAM was temperature-stabilized at 26°C to shift the absorption to a longer wavelength. The average (peak) output power was 6.2 mW (0.6 W). Figure 8.9(a) shows the measured second harmonic generation (SHG) intensity autocorrelation and the sech^2 -fit of a 6.3-ps pulse.

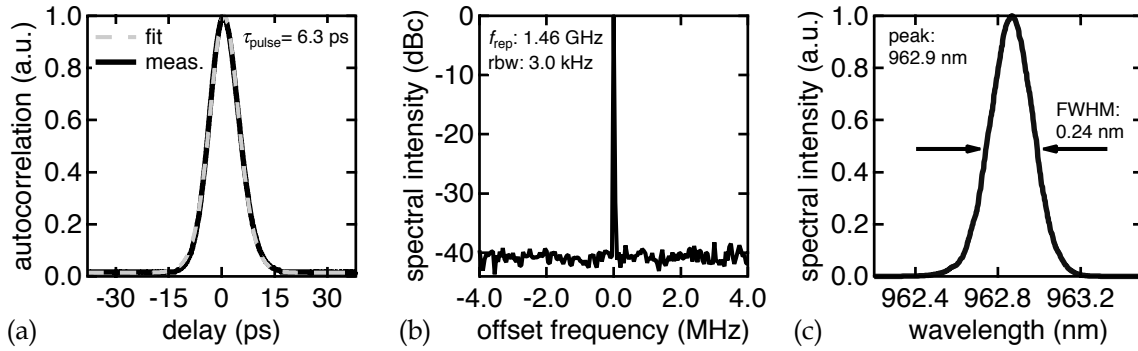


Figure 8.9 Passive modelocking results. (a) Second harmonic generation intensity autocorrelation, (b) microwave spectrum, and (c) optical spectrum of the 6.3-ps pulses at 1.46 GHz pulse repetition rate and 6.2 mW of average output power. rbw: resolution bandwidth, f_{rep} : repetition frequency.

The microwave spectrum in Figure 8.9(b) is measured with a resolution bandwidth of 3.0 kHz and shows a span of 8 MHz around the fundamental repetition rate of 1.46 GHz. The optical spectrum in Figure 8.9(c) is centered at a wavelength of 962.9 nm and has a spectral width of 0.24 nm FWHM. The resulting TBP is $\Delta\nu\Delta\tau = 0.5$, corresponding to about 1.56 times a transform-limited sech^2 -pulse.

In a similar cavity configuration with the FS-coated SESAM, we obtained 13.1 mW (1.1 W) of average (peak) output power with slightly longer pulse duration of 7.3 ps at the same repetition rate of 1.46 GHz. The optical spectrum shows a FWHM of 0.24 nm at 962.9 nm, resulting in a TBP of 0.56, roughly 1.7 times the transform limit. The injected current was 266 mA, and the EP-VECSEL and SESAM temperature were -20.7°C and 35.5°C , respectively. The OC transmission had a value of 0.85%.

8.4 Limitations and outlook

The experimental results presented in the previous section represent an important milestone, since they verify our design guidelines of an EP-VECSEL optimized for passive modelocking. Although the obtained pulse duration is already very close to the calculated minimum (see Chapter 2), the average output power still needs to be increased to make passively modelocked EP-VECSELs attractive for industrial applications. In this section, the performance limitations in modelocked operation are discussed and an outlook on possible improvements for higher average output power is given.

8.4.1 *Performance limitations of the modelocked EP-VECSELs*

Obtaining even shorter pulse durations from an EP-VECSEL is challenging. On the one hand, the gain bandwidth of these resonant structures is large enough to support significantly shorter pulses (see Chapter 6). On the other hand, the structural resonance leads to strongly wavelength dependent GDD values in the order of several 10^4 fs² around the resonance, setting a lower limit for the theoretically possible pulse duration (see Chapter 2). For both modelocking results presented in the previous section, the pulses exhibit a chirp with a TBP between 1.5 – 1.7 times the transform limit, most likely related to these very high GDD values. One possibility to reduce the pulse duration would be to reduce the number of intermediate n-DBR pairs further, but this would also decrease the gain and consequently lead to a reduction in average output power.

To scale the average output power, a simple approach would be to scale the pumped area. However, Table 8.2 shows that for larger devices the single-mode output power does not necessarily scale with the pumped area. Therefore, the optimization must focus on the increase of the single-mode output power from small lasers. Some approaches to achieve this are discussed in the next section.

8.4.2 *Possible improvements for higher average output power*

Reduction of optical losses and electrical resistance

A reduction of optical losses in the structure can be achieved by decreasing average doping levels and consequently optical losses from FCA. This requires a reduction of the electrical resistance of the devices at the same time to avoid excessive heating

from ohmic losses leading to a thermal rollover at low injected currents. Some possibilities that should allow for a reduction of the electrical resistance are:

- further improvement of the p-DBR, for example by optimizing doping levels in the gradings or using modulation doping schemes (see Chapter 7);
- a molefraction grading similar to the one used in the p-DBR can also be implemented in the n-DBR and the AR-coating;
- etching of the AR coating down to the CSL below the n-contact as it has been previously done;
- improvement of the active region. A graded index separate confinement hetero-structure (GRIN-SCH)-type active region [78] has already been developed for VCSELs and exhibits a lower resistance while increasing carrier confinement in the active region at the same time;

Improved current confinement

Another way of increasing the single-mode performance of the EP-VECSELs is to improve the current confinement by reducing current leakage and enhancing the current injection into the center of the device. Some options for an improved current confinement are:

- etching of trenches into the p-DBR , as it was proposed and simulated in [79].
- proton implantation into the p-DBR [80].
- use of an oxide-aperture in the active region, as it is commonly done in VCSELs [76].

All these possibilities require additional processing steps, but should help to increase the single-mode output power of the EP-VECSELs.

Further improved thermal management

The thermal management of the EP-VECSEL gain chip has already been enhanced by increasing the heat transfer area of the individual devices (see Chapter 7), but it can be further optimized. Especially the thermal conductivity of the heatsink leaves room

for improvement. Figure 8.10 shows the influence of the heatsink material on the output power of an 80- μm -BCD EP-VECSEL.

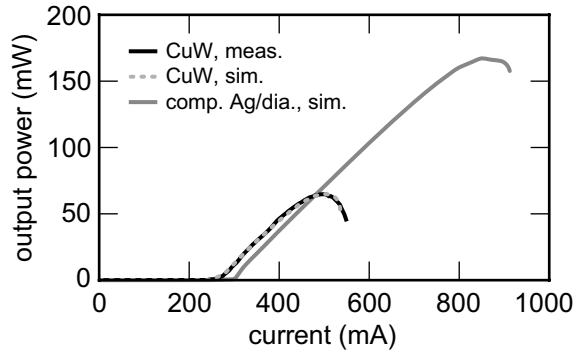


Figure 8.11 Simulated influence of the heatsink material on the output power of an 80- μm BCD EP-VECSEL. Black: measured, on CuW. Dashed gray: simulated, on CuW. Dark gray: simulated, on composite silver (Ag)/diamond.

The solid black line shows the measured LI-curve of the device on a CuW heatsink with a thermal conductivity of around $200 \text{ W}\cdot\text{K}^{-1}\cdot\text{m}^{-1}$. The dashed light gray line is the fit to this data using our simulation model. For the solid dark gray line, the same simulation data was taken, except the thermal conductivity was adapted to that of composite silver/diamond with $650 \text{ W}\cdot\text{K}^{-1}\cdot\text{m}^{-1}$. This leads to an increase in output power from 65 mW to nearly 170 mW, corresponding to an increase of more than 160%. Furthermore, composite diamond heatsink materials like silver/diamond or copper/diamond (thermal conductivity: $550 \text{ W}\cdot\text{K}^{-1}\cdot\text{m}^{-1}$, see Chapter 4) have a CTE matched to GaAs and are consequently a highly interesting alternative for the next realization of an EP-VECSEL gain chip.

Chapter 9

Conclusion and outlook

Electrical pumping is a key factor for more compact and cost efficient ultrafast VECSELs. In this thesis, the design, realization and improvement of an EP-VECSEL optimized for passive modelocking have been presented.

In our first successful realization of an EP-VECSEL, we experimentally verified our design guidelines based on numerical simulations and demonstrated confined current injection profiles for devices up to a bottom contact diameter of 100 μm . In cw multi-mode operation up to 120 mW of output power were obtained. However, the two main limitations of this initial design that we identified were thermal issues and insufficient beam quality. Fundamental transversal-mode operation was not achieved, which is an important prerequisite for stable passively modelocked operation. To find the reason for this, a more thorough investigation of the EP-VECSEL device characteristics was necessary.

The EP-VECSEL gain structure exhibits a resonant subcavity between the bottom DBR and an intermediate DBR, increasing the field enhancement and thus the gain in the active region. This is necessary to compensate losses from free carrier absorption due to doping of the structure. To gain deeper insight how the resonance affects the beam quality of the devices, EP-VECSELs with different intermediate DBR reflectivity were characterized. The experimental study revealed that devices with a high intermediate DBR reflectivity can suffer from low beam quality. It became clear, that a trade-off between high output power and good beam quality needs to be accepted in the design of an EP-VECSEL. This finding helped us to determine design

guidelines for our own future designs to achieve good beam quality with reasonable output power.

In addition to a better insight on the beam quality of these devices, a detailed characterization of important gain properties as function of the resonance broadened the understanding of these devices. Good knowledge of the gain properties is important for designing modelocking experiments and numerical modeling of the devices. From spectral gain measurements, gain bandwidth and small-signal gain were extracted. Gain saturation measurements revealed typical values for the saturation fluence, small-signal gain, non-saturable losses and induced absorption effects of EP-VECSEL gain chips. The device with the lowest field enhancement provides up to 3.1 nm of gain bandwidth full-width at half-maximum together with a moderate saturation fluence of $6.2 \mu\text{J}/\text{cm}^2$, making this device highly interesting for modelocking experiments.

Semiconductor lasers exhibit dynamic gain saturation, which means that for stable modelocked operation the absorber needs to saturate faster than the gain. The measurement of the gain saturation fluence allowed us to select a suitable SESAM with the correct saturation parameters. Passive modelocking experiments using the EP-VECSEL with the lowest field enhancement resulted in pulses as short as 9.5 ps with an average output power of 7.6 mW at a repetition rate of 1.4 GHz. This was an important step demonstrating that an EP-VECSEL with an optimized intermediate DBR reflectivity is suitable for ultrashort pulse generation.

The design guidelines we identified for achieving excellent beam quality were taken into account for an improved design. Furthermore, different aspects of the EP-VECSEL design were optimized to alleviate the thermal limitations. On the one hand, the electrical properties of the bottom p-doped DBR were optimized, with the aim to reduce Joule-heating of the devices due to ohmic losses. This required an improvement of the p-DBR measurement test structure, which previously delivered irreproducible results due to non-uniform current flow. A digital-alloy bi-parabolic p-DBR was subsequently developed, delivering state-of-the-art electrical performance. On the other hand, the thermal management of the EP-VECSELs was improved. Using an optimized device geometry derived from numerical simulations, a new photolithography mask-set was developed, increasing the heat-transfer area of the individual devices.

Based on these optimizations, an improved EP-VECSEL gain chip was fabricated. In cw multi-mode operation, up to 170 mW of output power were obtained. Overcoming previous limitations, single-mode operation was achieved at 26 mW of output power. In passive modelocking experiments with the improved EP-VECSELS, 7.3-ps pulses with 13.1 mW (1.1 W) of average (peak) output power and 6.3-ps pulses with 6.2 mW of average output power, both at 1.46 GHz repetition rate, were obtained. These are to the best of our knowledge the shortest pulses with the highest peak power from an EP-VECSEL to date.

Reducing electrical and optical losses further and enhancing the current confinement of the devices will increase the single-mode performance. Some possibilities to accomplish this include an optimization of the active region, molefraction gradings in the n-doped part of the structure or different structuring methods for guiding the electrical current in the devices. Further improvement of the thermal management of the EP-VECSEL gain chips should yield a significantly higher average output power level. This can be achieved by employing a composite diamond heatsink, combining high thermal conductivity and a coefficient of thermal expansion matched to GaAs. This will lead to compact, cost-efficient ultrafast laser sources with high power levels and GHz repetition rates suitable for low-cost mass applications such as optical clock-rate distribution in microprocessors, chip-to-chip interconnects or optical telecommunication systems.

References

1. R. N. Hall, G. E. Fenner, J. D. Kingsley, T. J. Soltys, and R. O. Carlson, "Coherent Light Emission From GaAs Junctions," *Physical Review Letters*, vol. 9, p. 366, 1962.
2. H. Soda, K. Iga, C. Kitahara, and Y. Suematsu, "GaInAsP/InP Surface Emitting Injection Lasers," *Japanese Journal of Applied Physics*, vol. 18, pp. 2329-2330, 1979.
3. M. Kuznetsov, F. Hakimi, R. Sprague, and A. Mooradian, "High-Power (>0.5-W CW) Diode-Pumped Vertical-External-Cavity Surface-Emitting Semiconductor Lasers with Circular TEM₀₀ Beams," *IEEE Photon. Technol. Lett.*, vol. 9, pp. 1063-65, 1997.
4. B. Rudin, A. Rutz, M. Hoffmann, D. J. H. C. Maas, A.-R. Bellancourt, E. Gini, T. Südmeyer, and U. Keller, "Highly efficient optically pumped vertical emitting semiconductor laser with more than 20-W average output power in a fundamental transverse mode," *Opt. Lett.*, vol. 33, pp. 2719-2721, 2008.
5. B. Heinen, T. L. Wang, M. Sparenberg, A. Weber, B. Kunert, J. Hader, S. W. Koch, J. V. Moloney, M. Koch, and W. Stolz, "106 W continuous-wave output power from vertical-external-cavity surface-emitting laser," *Electronics Letters*, vol. 48, pp. 516-517, 2012.
6. M. Kuznetsov, F. Hakimi, R. Sprague, and A. Mooradian, "Design and Characteristics of High-Power (>0.5-W CW) Diode-Pumped Vertical-External-Cavity Surface-Emitting Semiconductor Lasers with Circular TEM₀₀ Beams," *IEEE J. Sel. Top. Quantum Electron.*, vol. 5, pp. 561-573, 1999.
7. R. Häring, R. Paschotta, A. Aschwanden, E. Gini, F. Morier-Genoud, and U. Keller, "High-power passively mode-locked semiconductor lasers," *IEEE J. Quantum Electron.*, vol. 38, pp. 1268-1275, 2002.
8. U. Keller, K. J. Weingarten, F. X. Kärtner, D. Kopf, B. Braun, I. D. Jung, R. Fluck, C. Hönninger, N. Matuschek, and J. Aus der Au, "Semiconductor saturable absorber mirrors (SESAMs) for femtosecond to nanosecond pulse generation in solid-state lasers," *IEEE J. Sel. Top. Quantum Electron.*, vol. 2, pp. 435-453, 1996.
9. U. Keller and A. C. Tropper, "Passively modelocked surface-emitting semiconductor lasers," *Phys. Rep.*, vol. 429, pp. 67-120, June 2006.
10. S. Hoogland, S. Dhanjal, A. C. Tropper, S. J. Roberts, R. Häring, R. Paschotta, and U. Keller, "Passively mode-locked diode-pumped surface-emitting semiconductor laser," *IEEE Photon. Technol. Lett.*, vol. 12, pp. 1135-1138, 2000.
11. M. Scheller, T. L. Wang, B. Kunert, W. Stolz, S. W. Koch, and J. V. Moloney, "Passively modelocked VECSEL emitting 682 fs pulses with 5.1W of average output power," *Electronics Letters*, vol. 48, pp. 588-589, 2012.
12. D. J. H. C. Maas, A.-R. Bellancourt, B. Rudin, M. Golling, H. J. Unold, T. Südmeyer, and U. Keller, "Vertical integration of ultrafast semiconductor lasers," *Appl. Phys. B*, vol. 88, pp. 493-497, 2007.
13. B. Rudin, V. J. Wittwer, D. J. H. C. Maas, M. Hoffmann, O. D. Sieber, Y. Barbarin, M. Golling, T. Südmeyer, and U. Keller, "High-power MIXSEL: an integrated ultrafast semiconductor laser with 6.4 W average power," *Opt. Express*, vol. 18, pp. 27582-27588, 2010.

14. M. A. Hadley, G. C. Wilson, K. Y. Lau, and J. S. Smith, "High single-transverse-mode output from external-cavity surface-emitting laser diodes," *Applied Physics Letters*, vol. 63, pp. 1607-1609, 1993.
15. J. G. McNerney, A. Mooradian, A. Lewis, A. V. Shchegrov, E. M. Strzelecka, D. Lee, J. P. Watson, M. Liebman, G. P. Carey, B. D. Cantos, W. R. Hitchens, and D. Heald, "High-power surface emitting semiconductor laser with extended vertical compound cavity," *Electron. Lett.*, vol. 39, pp. 523-525, 2003.
16. J. G. McNerney, A. Mooradian, A. Lewis, A. V. Shchegrov, E. M. Strzelecka, D. Lee, J. P. Watson, M. K. Liebman, G. P. Carey, A. Umbrasas, C. A. Amsden, B. D. Cantos, W. R. Hitchens, D. L. Heald, V. V. Doan, and J. L. Cannon, "Novel 980-nm and 490-nm light sources using vertical cavity lasers with extended coupled cavities," in *SPIE 2003*, Brugge, Belgium, 2003, pp. 21-31.
17. K. Jasim, Q. Zhang, A. V. Nurmikko, A. Mooradian, G. Carey, W. Ha, and E. Ippen, "Passively modelocked vertical extended cavity surface emitting diode laser," *Electron. Lett.*, vol. 39, pp. 373-375, 2003.
18. K. Jasim, Q. Zhang, A. V. Nurmikko, E. Ippen, A. Mooradian, G. Carey, and W. Ha, "Picosecond pulse generation from passively modelocked vertical cavity diode laser at up to 15 GHz pulse repetition rate," *Electron. Lett.*, vol. 40, pp. 34-35, 2004.
19. J. R. Orchard, D. T. D. Childs, L. C. Lin, B. J. Stevens, D. M. Williams, and R. Hogg, "Tradeoffs in the realization of electrically pumped vertical external cavity surface emitting lasers," *IEEE J. Sel. Top. Quantum Electron.*, vol. 17, pp. 1745-1752, 2011.
20. I. Kardosh, F. Demaria, F. Rinaldi, M. C. Riedl, and R. Michalzik, "Electrically pumped frequency-doubled surface emitting lasers operating at 485 nm emission wavelength," *Electronics Letters*, vol. 44, pp. 524-525, 2008.
21. G. A. Keeler, D. K. Serkland, K. M. Geib, G. M. Peake, and A. Mar, "Electrically pumped 850-nm micromirror VECSELs," pp. 69-74, 2005.
22. M. E. Kurdi, S. Bouchoule, A. Bousseksou, I. Sagnes, A. Plais, M. Strassner, C. Symonds, A. Garnache, and J. Jacquet, "Room-temperature continuous-wave laser operation of electrically-pumped 1.55 μm VECSEL," *Electronics Letters*, vol. 40, pp. 671-672, 2004.
23. A. Harkonen, A. Bachmann, S. Arafin, K. Haring, J. Viheriäla, M. Guina, and M.-C. Amann, "2.34 μm electrically pumped VECSEL with buried tunnel junction," in *SPIE Photonics Europe*, Brussels, Belgium, 2010, pp. 772015-7.
24. P. Kreuter, B. Witzigmann, D. J. H. C. Maas, Y. Barbarin, T. Südmeyer, and U. Keller, "On the Design of Electrically-Pumped Vertical-External-Cavity Surface-Emitting Lasers," *Appl. Phys. B*, vol. 91, pp. 257-264, 2008.
25. R. Paschotta, R. Häring, U. Keller, A. Garnache, S. Hoogland, and A. C. Tropper, "Soliton-like pulse-shaping mechanism in passively mode-locked surface-emitting semiconductor lasers," *Appl. Phys. B*, vol. 75, pp. 445-451, 2002.
26. O. D. Sieber, M. Hoffmann, V. J. Wittwer, M. Mangold, M. Golling, B. W. Tilma, T. Südmeyer, and U. Keller, "Experimentally verified pulse formation model for high-power femtosecond VECSELs," *Applied Physics B*, pp. 1-13, 2013/04/27 2013.
27. G. W. Pickrell, D. A. Louderback, M. A. Fish, J. J. Hindi, H. C. Lin, M. C. Simpson, P. S. Guilfoyle, and K. L. Lear, "Compositional grading in distributed Bragg reflectors, using discrete alloys, in vertical-cavity surface-emitting lasers," *Journal of Crystal Growth*, vol. 280, pp. 54-59, 2005.

28. M. Hong, J. P. Mannaerts, J. M. Hong, R. J. Fischer, K. Tai, J. Kwo, J. M. Vandenberg, Y. H. Wang, and J. Gamelin, "A simple way to reduce series resistance in p-doped semiconductor distributed Bragg reflectors," *Journal of Crystal Growth*, vol. 111, pp. 1071-1075, 1991.
29. J. Chilwell and I. Hodgkinson, "Thin-films field-transfer matrix theory of planar multilayer waveguides and reflection from prism-loaded waveguides," *J. Opt. Soc. Am. A*, vol. 1, pp. 742-753, 1984.
30. B. Witzigmann, A. Bäcker, and S. Odermatt, "Physics and Simulation of Vertical-Cavity Surface-Emitting Lasers," *Journal of Computational and Theoretical Nanoscience*, vol. 5, pp. 1058-1071, 2008.
31. R. W. Hellwarth, "Advances in Quantum Electronics," e. J. R. Singer, Ed.: Columbia Univ. Press, New York, 1961, pp. 334-341.
32. F. J. McClung and R. W. Hellwarth, "Giant Optical Pulsations from Ruby," *J. Appl. Phys.*, vol. 33, pp. 828-829, 1962.
33. M. DiDomenico, "Small-Signal Analysis of Internal (Coupling-Type) Modulation of Lasers," *J. Appl. Phys.*, vol. 35, p. 2870, 1964.
34. L. E. Hargrove, R. L. Fork, and M. A. Pollack, "Locking of HeNe laser modes induced by synchronous intracavity modulation," *Appl. Phys. Lett.*, vol. 5, p. 4, 1964.
35. A. Yariv, "Internal Modulation in Multimode Laser Oscillators," *J. Appl. Phys.*, vol. 36, p. 388, 1965.
36. C. Hönniger, R. Paschotta, F. Morier-Genoud, M. Moser, and U. Keller, "Q-switching stability limits of continuous-wave passive mode locking," *J. Opt. Soc. Am. B*, vol. 16, pp. 46-56, January 1999.
37. S. Arahira, Y. Matsui, and Y. Ogawa, "Mode-locking at very high repetition rates more than terahertz in passively mode-locked distributed-Bragg-reflector laser diodes," *IEEE J. Quantum Electron.*, vol. 32, pp. 1211-1224, 1996.
38. U. Keller, G. W. 'tHooft, W. H. Knox, and J. E. Cunningham, "Femtosecond Pulses from a Continuously Self-Starting Passively Mode-Locked Ti:Sapphire Laser," *Opt. Lett.*, vol. 16, pp. 1022-1024, 1991.
39. T. Brabec, C. Spielmann, P. F. Curley, and F. Krausz, "Kerr lens mode locking," *Opt. Lett.*, vol. 17, pp. 1292-1294, September 15 1992.
40. U. Morgner, F. X. Kärtner, S. H. Cho, Y. Chen, H. A. Haus, J. G. Fujimoto, E. P. Ippen, V. Scheuer, G. Angelow, and T. Tschudi, "Sub-two-cycle pulses from a Kerr-lens mode-locked Ti:sapphire laser," *Opt. Lett.*, vol. 24, pp. 411-413, 1999.
41. D. H. Sutter, G. Steinmeyer, L. Gallmann, N. Matuschek, F. Morier-Genoud, U. Keller, V. Scheuer, G. Angelow, and T. Tschudi, "Semiconductor saturable-absorber mirror-assisted Kerr-lens mode-locked Ti:sapphire laser producing pulses in the two-cycle regime," *Opt. Lett.*, vol. 24, pp. 631-633, 1999.
42. R. Paschotta and U. Keller, "Passive mode locking with slow saturable absorbers," *Appl. Phys. B*, vol. 73, pp. 653-662, 2001.
43. F. X. Kärtner, I. D. Jung, and U. Keller, "Soliton Mode-Locking with Saturable Absorbers," *IEEE J. Sel. Top. Quant.*, vol. 2, pp. 540-556, September 1996.
44. A. Agnesi, A. Greborio, F. Pirzio, G. Reali, J. Aus der Au, and A. Guandalini, "40-fs Yb³⁺:CaGdAlO₄ laser pumped by a single-mode 350-mW laser diode," *Opt. Express*, vol. 20, pp. 10077-10082, 2012.

45. C. V. Shank, "Physics of Dye Lasers," *Reviews of Modern Physics*, vol. 47, pp. 649-657, 1975.
46. O. E. Martinez, R. L. Fork, and J. P. Gordon, "Theory of passively modelocked lasers for the case of a nonlinear complex propagation coefficient," *J. Opt. Soc. Am. B*, vol. 2, p. 753, 1985.
47. M. Hoffmann, O. D. Sieber, D. J. H. C. Maas, V. J. Wittwer, M. Golling, T. Südmeyer, and U. Keller, "Experimental verification of soliton-like pulse-shaping mechanisms in passively mode-locked VECSELs," *Opt. Express*, vol. 18, pp. 10143-10153, 2010.
48. U. Keller, "Recent developments in compact ultrafast lasers," *Nature*, vol. 424, pp. 831-838, 14.08. 2003.
49. G. J. Spühler, K. J. Weingarten, R. Grange, L. Krainer, M. Haiml, V. Liverini, M. Golling, S. Schon, and U. Keller, "Semiconductor saturable absorber mirror structures with low saturation fluence," *Appl. Phys. B*, vol. 81, pp. 27-32, 2005.
50. M. Haiml, R. Grange, and U. Keller, "Optical characterization of semiconductor saturable absorbers," *Appl. Phys. B*, vol. 79, pp. 331-339, August 2004 2004.
51. D. J. H. C. Maas, B. Rudin, A.-R. Bellancourt, D. Iwaniuk, S. V. Marchese, T. Südmeyer, and U. Keller, "High precision optical characterization of semiconductor saturable absorber mirrors," *Opt. Express*, vol. 16, pp. 7571-7579, 2008.
52. L. A. Coldren and S. W. Corzine, *Diode lasers and photonics integrated circuits*: Wiley, 1995.
53. E. Reichmanis and A. Novembre, "Lithographic resist materials chemistry," *Annual Review of Materials Science*, vol. 23, pp. 11-43, 1993.
54. K. Yoshida and H. Morigami, "Thermal properties of diamond/copper composite material," *Microelectronics Reliability*, vol. 44, pp. 303-308, 2004.
55. M. Faqir, T. Batten, T. Mrotzek, S. Knippscheer, L. Chalumeau, M. Massiot, M. Buchta, J. Thorpe, H. Blanck, S. Rochette, O. Vendier, and M. Kuball, "Novel packaging solutions for GaN power electronics: Silver-diamond composite packages," in *The International Conference on Compound Semiconductor Manufacturing Technology*, Portland, Oregon, USA, 2010, p. 307.
56. T. Kitano, S. Izumi, H. Minami, T. Ishikawa, K. Sato, T. Sonoda, and M. Otsubo, "Selective wet etching for highly uniform GaAs/AlGaAs heterostructure field effect transistors," *Journal of Vacuum Science & Technology B: Microelectronics and Nanometer Structures*, vol. 15, pp. 167-170, 1997.
57. X. Liu, K. Song, R. W. Davis, M. H. Hu, and C.-E. Zah, "Design and implementation of metallization structures for epi-down bonded high power semiconductor lasers," in *Electronic Components and Technology Conference, 2004. Proceedings. 54th*, 2004, pp. 798-806.
58. Y. Barbarin, M. Hoffmann, W. P. Pallmann, I. Dahhan, P. Kreuter, M. Miller, J. Baier, H. Moench, M. Golling, T. Südmeyer, B. Witzigmann, and U. Keller, "Electrically pumped vertical external cavity surface emitting lasers suitable for passive modelocking," *IEEE J. Selected Topics in Quantum Electronics*, vol. 17, pp. 1779-1786, 2011.
59. W. P. Pallmann, C. A. Zaugg, M. Mangold, V. J. Wittwer, H. Moench, S. Gronenborn, M. Miller, B. W. Tilma, T. Südmeyer, and U. Keller, "Gain characterization and passive modelocking of electrically pumped VECSELs," *Opt. Express*, vol. 20, pp. 24791-24802, 2012.
60. M. Mangold, V. J. Wittwer, O. D. Sieber, M. Hoffmann, I. L. Krestnikov, D. A. Livshits, M. Golling, T. Südmeyer, and U. Keller, "VECSEL gain characterization," *Opt. Express*, vol. 20, pp. 4136-4148, 2012.
61. L. M. Frantz and J. S. Nodvik, "Theory of Pulse Propagation in a Laser Amplifier," *J. Appl. Phys.*, vol. 34, pp. 2346-2349, 1963.

62. R. F. Nabiev and C. J. Chang-Hasnain, "Voltage drop in n- and p-type Bragg reflectors for vertical-cavity surface-emitting lasers," *IEEE Photonics Technology Letters*, vol. 7, pp. 733-735, 07 1995.
63. E. F. Schubert, L. W. Tu, G. J. Zyzdik, R. F. Kopf, A. Benvenuti, and M. R. Pinto, "Elimination of heterojunction band discontinuities by modulation doping," *Applied Physics Letters*, vol. 60, pp. 466-468, 1992.
64. A. D. Katnani and G. Margaritondo, "Empirical rule to predict heterojunction band discontinuities," *Journal of Applied Physics*, vol. 54, pp. 2522-2525, 1983.
65. S. Massidda, B. I. Min, and A. J. Freeman, "Interface phenomena at semiconductor heterojunctions: Local-density valence-band offset in GaAs/AlAs," *Physical Review B*, vol. 35, pp. 9871-9874, 1987.
66. W. S. Capinski and H. J. Maris, "Thermal conductivity of GaAs/AlAs superlattices," *Physica B: Condensed Matter*, vol. 219, pp. 699-701, 1996.
67. J. Piprek, T. Troger, B. Schroter, J. Kolodzey, and C. S. Ih, "Thermal conductivity reduction in GaAs-AlAs distributed Bragg reflectors," *Photonics Technology Letters, IEEE*, vol. 10, pp. 81-83, 1998.
68. P. Zhou, J. Cheng, C. F. Schaus, S. Z. Sun, D. Kopchik, C. Hains, W. Hsin, C. Chen, D. R. Myers, G. A. Vawter, G. R. Olbright, and R. P. Bryan, "Low series resistance continuously graded mirror multiple quantum-well vertical-cavity surface-emitting lasers grown by MOCVD," *Electron Devices, IEEE Transactions on*, vol. 38, pp. 2697-2698, 1991.
69. S. A. Chalmers, K. L. Lear, and K. P. Killeen, "Low resistance wavelength-reproducible p-type (Al,Ga)As distributed Bragg reflectors grown by molecular beam epitaxy," *Applied Physics Letters*, vol. 62, pp. 1585-1587, 1993.
70. K. Kurihara, T. Numai, I. Ogura, A. Yasuda, M. Sugimoto, and K. Kasahara, "Reduction in the series resistance of the distributed Bragg reflector in vertical cavities by using quasi-graded superlattices at the heterointerfaces," *Journal of Applied Physics*, vol. 73, pp. 21-27, 1993.
71. P. G. Newman, J. Pamulapati, H. Shen, M. Taysing-Lara, J. Liu, W. Chang, G. Simonis, B. Koley, M. Dagenais, S. Feld, and J. Loehr, "Molecular beam epitaxial growth of vertical cavity surface emitting lasers with digital alloys and digital gradings," *Journal of Vacuum Science & Technology B: Microelectronics and Nanometer Structures*, vol. 18, pp. 1619-1622, 2000.
72. M. G. Peters, B. J. Thibeault, D. B. Young, J. W. Scott, F. H. Peter, A. C. Gossard, and L. A. Coldren, "Band - gap engineered digital alloy interfaces for lower resistance vertical - cavity surface - emitting lasers," *Appl. Phys. Lett.*, vol. 63, pp. 3411-3413, 1993.
73. D. W. Winston and R. E. Hayes, "Optoelectronic device simulation of Bragg reflectors and their influence on surface-emitting laser characteristics," *Quantum Electronics, IEEE Journal of*, vol. 34, pp. 707-715, 1998.
74. P. Kreuter, "Modeling of Electrically Pumped Vertical-External-Cavity Surface-Emitting Lasers," ETH Zürich, PhD thesis, 2010.
75. D. B. Young, "Molecular beam epitaxy and fabrication techniques for advanced vertical cavity lasers," University of California, PhD thesis, Dec. 1996.
76. Y.-C. Chang, "Engineering vertical-cavity surface-emitting lasers for high-speed operation," University of California, PhD dissertation, 2008.

77. W. P. Pallmann, C. A. Zaugg, M. Mangold, I. Dahhan, M. Golling, B. W. Tilma, B. Witzigmann, and U. Keller, "Ultrafast Electrically Pumped VECSELs," *Photonics Journal, IEEE*, vol. 5, pp. 1501207-1501207, 2013.
78. Y. H. Wang, K. Tai, J. D. Wynn, M. Hong, R. J. Fischer, J. P. Mannaerts, and A. Y. Cho, "GaAs/AlGaAs multiple quantum well GRIN-SCH vertical cavity surface emitting laser diodes," *Photonics Technology Letters, IEEE*, vol. 2, pp. 456-458, 1990.
79. I. Dahhan, Y. Barbarin, M. Hoffmann, W. P. Pallmann, C. A. Zaugg, M. Golling, T. Südmeyer, U. Keller, and B. Witzigmann, "Current confinement in EP-VECSELs for high power single-mode operation suitable for passive mode-locking," in *SPIE Photonics Europe*, Brussels, Belgium, 2012, p. 84330C.
80. K. D. Choquette, A. J. Fischer, K. M. Geib, G. R. Hadley, A. A. Allerman, and J. J. Hindi, "High single mode operation from hybrid ion implanted/selectively oxidized VCSELs," in *International Semiconductor Laser Conference*, Monterey, CA, USA, 2000, pp. 59-60.